

Institut für Kern- und Teilchenphysik
TU Dresden

**$Z \rightarrow \tau\tau$ Cross Section Measurement and
Liquid-Argon Calorimeter Performance
at High Rates at the ATLAS Experiment**

von

Frank Seifert

2012

Institut für Kern- und Teilchenphysik
Fakultät Mathematik und Naturwissenschaften
Technische Universität Dresden

$Z \rightarrow \tau\tau$ Cross Section Measurement and Liquid-Argon Calorimeter Performance at High Rates at the ATLAS Experiment

Dissertation

zur Erlangung des akademischen Grades

Doctor rerum naturalium

(Dr. rer. nat.)

vorgelegt von

Diplom-Physiker Frank Seifert

geboren am 08.02.1984 in Dresden

Dresden 2012

Eingereicht am 12.11.2012

1. Gutachter: Jun.-Prof. Dr. A. Straessner
2. Gutachter: Prof. Dr. A. Quadt

Verteidigt am 10.01.2013

Abstract

In this study, a measurement of the production cross section of Standard Model Z bosons in proton-proton collisions in the decay channel $Z \rightarrow \tau\tau$ is performed with data of $1.34\text{fb}^{-1} - 1.55\text{fb}^{-1}$ recorded by the ATLAS experiment at the LHC at a center-of-mass energy of $\sqrt{s} = 7\text{TeV}$. An event selection of the data is applied in order to obtain a sample enriched with $Z \rightarrow \tau\tau$ events. After background estimations using data and Monte Carlo (MC) simulations, the fiducial cross sections in the sub-channels $Z \rightarrow \tau\tau \rightarrow e\tau_h + 3\nu$ and $Z \rightarrow \tau\tau \rightarrow \mu\tau_h + 3\nu$ are measured. Together with the geometrical and kinematical acceptance, A_Z , and the well known tau lepton branching fractions, these results are combined to a total inclusive $Z \rightarrow \tau\tau$ cross section. A_Z is obtained from MC studies only, and the combination of the channels is done including statistical and systematical uncertainties using the BLUE method. The result is a measured total inclusive cross section of $\sigma_{tot}^{inc}(Z \rightarrow \tau\tau) = 914.4 \pm 14.6(\text{stat}) \pm 95.1(\text{syst}) \pm 33.8(\text{lumi})\text{ pb}$. This is in agreement with theoretical predictions from NNLO calculations of $\sigma^{theory}(Z \rightarrow \tau\tau) = 964 \pm 48\text{ pb}$ and also with measurements previously performed by the ATLAS and CMS experiments. With the increased amount of data, the statistical uncertainty could be reduced significantly compared to previous measurements.

Furthermore, a testbeam analysis is performed to study the operation of the electromagnetic and hadronic endcap calorimeters, EMEC and HEC, and of the forward calorimeter, FCal, in the high particle fluxes expected for the upgraded LHC. The high voltage return currents of the EMEC module are analysed in dependence of the beam intensity. The results are compared to model predictions and simulations to extract the point of critical operation. Overall, the results for the critical beam intensities and the critical high voltage currents are in agreement with the predictions, but the assigned uncertainties are rather large. The general behaviour of the high voltage current in dependence of the beam intensity above the critical intensity could be confirmed very well. The testbeam data show that the EMEC can be operated up to highest LHC luminosities, and that ATLAS conserves its excellent calorimeter performance in this detector area.

Kurzfassung

In dieser Studie wird eine Wirkungsquerschnittsmessung des Standardmodell- Z -Bosons im Zerfallskanal $Z \rightarrow \tau\tau$ mit Kollisionsereignissen entsprechend 1.34 fb^{-1} bis 1.55 fb^{-1} aufgezeichneter Daten des ATLAS-Experiments am LHC bei einer Schwerpunktsenergie von $\sqrt{s} = 7 \text{ TeV}$ durchgeführt. Hierbei kommt eine spezielle Ereignisselektion der Daten zum Einsatz, die zum Ziel hat, einen mit $Z \rightarrow \tau\tau$ Ereignissen angereicherten Datensatz zu erhalten. Nach einer Untergrundabschätzung mit Hilfe von experimentellen Daten und Monte-Carlo(MC)-Simulationen wird eine spezifische Wirkungsquerschnittsmessung in den Unterkanälen $Z \rightarrow \tau\tau \rightarrow e\tau_h + 3\nu$ und $Z \rightarrow \tau\tau \rightarrow \mu\tau_h + 3\nu$ erreicht, welche zunächst nur Ereignisse in der geometrischen und kinematischen Akzeptanzregion umfasst. Zusammen mit der Selektionseffizienz dieser Akzeptanzregion, A_Z , und den bekannten Tau-Lepton-Verzweigungsverhältnissen können diese Ergebnisse zu einem totalen, inklusiven $Z \rightarrow \tau\tau$ Wirkungsquerschnitt kombiniert werden. Hierbei wird A_Z ausschließlich aus MC-Studien bestimmt und die Kombination unter Berücksichtigung der statistischen und systematischen Fehler der Einzelkanäle mit der BLUE-Methode durchgeführt. Das Ergebnis ist ein totaler, inklusiver Wirkungsquerschnitt von $\sigma_{tot}^{inc}(Z \rightarrow \tau\tau) = 914.4 \pm 14.6(\text{stat}) \pm 95.1(\text{syst}) \pm 33.8(\text{lumi}) \text{ pb}$. Dies stimmt innerhalb der Messunsicherheiten sowohl mit theoretischen Vorhersagen aus NNLO Rechnungen von: $\sigma^{theory}(Z \rightarrow \tau\tau) = 964 \pm 48 \text{ pb}$ als auch mit Messungen, die zuvor im Zuge der ATLAS- und CMS-Experimente durchgeführt wurden, überein. Im Vergleich zu den bisherigen Messungen können die statistischen Fehler mit dem größeren Datensatz deutlich reduziert werden.

Weiterhin wird eine Teststrahlstudie zur Prüfung der Funktionalität der elektromagnetischen und hadronischen Endkappenkalorimeter, EMEC und HEC, und des Vorwärtskalorimeters FCal in den zukünftigen, hohen Teilchenflussdichten des verbesserten LHC präsentiert. Die Hochspannungsströme des EMEC-Moduls werden in Abhängigkeit von der Strahlintensität analysiert. Weiterhin werden die Ergebnisse mit Modellvorhersagen und Simulationen verglichen, um die Punkte nichtlinearen (kritischen) Betriebes zu extrahieren. Die Ergebnisse für die kritische Strahlintensität und die kritischen Ströme stimmen mit Modellrechnungen und Simulationen überein, die jedoch mit großen Unsicherheiten behaftet sind. Das vorhergesagte Verhalten der Hochspannungsströme in Abhängigkeit von der Strahlintensität oberhalb der kritischen Intensität konnte sehr genau bestätigt werden. Die Teststrahl Daten zeigen, dass das EMEC bis zu den höchsten LHC-Luminositäten arbeiten kann und ATLAS in dieser Detektorregion seine exzellenten Kalorimeteigenschaften beibehält.

Contents

List of Figures	11
List of Tables	14
1 Introduction	17
2 Theoretical Foundation	19
2.1 The Standard Model of Particle Physics	19
2.1.1 Phenomenological Overview	19
2.1.2 Quantum Electrodynamics	21
2.1.3 Electroweak Interaction	23
2.1.4 Particle Masses and the Higgs Mechanism	24
2.1.5 Quantum Chromo Dynamics	27
2.2 Z Boson Production and Decay at the LHC	29
2.3 Event Generation and Simulation	31
2.3.1 The Partonic Process	31
2.3.2 Hadronization	33
2.3.3 The Underlying Event	33
2.3.4 Detector Simulation	33
2.4 Cross Section Predictions for Z Boson Production at the LHC	34
3 The LHC and the ATLAS Experiment	37
3.1 The Large Hadron Collider	37
3.2 The ATLAS Experiment	39
3.2.1 The Inner Detector	41
3.2.2 The Electromagnetic Calorimeter	42
3.2.3 The Hadronic Calorimeter	47
3.2.4 The Muon Spectrometer	48
3.2.5 Luminosity Measurement	49
3.2.6 The Trigger System	51
3.2.7 Data Taking	52
4 Testbeam Study of Liquid-Argon Calorimeter Performance at High Rates	55
4.1 Upgrade Plans of the LHC and the ATLAS Calorimeters	55
4.2 Testbeam Parameters and Setup	56
4.3 The Calorimeter Test Modules	58
4.4 Test Module Readout and Signal Degradation	58
4.5 Measurement and Analysis of the HV Currents	61

4.5.1	Device for Precision HV Current Measurement	62
4.5.2	Testbeam Data Taking	62
4.5.3	Analysis of the EMEC Currents	63
4.5.4	Beam Intensity Measurement	65
4.5.5	Comparison of EMEC Currents to Beam Intensity	67
4.5.6	Discussion Considering the Predictions	72
4.6	Summary of Results	74
5	$Z \rightarrow \tau\tau$ Cross Section Measurement with 1.34-1.55 fb⁻¹	75
5.1	Introduction	75
5.2	Data and Monte Carlo Samples	75
5.2.1	Trigger Requirements	76
5.2.2	Monte Carlo Simulations	76
5.2.3	Pile-up Simulation	77
5.2.4	Tau Trigger Weighting	78
5.3	Event Preselection	78
5.3.1	Good Run List	78
5.3.2	Vertex Requirement	79
5.3.3	Calorimeter Jet Cleaning	80
5.3.4	Liquid-Argon Calorimeter Hole Cleaning	80
5.4	Reconstructed Physics Objects	81
5.4.1	Muons	82
5.4.2	Electrons	82
5.4.3	Jets	84
5.4.4	Taus	84
5.4.5	Missing Transverse Energy	86
5.4.6	Overlap Removal	87
5.5	Event Selection	88
5.5.1	Dilepton Veto	88
5.5.2	Opposite Charge Between the Lepton and the Hadronic Tau Candidate	89
5.5.3	Reduction of W +jets Background	89
5.5.4	Final Requirements on the Tau Candidate	90
5.5.5	Visible Mass Window	91
5.5.6	Summary of the Event Selection	92
5.6	Tau Identification Variables	96
5.7	Background Estimation	99
5.7.1	W +jets	99
5.7.2	Z +jets	100
5.7.3	QCD Multijet Events	102
5.8	Cross Section Measurement	103
5.9	Systematic Uncertainties	106
5.9.1	Trigger Efficiencies and Scale Factors	106
5.9.2	Reconstruction, Identification and Isolation Efficiencies of the Muons and Electrons	107
5.9.3	Identification Efficiency of the Hadronically Decaying Tau	108
5.9.4	Background Estimation	109
5.9.5	Geometrical and Kinematical Acceptance A_Z	110

5.9.6	Energy Scale Uncertainty	111
5.9.7	Further Systematic Uncertainties	112
5.9.8	Summary of Systematic Uncertainties	112
5.10	Combination of the Channels and Results	112
5.11	The $Z \rightarrow \tau\tau$ Cross Section Measurement in the LHC Physics Context	115
6	Summary and Outlook	121
A	Gauge Invariance in Quantum Electrodynamics	123
A.1	Local gauge invariance	123
A.2	Gauge invariance of the Maxwell-Equations	123
B	Testbeam Results	125
C	Tau Trigger Weighting	131
C.1	Event Selection	131
C.2	Tau Trigger Efficiency Measurement	132
C.3	Systematic Uncertainties	133
	Bibliography	135

List of Figures

2.1	Left: three gluon interaction in QCD with the coupling order g_s and right: four gluon interaction in QCD with the coupling order g_s^2	28
2.2	Diagram of p-p interaction with the production of a Z boson at the LHC. . .	30
2.3	PDF distribution parametrisations evolved to different Q^2 values using the CTEQ66 PDF set.	30
2.4	Feynman diagrams of Z boson production and decay at the LHC.	32
2.5	Standard Model production cross sections at the LHC and the Tevatron. . .	35
3.1	The LHC magnetic dipole field configuration.	38
3.2	Scheme of the accelerator system at CERN.	39
3.3	The ATLAS detector with labels for the most important elements.	40
3.4	The inner detector of the ATLAS experiment.	41
3.5	The electromagnetic (EM) calorimeter of the ATLAS experiment.	42
3.6	Schematic view of the accordion shape structure of the LAr barrel calorimeter.	43
3.7	Photograph of one side of the EMEC module and scheme of the FCal1 absorber matrix.	44
3.8	Scheme of the overall LAr detector readout electronics.	46
3.9	Cut-away view of the hadronic calorimeter of the ATLAS experiment. . . .	47
3.10	The ATLAS muon spectrometer system.	49
3.11	Scheme of the magnet system of the muon spectrometer.	50
3.12	Photographs of the LUCID (left) and the BCM (right) before installation. .	51
3.13	Scheme of the L1 trigger.	52
4.1	Working scheme of the U-70 proton accelerator for the Hilum testbeam project.	57
4.2	Layout of the experimental setup in beamline 23 of the U-70 accelerator. . .	58
4.3	Left: layout of the FCal test module with the two parts visible the approximate beam size indicated. Right: photograph of the FCal module with some rods taken out.	59
4.4	Shown are layouts of the HEC test module on the left and of the EMEC test module on the right.	60
4.5	Left figure: theoretical prediction of the triangular and the shaped signal for a 2 mm LAr gap of the EMEC. Right figure: response of one channel of the HEC test module to a calibration pulse, compared to a model function. . . .	60
4.6	Normalized signal amplitude in dependence of the relative ionization rate. . .	61
4.7	HV current measurement device used for precision measurements of the HV return currents of the LAr calorimeter test modules during the HiLum testbeams in Protvino, Russia.	62

4.8	Left: Measured beam intensity of the Cherenkov monitor in dependence of the ionization chamber measurements up to 7×10^{10} p/s. Right: Cherenkov counter measurements against the intensity as measured by the secondary emission chamber in the range up to 2.5×10^{11} p/s.	66
4.9	Left: Absolute calibration of the Cherenkov monitor with activated aluminium foils. Right: Cherenkov counter measurements for two different time scales.	66
4.10	HV current in dependence of beam intensity for run period 712-715.	68
4.11	HV current in dependence of beam intensity for run period 718-727.	69
4.12	HV current in dependence of beam intensity for run period 737-747.	69
4.13	HV current in dependence of beam intensity for run period 745-763.	70
4.14	HV current in dependence of beam intensity for run period 797-827.	70
4.15	Distributions of the integrated HV current over the spill divided by a single measurement within this spill for all signal measurements in the five analysed run periods together.	72
5.1	The average number of pile-up interactions in data (red) and γ^*/Z Monte Carlo (blue) before applying event weights to the MC sample.	77
5.2	Illustration of the definitions of d_0 in the R- ϕ plane (left) and z_0 in the R- z plane (right).	79
5.3	The distributions of the isolation variables $\sum p_T^{track}(\Delta R < 0.4)/p_T^\mu$ (a) and $\sum E_T^{cell}(\Delta R < 0.3)/p_T^\mu$ (b).	83
5.4	The distributions of the isolation variables $\sum p_T^{track}(\Delta R < 0.4)/p_T^{el}$ (a) and $\sum E_T^{cell}(\Delta R < 0.4)/p_T^{el}$ (b).	83
5.5	The distributions of the number of reconstructed leptons are shown for the (a) $\mu\tau_h$ and (b) $e\tau_h$ final states.	88
5.6	Diagrams of Z and W boson decays in the plane fixed by their decay products.	89
5.7	The distributions of $\sum \cos \Delta\phi$ are shown for the (a) $\mu\tau_h$ and (b) $e\tau_h$ final states.	90
5.8	The distributions of m_T are shown for the (a) $\mu\tau_h$ and (b) $e\tau_h$ final states.	91
5.9	The distributions of the number of tracks of the hadronic tau candidate are shown for the (a) $\mu\tau_h$ and (b) $e\tau_h$ final states.	92
5.10	The distributions of the m_{vis} are shown for the (a) $\tau_\mu\tau_h$ and (b) $\tau_e\tau_h$ final states.	92
5.11	The distributions of muon p_T (a) and electron E_T (b) as well as eta distributions of the leptons (c) and (d) in the $\tau_\mu\tau_h$ (left) and $\tau_e\tau_h$ (right) final states.	94
5.12	The distributions of tau p_T (a) and (b) as well as eta distributions of the tau candidates (c) and (d) in the $\tau_\mu\tau_h$ (left) and $\tau_e\tau_h$ (right) final states.	95
5.13	The distributions of the E_T^{miss} are shown for the (a) $\tau_\mu\tau_h$ and (b) $\tau_e\tau_h$ final states.	95
5.14	Event display of an ATLAS collision data event candidate of a produced Z boson and its decay in the channel $Z \rightarrow \tau\tau \rightarrow \mu\tau_h$	96
5.15	The final tau BDT score is shown before applying the tau identification BDT medium (and the cuts on the number of tracks and unit charge of the tau candidate) on the top left and after applying it on the top right plot.	97

5.16	The distributions of the following variables relevant for tau identification are shown for events passing the full event selection of the $\tau_\mu\tau_h$ channel: The invariant mass of the topological clusters, the impact parameter significance of the leading track, the core energy fraction, the invariant mass of the track system, the average distance of the tracks and the transverse flight path significance.	98
5.17	The distributions of the E_T of the tau candidate in the W enriched control region are shown for the (a) $\mu\tau_h$ and (b) $e\tau_h$ final states before applying the correction factors.	100
5.18	The distributions of E_T of the electron (a) and the tau candidate (b) in the Z -enriched control region, where an electron is faking the hadronic tau candidate.	100
5.19	The distributions of the E_T of the tau candidate in the Z enriched control region, where an extra jet is faking the hadronic tau candidate, are shown for the (a) $\tau_\mu\tau_h$ and (b) $\tau_e\tau_h$ final states before applying the correction factors.	101
5.20	Scheme of sideband control regions for multijet estimation.	102
5.21	Muon trigger efficiencies for the isolated muon triggers in dependence of p_T of the muon for data compared to MC.	107
5.22	Electron trigger and isolation scale factors.	107
5.23	Muon isolation efficiency and scale factors in dependence of p_T (a) and η (b) of the muon.	108
5.24	The ratio of events with oppositely charged lepton and tau candidate and similarly charged ones, $R_{OS/SS}$, as a function of the cutflow steps.	109
5.25	The cross sections as measured in the individual channels and the combined value.	114
5.26	Z production cross section in dependence of the center of mass energy.	115
B.1	Simulation of electron and ion density on the left and electric field on the right over the 2 mm LAr gap for different beam intensities.	126
B.2	Induced current on the left and pulse shape shaper on the right over time for different beam intensities as obtained from simulations.	126
B.3	Pulse shapes of the EMEC test module normalized to the beam intensity and averaged over many bunches for four different beam intensities.	127
B.4	Response of the calorimeter signal amplitude (ADC counts per proton) in dependence of the beam intensity.	128
C.1	The distributions of the visible mass (a) and E_T of the tau candidate (b) for the selection applied for the tau trigger efficiency measurement.	132
C.2	The distributions of the tau trigger efficiency in dependence of E_T of the tau candidate and for MC and data with different background correction methods.	133

List of Tables

2.1	Particles and quantum numbers of the Standard Model of particles physics.	20
2.2	Summary of particle masses.	27
2.3	Summary of most important Z decay modes and branching fractions.	29
3.1	Properties and operating parameters of the ATLAS LAr calorimeters.	45
3.2	Summary of data taking periods for the ATLAS 7 TeV LHC run.	53
4.1	Summary of testbeam runs used for analysis of the EMEC HV currents.	63
4.2	Thresholds to separate signal measurements from background only ones in nA.	64
4.3	Summary of the fit parameters obtained by applying the fit equation 4.10 to the five analysed run periods.	71
4.4	Summary of the fit parameters for the summed channels with I_c and i_c divided by the spill length.	73
4.5	Comparison of obtained parameters averaged over the corresponding run periods with the model predictions.	73
5.1	Cut values for jet cleaning cuts used in the analysis.	81
5.2	The η and ϕ coordinates for the Liquid-Argon hole cleaning.	81
5.3	Inner detector quality requirements for muons.	82
5.4	Identification variables for the BDT algorithm to identify hadronically decaying tau leptons.	85
5.5	Preselection criteria for electrons, muons, hadronic taus and jets used for the overlap removal and dilepton veto.	87
5.6	Cutflow table for the $\mu\tau_h$ channel starting after the full object selection.	93
5.7	Cutflow table for the $e\tau_h$ channel starting after the full object selection.	93
5.8	Correction factors k_W for the W +jets Monte Carlo samples as measured with regard to data.	99
5.9	Correction factors k_Z for the Z +jets Monte Carlo samples as measured with regard to data.	101
5.10	Number of events in the ABCD control regions used for the multijet background estimation. Signal and other background processes are estimated from Monte Carlo, while the number of Multijet events is estimated from data after subtracting the EW processes.	103
5.11	Summary of the factors A_Z , C_Z and the luminosity for the $\mu\tau_h$ and the $e\tau_h$ channel.	105
5.12	The production cross section times branching ratio for the $Z \rightarrow \tau\tau$ process as measured in both channels.	105

5.13	Relative systematic uncertainties of the different contributions to A_Z and total ones for the $e\tau_h$ channel and the $\mu\tau_h$ channel.	110
5.14	Tau energy scale uncertainties in dependence of E_T and η of the tau candidate.	111
5.15	Statistical and systematic uncertainties in % relative to the total cross section measurement.	113
5.16	List of Monte Carlo samples for Z +jets production. The generated mass of the Z boson is $M_Z > 40$ GeV.	117
5.17	List of Monte Carlo samples for W +jets production. The samples are generated with ALPGEN and split per number of initial extra partons (NpX, X=0, ..., 5).	118
5.18	List of Monte Carlo samples for Z +jets production. The generated mass of the Z boson is $10 \text{ GeV} < M_Z < 40 \text{ GeV}$	119
5.19	List of Monte Carlo samples for the $t\bar{t}$ production, generated with MC@NLO 3, and for the diboson production, generated with HERWIG 6.5.	119

1 Introduction

In the last decades, nuclear and particle physics has made enormous steps toward an overall understanding of the fundamental constituents and of the forces of nature. This includes the electromagnetic force explaining the majority of phenomena of the macroscopic world, the discovery of the heavy W and Z bosons as force carriers of the weak interaction up to the quarks and gluons as fundamental components of nuclei and of matter. All known particles and the forces connecting them (except gravitation) are unified in the so-called "Standard Model" of particle physics. It can explain a wide range of observations, from the generation of the relatively high proton and neutron masses by the strong interaction between the quarks up to radioactive decays or the generation and propagation of electromagnetic waves. A lot of these findings have been gained at particle accelerator experiments. Also the Higgs mechanism of generating fundamental particle masses is likely to be confirmed at the LHC.

Nevertheless, many questions still remain unanswered, like the large matter-to-antimatter asymmetry in the early universe, the origin of dark matter or the fine tuning of physical constants. To explore these research fields and get hints on possible new physics, the LHC will continue data taking over the next decade, also with increased energy and luminosity. Large amounts of data have to be analysed by the LHC experiments to be sensitive to new physics signatures with small cross sections. In addition, the production rates of Standard Model particles and their properties have to be known very well.

In this work, a study of the cross section measurement of the Z boson in the decay channel into two tau leptons with the ATLAS experiment at the LHC is presented. Z boson production is an important background in searches for Higgs bosons and possible new physics signals. The new resonance discovered [1, 2] by the LHC experiments, ATLAS [3] and CMS [4], is likely to be a Higgs boson, but more of its properties have to be measured. For example, its decay into two tau leptons has not yet been observed, but must be measured to confirm its nature. This $H \rightarrow \tau\tau$ decay is rare and the main background of $Z \rightarrow \tau\tau$ events has to be understood as precisely as possible. The study presented here uses the semileptonic decay channels $Z \rightarrow \tau\tau \rightarrow e\tau_h + 3\nu$ and $Z \rightarrow \tau\tau \rightarrow \mu\tau_h + 3\nu$ which are also the most sensitive final states for the search of Higgs boson decays into two tau leptons.

Furthermore, with the LHC center-of-mass energies of 7 TeV are reached for the first time by a particle collider. Therefore, production rates and properties of known particles have to be tested at these energies. This includes the production cross section of the Z boson as well as its decay properties. These results are also relevant to confirm theoretical models and predictions about physics at these energies.

Previous studies of the Z cross section have already been made by the ATLAS [5] and CMS [6] experiments with the 2010 dataset of 36 pb^{-1} in the $Z \rightarrow \tau\tau$ decay channel. The study presented here complements these measurements with increased statistics of the 2011 dataset using integrated luminosities of 1.34 fb^{-1} ($e\tau_h + 3\nu$ decay channel) and 1.55 fb^{-1} ($\mu\tau_h + 3\nu$ decay channel). The obtained result is compared to theoretical calculations including second order loop corrections [7] as well as to $Z \rightarrow ee$ and $Z \rightarrow \mu\mu$ cross sections measured by ATLAS on the basis of lepton universality.

To further increase the discovery potential for new physics phenomena, the LHC is planned to be upgraded in several steps. The center-of-mass energy is planned to reach 13-14 TeV in 2015. In the long term, the instantaneous luminosity is intended to be increased to 5-7 times the original design value of $10^{34} \text{ cm}^{-2}\text{s}^{-1}$. Especially the upgrade in instantaneous luminosity is very challenging for many detector components of the experiments. This work also presents a testbeam study to investigate the performance of the ATLAS calorimeters in the endcap and forward regions in the environment of the high luminosity LHC. These calorimeters are based on liquid-argon (LAr) technology, and the charge density produced within the LAr gaps is one limiting factor of the performance. The results obtained are discussed with regard to those charge build-up effects and are compared to model predictions and simulations.

This thesis is structured as follows:

Chapter 2 describes the theoretical foundation of this work. It introduces the Standard Model of particle physics up to the Higgs mechanism and explains the steps of Monte Carlo generation procedure to simulate proton-proton collision events. Monte Carlo simulations are also used to calculate predictions of production cross sections, as for the Z boson production.

Chapter 3 introduces the LHC and the ATLAS experiment. Parameters of the collider are described as well as the various components of the ATLAS detector. The sub-detectors most relevant for the testbeam study and the $Z \rightarrow \tau\tau$ cross section analysis are explained in special detail.

Chapter 4 is presenting the testbeam study of ATLAS LAr calorimeter performance at high particle rates in the high-luminosity environment of the planned LHC upgrade. This chapter focuses on the testbeam setup at the U-70 proton synchrotron in Protvino, Russia, the data taking and the testbeam results. They are relevant for both high luminosity operation and online determination of the relative luminosity of ATLAS.

Chapter 5 describes the $Z \rightarrow \tau\tau$ cross section analysis in detail. It starts with the description of the data and Monte Carlo samples used and the event preselection cuts. The selection criteria for the physical objects like electrons, muons and tau leptons are explained as well as the final event selection of $Z \rightarrow \tau\tau$ events. The extraction of the fiducial and the $Z \rightarrow \tau\tau$ inclusive cross section is described and the results of the sub-channels are combined to one final result which is compared to theoretical predictions.

Chapter 6 gives a summary and outlook.

2 Theoretical Foundation

2.1 The Standard Model of Particle Physics

2.1.1 Phenomenological Overview

The Standard Model (SM) of particle physics [8–12] is a quantum gauge theory describing all presently known particles and their interactions via the electromagnetic, weak and strong force with high precision. The particles forming all usual matter are the up-quark (u), the down-quark (d) which compose the protons and neutrons of all nuclei, and the electron (e) responsible for the atomic shells. However, more fundamental particles are known which can be ordered in three families. The particles mentioned above belong to the first family and have relatively small masses, while the charged particles of the other two families are heavier and unstable. Finally, they decay into particles of the first family within fractions of a second, except neutrinos. The fundamental particles are categorized into quarks (d, u, s, c, b and t) and leptons ($e, \nu_e, \mu, \nu_\mu, \tau$ and ν_τ). They are of half-integer spin and thus fermions following the Fermi-Dirac statistics. For each lepton and quark there is also a corresponding anti-particle with opposite charge.

The forces responsible for the interactions of the particles are mediated via gauge bosons, which are of integer spin (categorized as bosons). The most widely known gauge boson is the one mediating the electromagnetic interaction, the photon (γ). It is massless and therefore traveling at the speed of light, couples to the electric charge, Q , and carries no electric charge itself. Photons are also the components of all kinds of electromagnetic radiation. The electromagnetic force is responsible for many macroscopic phenomena like the optical visibility, electricity or chemical reactions.

The weak interaction describes nuclear reactions like radioactive decays and the decay of the heavier quarks and leptons of the second or third family into the lighter ones. The gauge bosons of the weak interaction are the electrically charged W^+ and W^- bosons and the neutral Z boson. In contrast to the photon, they are very massive leading to a short range ($\approx 10^{-18}$ m) and weak effective coupling of that force. The W^\pm bosons couple to the third component of the weak isospin (I_3^W) which is only non-zero for left-handed particles. Therefore, right-handed particles do not participate in the weak interaction. The electromagnetic and weak interaction are unified to the electroweak interaction, and the weak isospin (\mathbf{I}^W) and the electric charge (Q) are connected by the Gell-Mann-Nishijima relation

$$I_3^W = Q - \frac{Y}{2} \tag{2.1}$$

with Y being the weak hypercharge.

The protons, neutrons and other baryons are not fundamental but composed of quarks. Quarks are bound via the strong interaction, which is also responsible for the adhesiveness of protons and neutrons within nuclei. The strong force is mediated by the gluon. It is massless and couples to the strong colour charge, which exists in three types named red (r), green (g) and blue (b) and the corresponding anti-charges. They add up to zero not only with one colour charge and its anti-charge but also with having one of each of the three charges. Only the quarks (and the gluon itself) carry a strong colour charge and three quarks or one quark and one antiquark are needed to create a colour-neutral object. As the gluons themselves carry strong charge (one of eight mixed states between r, g and b), they interact with each other leading to non-perturbative behaviour (at low momentum transfer). At low energies, the strong force is characterized by confinement and a range of the order of the size of a proton ($\approx 10^{-15}$ m). Confinement means that a colour charged particle does not exist freely but is always bound with other colour charged particles forming a colour-neutral object.

An overview of the described particles, gauge bosons and some of their quantum numbers is given in Table 2.1. The Standard Model, as a gauge theory, is based on the symmetry group:

$$SU(3)_C \otimes SU(2)_L \otimes U(1)_Y. \quad (2.2)$$

Table 2.1: Particles and quantum numbers of the Standard Model of particles physics. In addition for each quark and lepton an anti particle with opposite charge exists. The eight different colour charges of the gluon are combinations of the strong colours r, g, b and their anti colours \bar{r} , \bar{g} , \bar{b} .

Particles			Q	$ \mathbf{I}^W $	I_3^W	Y	colour charge	spin
Fermions								
1 st family	2 nd family	3 rd family						
$\begin{pmatrix} u \\ d \end{pmatrix}_L$	$\begin{pmatrix} c \\ s \end{pmatrix}_L$	$\begin{pmatrix} t \\ b \end{pmatrix}_L$	+2/3	1/2	+1/2	+1/3	r,g,b	1/2
$\begin{pmatrix} \nu_e \\ e \end{pmatrix}_L$	$\begin{pmatrix} \nu_\mu \\ \mu \end{pmatrix}_L$	$\begin{pmatrix} \nu_\tau \\ \tau \end{pmatrix}_L$	-1/3	1/2	-1/2	+1/3	r,g,b	1/2
			0	1/2	+1/2	-1	0	1/2
			-1	1/2	-1/2	-1	0	1/2
u_R	c_R	t_R	+2/3	0	0	+4/3	r,g,b	1/2
d_R	s_R	b_R	-1/3	0	0	-2/3	r,g,b	1/2
e_R	μ_R	τ_R	-1	0	0	-2	0	1/2
ν_{eR}	$\nu_{\mu R}$	$\nu_{\tau R}$	0	0	0	0	0	1/2
Bosons								
	γ		0	-	-	-	0	1
	g		0	0	0	0	1 ... 8	1
	W^+		+1	-	-	-	0	1
	W^-		-1	-	-	-	0	1
	Z^0		0	-	-	-	0	1
	H^0		0	1/2	-1/2	1	0	0

$SU(3)_C$ describes the strong force and $SU(2)_L \otimes U(1)_Y$ the unified electroweak interaction. The pure electromagnetic part is described by Quantum Electrodynamics (QED) which is explained in more detail in Section 2.1.2, while the electroweak interaction and the related Higgs mechanism explaining the particle mass generation is described in Sections 2.1.3 and 2.1.4. The Quantum Chromodynamics responsible for the strong interaction is covered in Section 2.1.5.

The gravitational force is not covered by the Standard Model but described by general relativity. A consistent unification of the SM as quantum field theory and general relativity has not been reached at the time of writing. However, gravitation is negligible when describing particle or nuclear reactions at LHC energies.

2.1.2 Quantum Electrodynamics

The aim of Quantum Electrodynamics is the precise description of electromagnetic processes according to physical observations. A fundamental principle of nature is the principle of least action. It leads to the Dirac lagrangian of a relativistic, free, spin 1/2 particle of mass m and electric charge Q like the electron:

$$\mathcal{L}_D = \bar{\psi}(i\gamma_\mu\partial^\mu - m)\psi \quad (2.3)$$

with γ_μ being the Dirac matrices and using Einstein summation convention. $\psi = \psi(\vec{r}, t)$ is the quantum mechanical wave function of the particle in three dimensional space, \vec{r} , and time, t . Hence, the unit system $\hbar = c = 1$ is chosen. From (2.3) the Dirac equation of motion for the free particle can be derived:

$$(i\gamma_\mu\partial^\mu - m)\psi = 0 \quad (2.4)$$

which describes the physical behaviour. ψ itself is not a physical observable but its absolute square $|\psi|^2$. Therefore, the transformed wave function

$$\psi(\vec{r}, t) \xrightarrow{U(1)} \psi'(\vec{r}, t) = e^{iQ\chi}\psi(\vec{r}, t) \quad (2.5)$$

with $\chi = \text{const.}$ and arbitrary, describes the physical system as well. This is a global $U(1)$ gauge transformation under which the Dirac Lagrangian (2.3) is invariant. This is expected because the physical behaviour has to be independent of the arbitrary choice of the global phase χ . This is known as global gauge invariance, and the conservation of the electric charge can be derived from it. It is now required that the phase χ can also be dependent on space and time as $\chi = \chi(\vec{r}, t)$:

$$\psi(\vec{r}, t) \xrightarrow{U(1)} \psi'(\vec{r}, t) = e^{iQ\chi(\vec{r}, t)}\psi(\vec{r}, t), \quad (2.6)$$

and that the physics still has to be independent on the concrete choice of $\chi(\vec{r}, t)$ in order to conserve causality. The lagrangian (2.3) is not invariant under this local gauge transformation:

$$\begin{aligned} \mathcal{L}_D' &= \bar{\psi}'(i\gamma_\mu\partial^\mu - m)\psi' = e^{-iQ\chi(\vec{r}, t)}\bar{\psi}(\vec{r}, t)(i\gamma_\mu\partial^\mu - m)e^{iQ\chi(\vec{r}, t)}\psi(\vec{r}, t) \\ &= e^{-iQ\chi(\vec{r}, t)}\bar{\psi}(\vec{r}, t)(i\gamma_\mu\partial^\mu[e^{iQ\chi(\vec{r}, t)}])\psi(\vec{r}, t) + \bar{\psi}(i\gamma_\mu\partial^\mu - m)\psi \\ &\neq \mathcal{L}_D. \end{aligned} \quad (2.7)$$

The local gauge invariance can be restored by introducing a field, A^μ , with the following transformation behaviour:

$$A^\mu(\vec{r}, t) \rightarrow A^{\mu'}(\vec{r}, t) = A^\mu(\vec{r}, t) - \frac{1}{e} \partial^\mu \chi(\vec{r}, t) \quad (2.8)$$

and by replacing the usual derivative, ∂^μ , by the gauge-covariant derivative:

$$\partial^\mu \rightarrow D^\mu = \partial^\mu + ieQA^\mu(\vec{r}, t). \quad (2.9)$$

The field A^μ also appears in the modified Dirac lagrangian

$$\mathcal{L}_D = \bar{\psi}(i\gamma_\mu D^\mu - m)\psi. \quad (2.10)$$

It is now invariant under local gauge transformation when the local phase transformation (2.6) is applied together with the transformation (2.8) of the field A^μ . This is shown in Appendix A.1. That means the physical system ψ is identical to the locally transformed ψ' , as the local phase transformation (2.6) is compensated by the gauge transformation (2.8) of the field A^μ .

In addition, the physical behaviour of A^μ itself has to be gauge invariant. It is aimed to identify the field A^μ with the photon and thus the Maxwell-equations should hold for A^μ :

$$\partial_\mu F^{\mu\nu} = j^\nu \quad (2.11)$$

with $F^{\mu\nu} = \partial^\mu A^\nu - \partial^\nu A^\mu$ being the electromagnetic field tensor and j^ν being the four-current. With that definition, the Maxwell-equations can be written as:

$$\partial_\mu \partial^\mu A^\nu - \partial_\mu \partial^\nu A^\mu = j^\nu \quad (2.12)$$

or with the definition of the D'Alembert operator, $\square = \partial_\mu \partial^\mu$, as:

$$\square A^\nu - \partial^\nu \partial_\mu A^\mu = j^\nu. \quad (2.13)$$

The Maxwell-equations do not change under the gauge transformation (2.8), as can be seen in Appendix A.2. That means the field A^μ is gauge invariant and can actually be identified with the photon.

The concept of local gauge invariance requires the introduction of a field A^μ which couples to the fermion field ψ with a strength proportional to the electric charge, Q , of the particle. If a local phase transformation of the form (2.6) can be compensated by a gauge transformation of the fields of the form (2.8) leading to local gauge invariance of the Lagrangian (and therefore of the equations of motion) and if the fields are also gauge invariant, then it is a local gauge theory. Therefore, QED is a local gauge theory with the gauge boson identified as the photon.

2.1.3 Electroweak Interaction

In a local gauge theory, the gauge boson has to be massless. With a fixed mass term, M , for the gauge boson the Maxwell equation (2.13) becomes:

$$(\square + M^2)A^\nu - \partial^\nu \partial_\mu A^\mu = j^\nu \quad (2.14)$$

and is not gauge invariant anymore:

$$\square A^{\nu'} - \partial^\nu (\partial_\mu A^{\mu'}) + M^2 A^{\nu'} = \square A^\nu - \partial^\nu (\partial_\mu A^\mu) + M^2 A^\nu - M^2 \partial^\nu \chi = j^\nu - M^2 \partial^\nu \chi \neq j^\nu. \quad (2.15)$$

For QED, a massless gauge boson has been proven experimentally with high precision by determining an upper limit on the photon mass of $M_\gamma < 6 \cdot 10^{-16}$ eV [13]. As QED is a very successful theory, it is aimed to likewise formulate the electroweak interaction as gauge theory. It is experimentally observed that only left handed fermions (and right handed anti-fermions) participate in the weak interaction of charged currents, while neutral currents couple to left handed and also to right handed ones. Therefore, the fermions are arranged in left handed doublets and right handed singlets as in Table 2.1.

The wave function ψ now represents such a 2-dimensional isospin doublet, and U(1) is replaced by the unitary SU(2) operation. It corresponds to a rotation around the direction $\vec{\chi}$ with the angle $|\vec{\chi}|$ in isospin phase space. The local phase transformation in SU(2) can be written as:

$$\psi(\vec{r}, t) \xrightarrow{U(1)} \psi'(\vec{r}, t) = e^{i\vec{\chi}(\vec{r}, t) \cdot \frac{\vec{\sigma}}{2}} \psi(\vec{r}, t) \quad (2.16)$$

with $\vec{I}^W = \vec{\sigma}/2$ and $\vec{\sigma}$ being the Pauli matrices. Compared to QED, the electrical charge Q is replaced by \vec{I}^W and the coupling constant e by the weak coupling constant g . Thus the field A^μ is also replaced by a field of three components, $W_1^\mu, W_2^\mu, W_3^\mu$, shortened with \vec{W}^μ . The covariant derivative is given by:

$$D^\mu = \partial^\mu + ig\vec{I}^W \cdot \vec{W}^\mu(\vec{r}, t) \quad (2.17)$$

and the fields \vec{W}^μ transform as (for simplicity the dependence of \vec{W}^μ, ψ and $\vec{\chi}$ on (\vec{r}, t) is not written explicitly in the following):

$$\vec{W}^\mu \rightarrow \vec{W}^{\mu'} = \vec{W}^\mu - \frac{1}{g} \partial^\mu \vec{\chi} - g[\vec{\chi} \times \vec{W}^\mu]. \quad (2.18)$$

Now it can be shown that the Dirac equation, $(i\gamma_\mu D^\mu - m)\psi = 0$, is invariant under the local transformation (2.16) when applying also the gauge transformation of the fields (2.18) [14, 15]:

$$0 = (i\gamma_\mu D^\mu - m)\psi = (i\gamma_\mu D^{\mu'} - m)\psi' = 0. \quad (2.19)$$

The experimentally observed W^+ and W^- bosons can be written as a linear combination of the W_1 and W_2 fields as:

$$W^{\mu\pm} = \frac{1}{\sqrt{2}}(W_1^\mu \mp iW_2^\mu) \quad (2.20)$$

and are responsible for the observed charged weak currents coupling to left handed fermions. The field W_3^μ would represent the neutral weak currents, but as they couple also to right handed fermions their structure has to be modified compared to the charged currents. This can be done by a mixing of W_3^μ with a neutral $U(1)$ field, B^μ , which has left handed as well as right handed contributions to the coupling. The fields W_3^μ and B^μ mix to the observed γ (field A^μ) and Z^0 (field Z^μ) bosons with the mixing angle θ_w as:

$$\begin{aligned} A^\mu &= \sin \theta_w W_3^\mu + \cos \theta_w B^\mu \\ Z^\mu &= \cos \theta_w W_3^\mu - \sin \theta_w B^\mu. \end{aligned} \quad (2.21)$$

The \vec{W}^μ fields couple with the strength g , while the B^μ field couples with the strength g' . The local phase transformation (2.16) is then extended to:

$$\psi(\vec{r}, t) \xrightarrow{SU(2) \otimes U(1)} \psi' = e^{ig\vec{\alpha}(\vec{r}, t)\vec{I}^W + ig'\frac{Y}{2}\beta(\vec{r}, t)}\psi \quad (2.22)$$

and the covariant Dirac derivative to:

$$D^\mu = \partial^\mu + ig\vec{I}^W \cdot \vec{W}^\mu + ig'\frac{Y}{2}B^\mu. \quad (2.23)$$

This describes the extension of the symmetry to $SU(2)_{IW} \otimes U(1)_Y$ and therefore the electroweak unification [8].

In analogy to (2.13) the gauge invariant Maxwell equations for the three massless fields \vec{W}^μ would be:

$$\square \vec{W}^\mu - \partial^\mu \partial_\nu \vec{W}^\nu = \vec{j}^\mu. \quad (2.24)$$

However, the gauge bosons, W^+ , W^- and Z , are not massless, but are measured to be as heavy as around 80 or 90 proton masses.

2.1.4 Particle Masses and the Higgs Mechanism

As shown in (2.15), the Maxwell equations are not gauge invariant anymore for $M \neq 0$. Therefore, the gauge boson masses have to be generated dynamically. This can be done by introducing a scalar field, φ , that generates gauge currents, $j^\mu(\varphi)$, which then act as effective mass terms. The equations for the four electroweak fields would become:

$$\begin{aligned} \square \vec{W}^\mu - \partial^\mu \partial_\nu \vec{W}^\nu &= \vec{j}^\mu(W) + \vec{j}^\mu(\varphi) \\ \square B^\mu - \partial^\mu \partial_\nu B^\nu &= j_y^\mu(\varphi). \end{aligned} \quad (2.25)$$

This field was suggested in 1964 by Peter Higgs, Francois Englert, Robert Brout, T. W. B. Kibble, Carl R. Hagen and Gerald Guralnik and is commonly called Higgs field [16–19]. It is predicted to have an electrical charge of 0, a weak isospin of $I^W = 1/2$ and as a scalar a spin of 0. Therefore, φ can be written as complex doublet with four components:

$$\varphi(\vec{r}, t) = \begin{pmatrix} \varphi_1(\vec{r}, t) + i\varphi_2(\vec{r}, t) \\ \varphi_3(\vec{r}, t) + i\varphi_4(\vec{r}, t) \end{pmatrix} = e^{i\frac{\vec{g}}{2} \cdot \vec{\delta}(\vec{r}, t)} \begin{pmatrix} 0 \\ \frac{v}{\sqrt{2}} \end{pmatrix}. \quad (2.26)$$

With the continuity equation and the covariant derivative (2.23), the Klein-Gordon currents for a spin 0 Higgs field can be written as:

$$\begin{aligned}\vec{j}^\mu(\varphi) &= ig(\varphi^\dagger \frac{\vec{\sigma}}{2}[D^\mu\varphi] - [D^\mu\varphi]^\dagger \frac{\vec{\sigma}}{2}\varphi) \\ j_y^\mu(\varphi) &= ig' \frac{Y}{2}(\varphi^\dagger [D^\mu\varphi] - [D^\mu\varphi]^\dagger \varphi)\end{aligned}\quad (2.27)$$

which also lead to gauge invariance of the Equations (2.25). By applying the electroweak phase transformation (2.22) to (2.26) with the gauge choice $\vec{\alpha} = -\frac{1}{g}\vec{\theta}$ and $\beta = 0$, the Higgs field simplifies to:

$$\varphi = \begin{pmatrix} 0 \\ \frac{v}{\sqrt{2}} \end{pmatrix}\quad (2.28)$$

which is constant with $|\varphi| = v/\sqrt{2}$ and real with $I_3^W = -1/2$. This is called spontaneous symmetry breaking.

With that result and the covariant derivative (2.23), the four currents (2.27) can be calculated leading to [14]:

$$\begin{aligned}j_1^\mu(\varphi) &= -\frac{g^2 v^2}{4} W_1^\mu \\ j_2^\mu(\varphi) &= -\frac{g^2 v^2}{4} W_2^\mu \\ j_3^\mu(\varphi) &= -\frac{g^2 v^2}{4} W_3^\mu + \frac{gg' v^2}{4} B^\mu \\ j_y^\mu(\varphi) &= +\frac{g^2 v^2}{4} W_3^\mu - \frac{g'^2 v^2}{4} B^\mu.\end{aligned}\quad (2.29)$$

With the definitions

$$M = \frac{vg}{2} \quad \text{and} \quad M' = \frac{vg'}{2},\quad (2.30)$$

these currents correspond to mass terms of the masses M and M' in the gauge invariant field equations (2.25). With the previously introduced definitions (2.21), where θ_w is the Weinberg angle and defined as

$$\tan\theta_w = \frac{g'}{g} = \frac{M'}{M},\quad (2.31)$$

the currents (2.29) inserted into the field equations (2.25) lead to the form:

$$\begin{aligned}[\square + M^2]W_1^\mu - \partial^\mu \partial_\nu W_1^\nu &= j_1^\mu(W) \\ [\square + M^2]W_2^\mu - \partial^\mu \partial_\nu W_2^\nu &= j_2^\mu(W) \\ \square A^\mu - \partial^\mu \partial_\nu A^\nu &= \sin\theta_w \cdot j_3^\mu(W) \\ [\square + (M^2 + M'^2)]Z^\mu - \partial^\mu \partial_\nu Z^\nu &= \cos\theta_w \cdot j_3^\mu(W).\end{aligned}\quad (2.32)$$

The first two equations correspond to massive fields W_1 and W_2 or with (2.20) W^+ and W^- with the masses $M_W = M$. The third equation describes the massless photon field, while the fourth equation corresponds to a massive field Z with the mass

$$M_Z = \sqrt{M^2 + M'^2} \stackrel{(2.31)}{=} \frac{M_W}{\cos\theta_W}. \quad (2.33)$$

The Weinberg angle, $\sin^2\theta_w$, can be measured e.g. in the forward-backward asymmetry in $e^+e^- \rightarrow \mu^+\mu^-$ scattering or from the masses M_W and M_Z . At the time of writing, the most precise values measured for these quantities are: $\sin^2\theta_w = 0.2312(\pm 0.0001)$, $M_W = 80.385(\pm 0.015)$ GeV and $M_Z = 91.188(\pm 0.002)$ GeV [20].

The Higgs field introduced in (2.26) to generate mass terms dynamically can be tested experimentally by producing and measuring a quantum of this field, the Higgs boson. With the potential $V = -\mu^2\varphi^\dagger\varphi + \lambda(\varphi^\dagger\varphi)^2$ the lagrangian of the Higgs field becomes:

$$\mathcal{L}_\varphi = T - V = (\partial_\mu\varphi)^\dagger(\partial^\mu\varphi) + \mu^2(\varphi^\dagger\varphi) - \lambda(\varphi^\dagger\varphi)^2. \quad (2.34)$$

Here, the term $-\mu^2\varphi^\dagger\varphi$ is responsible for the mass generation and $\lambda(\varphi^\dagger\varphi)$ describes the Higgs self coupling. With $\lambda > 0$ and $\mu^2 > 0$ the potential V is symmetric around 0. The minimum is $\neq 0$ but with the choice of (2.26), $\varphi_3 = v/\sqrt{2}$, at:

$$\frac{\partial V}{\partial \varphi} = -\mu^2 + 2\lambda\varphi_3 = 0 \longrightarrow \varphi_3^2 = \frac{\mu^2}{2\lambda} = \frac{v^2}{2}. \quad (2.35)$$

That means the minimum vacuum state is non-zero and realized in nature, and the symmetry is spontaneously broken. The constant v is the vacuum expectation value and connected to the well measured Fermi constant by

$$v^2 = \frac{\sqrt{2}}{2G_F} \quad (2.36)$$

from which it can be calculated to $v \approx 246$ GeV. The mass of the Higgs boson is connected to the free parameter μ via

$$M_H = \sqrt{2\mu^2} \quad (2.37)$$

and has to be measured experimentally.

In 2012 a new resonance has been discovered at the LHC with a mass of around 126 GeV [1, 2] by the ATLAS [3] and CMS [4] experiments. At the time of writing its properties are compatible with the Higgs boson, but more measurements are needed for a confirmation. In this case, the parameter λ would be also known via (2.35) to be $\lambda \approx 0.13$.

While the Higgs mechanism naturally introduces gauge boson masses, the masses of the fermions are not generated directly. Nevertheless, it is possible to generate also the fermion masses with the Higgs mechanism by introducing dimensionless Yukawa couplings between the fermion fields, ψ , and the Higgs field, φ , of the form:

$$-\frac{m_f}{v}\bar{\psi}_{Lf}^d\varphi\psi_{Rf}^d \quad (2.38)$$

for leptons and down type quarks and

$$\frac{m_f}{v} \bar{\psi}_{L_f}^u i\sigma^2 \varphi^* \psi_{R_f}^u \quad (2.39)$$

for up type quarks. Here, m_f are free parameters corresponding to the fermion masses of the left handed and right handed fermions f . These mass terms are generated via spontaneous symmetry breaking when the vacuum expectation value of the Higgs field becomes non-zero, similar to the gauge boson mass terms.

The coupling strength of the fermion f to the Higgs boson is proportional to $\propto \frac{m_f}{v}$. Therefore, heavier fermions have a stronger coupling to the Higgs boson than lighter fermions. A summary of the experimentally measured particle masses is given in Table 2.2.

Table 2.2: A summary of the particle masses as measured experimentally is shown. The values are taken from Reference [20] (except for the Higgs boson) and given without uncertainties.

Category	Particle		Mass
Gauge bosons	Photon	γ	$< 6 \cdot 10^{-16}$ eV
	Z boson	Z^0	91.2 GeV
	W bosons	$W^{+/-}$	80.4 GeV
	Gluon	g	0
Leptons	Electron neutrino	ν_e	$m_{\nu_e}^{eff} = \sqrt{\sum_i U_{ei} ^2 m_{\nu_i}^2} < 2$ eV
	Muon neutrino	ν_μ	$m_{\nu_\mu}^{eff} = \sqrt{\sum_i U_{\mu i} ^2 m_{\nu_i}^2} < 0.19$ MeV
	Tau neutrino	ν_τ	$m_{\nu_\tau}^{eff} = \sqrt{\sum_i U_{\tau i} ^2 m_{\nu_i}^2} < 18.2$ MeV
	Electron	e	0.511 MeV
	Muon	μ	105.7 MeV
	Tau lepton	τ	1777 MeV
Quarks	Down quark	d	4.1 - 5.8 MeV
	Up quark	u	1.7 - 3.3 MeV
	Strange quark	s	101 MeV
	Charm quark	c	1.27 GeV
	Bottom quark	b	4.19 GeV
	Top quark	t	172.0 GeV
Scalar	Higgs boson	H^0	126 GeV (preliminary, at the time of writing)

2.1.5 Quantum Chromo Dynamics

Quantum chromo dynamics (QCD) is the theory of strong interaction [21–24], responsible for the binding of quarks into hadrons and also the formation of nuclei. A wide spectrum of hadrons has been discovered so far. They are categorized into the mesons, which consist of a quark and an antiquark, and the baryons, formed by three quarks or three antiquarks. The simplest and most successful way to describe all observed properties of QCD is by a gauge theory of $SU(3)_C$ in analogy to the electroweak interaction. Only a short theoretical

overview shall be given here.

The lagrangian of QCD can be written as:

$$\mathcal{L}_{QCD} = \bar{\psi}(i\gamma_{\mu}D^{\mu} - m)\psi - \frac{1}{4}F^2 \quad (2.40)$$

with the field tensor of the strong interaction, F , and the gauge-covariant derivative

$$D^{\mu} = \partial^{\mu} + ig_s \frac{1}{2} \lambda^a A_a^{\mu}. \quad (2.41)$$

The gluon field is described by A_a^{μ} , while g_s is the strong coupling constant. The index a indicates the generators of $SU(3)_C$, which ranges from $1 \dots N_C^2 - 1$. N_C is the number of colour charges and in case of $N_C = 3$ eight different generators appear. λ^a are the 8 Gell-Mann matrices. The gauge transformation of the wave function is then given as

$$\psi(\vec{r}, t) \xrightarrow{SU(3)_C} \psi' = e^{ig_s \frac{1}{2} \lambda^a \chi^a} \psi \quad (2.42)$$

with the 8 degrees of freedom in a . The 8 Gell-Mann matrices fulfil the commutation relations:

$$[\lambda^a, \lambda^b] = if^{abc} \lambda^c \quad (2.43)$$

where the f^{abc} are non-zero for some combinations. Furthermore, the strong field tensor, F , in (2.40) can be written as:

$$F_a^{\mu\nu} = \partial^{\mu} A_a^{\nu} - \partial^{\nu} A_a^{\mu} - g_s f^{abc} A^{\mu b} A^{\nu c}. \quad (2.44)$$

The last term means that direct coupling of two gluon fields is possible, which is in contrast to QED. Therefore, the interactions as given in the Feynman-diagrams of Figure 2.1 are also possible in addition to the usual quark-gluon interaction. These gluon-gluon interactions lead to confinement of colour charged partons within colour-neutral hadrons. At small distances the strong coupling constant runs asymptotically to zero leading to asymptotic freedom of the partons within the colour-neutral objects. No free quarks have been found until the time of writing [20]. Gluon-gluon coupling also means that e.g. gluons can be radiated by gluons, which then can produce (virtual) quark-antiquark pairs.

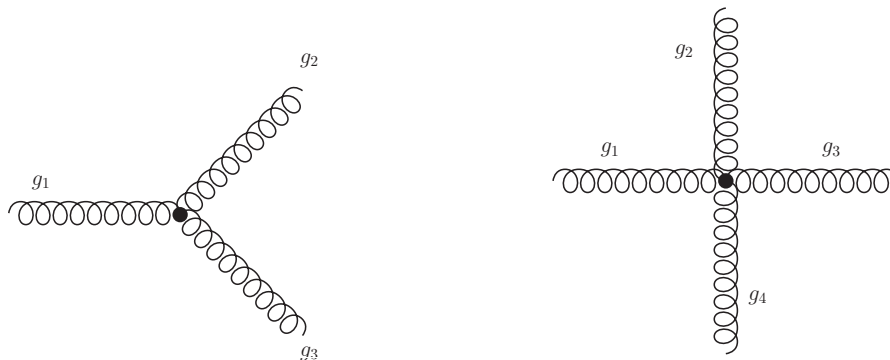


Figure 2.1: Left: three gluon interaction in QCD with the coupling order g_s and right: four gluon interaction in QCD with the coupling order g_s^2 .

Therefore, the momentum fraction of hadrons like the protons is carried not only by the main (valence) quarks but also by gluons and sea quarks (produced by gluons binding the valence quarks). The distribution of momentum fractions of the different types of partons then depends on the energy transfer, Q^2 , and is described by parton distribution functions (PDFs).

2.2 Z Boson Production and Decay at the LHC

The Z boson properties were measured very precisely at the Large Electron-Positron collider (LEP) [25] experiments. LEP was a collider at CERN operating from 1989-2000 with the ability to collide electrons with positrons at center-of-mass energies from the Z pole of up to 209 GeV. Therefore, the Z boson could be produced directly via $e^+e^- \rightarrow Z$. Its mass and width is measured to be [20]:

$$M_Z = 91.1876 \text{ GeV} \pm 0.0021 \text{ GeV} \quad (2.45)$$

$$\Gamma_Z = 2.4952 \text{ GeV} \pm 0.0023 \text{ GeV}. \quad (2.46)$$

Moreover, the decay modes of the Z boson were measured precisely, and the most important ones are summarized in Table 2.3. At the LHC, protons are brought to collision and the Z boson is produced by the interaction of quarks and gluons (partons) within the protons. Such a proton-proton collision at the LHC producing a Z boson is illustrated in Figure 2.2.

Because of the high multijet production rate at hadron colliders, quarks of hadronic decays are difficult to identify within the large multijet background. Therefore, the Z boson can be measured in the leptonic decay modes with the highest precision. The production cross-section depends on the partonic cross-section, $\sigma_{12 \rightarrow \gamma/Z}$, and also on the PDFs, $f_1(x_1, Q^2)$ and $f_2(x_2, Q^2)$, of the proton.

Table 2.3: Summary of most important Z decay modes and branching fractions [20].

Decay mode	Partial width Γ_i [MeV]	Branching fraction Γ_i/Γ_Z [%]
$Z \rightarrow e^+e^-$	83.91 ± 0.12	3.363 ± 0.004
$Z \rightarrow \mu^+\mu^-$	83.99 ± 0.18	3.366 ± 0.007
$Z \rightarrow \tau^+\tau^-$	84.08 ± 0.22	3.370 ± 0.008
$Z \rightarrow \text{leptons}$	251.98 ± 0.31	10.099 ± 0.011
$Z \rightarrow \text{hadrons}$	1744.4 ± 2.0	69.91 ± 0.06
$Z \rightarrow \text{invisible}$	499.0 ± 1.5	20.00 ± 0.06

The production cross-section for Z boson production at the LHC can then be calculated by the convolution of the PDFs and the partonic cross-section:

$$\sigma_{pp \rightarrow \gamma/Z} = \int dx_1 dx_2 \cdot f_1(x_1, Q^2) \cdot f_2(x_2, Q^2) \cdot \sigma_{12 \rightarrow \gamma/Z}(\mu_F, \mu_R, Q^2). \quad (2.47)$$

The PDFs, f_1 and f_2 , were extracted precisely from data of the H1 [26–29] and ZEUS [30,31] experiments at the electron-proton collider Hera, the D0 experiment [32,33] at the Tevatron,

ATLAS and CMS, and other experiments [34]. Those measurements are used to tune the PDF calculations in Monte-Carlo (MC) event generators, which are then used e.g. to simulate production cross-sections in the p - p collisions. PDF distributions for two different low-momentum transfer scales, Q^2 , are shown in Figure 2.3. In addition, the partonic cross-section, $\sigma_{12 \rightarrow \gamma/Z}$, is dependent on the factorization scale, μ_F , the renormalization scale, μ_R , and Q^2 . The complete MC generation process is described in more detail in the next section.

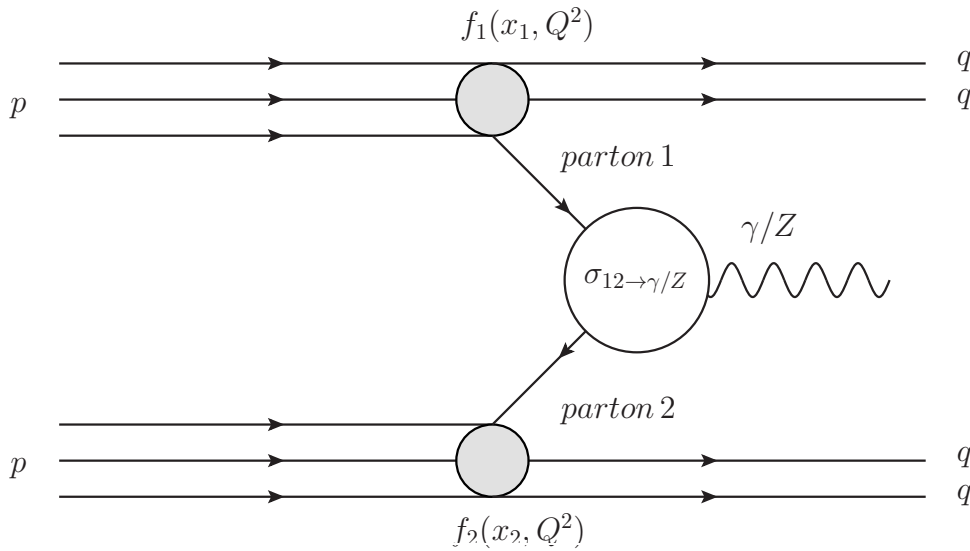


Figure 2.2: Diagram of p - p interaction with the production of a Z boson at the LHC.

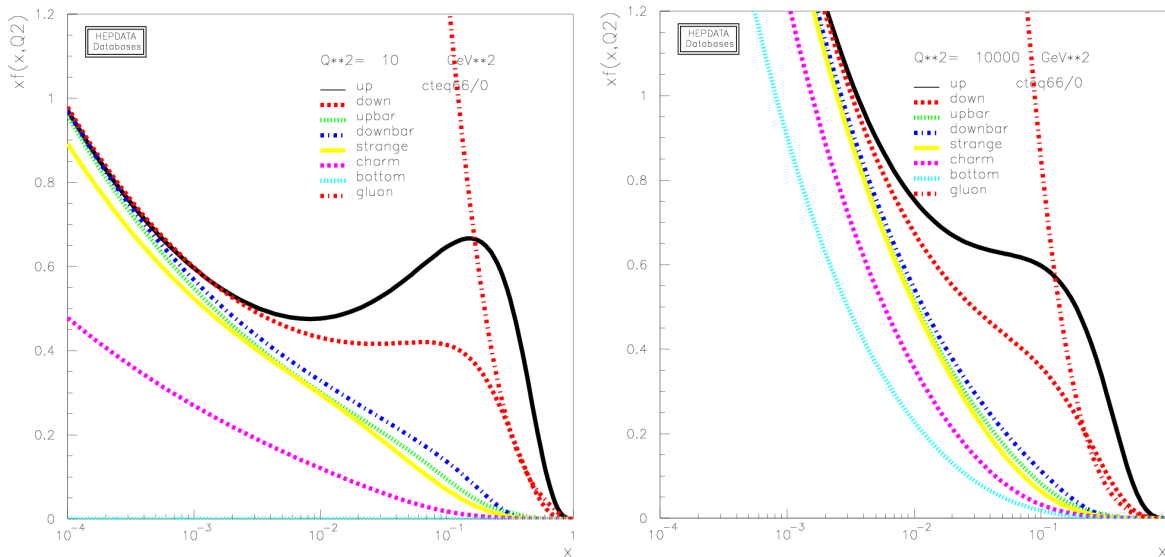


Figure 2.3: PDF distribution parametrizations evolved to different Q^2 values using the CTEQ66 PDF set [34] at $Q^2 = 10 \text{ GeV}^2$ and $Q^2 = 10^4 \text{ GeV}^2$. Shown are the probability density functions times the momentum fraction in dependence of the momentum fraction for the individual quark and gluon contributions of the proton. The parametrizations are performed in next-to-leading order (NLO).

2.3 Event Generation and Simulation

Physics processes at particle colliders can be predicted to some extent by the simulation of collision events and the resulting decay products. Those simulations are based on theoretical calculations. After including the PDFs in the simulations, the first basic step is the calculation of the initial partonic reaction.

2.3.1 The Partonic Process

The partonic process can be calculated by integrating the leading order (LO) matrix element over the allowed phase-space by using electroweak and perturbative QCD calculations. The matrix element in turn can be calculated from the sum of all Feynman-diagrams which contribute to the simulated process. Higher order corrections in QCD arise from initial-state radiation (ISR) or final-state radiation (FSR) of gluons as well as from gluon loop corrections.

Some Feynman-diagrams contributing to the production and decay of the Z boson into leptons are shown in Figure 2.4. The main leading order contributions, quark-antiquark annihilation and Compton-scattering of a quark and a gluon, can be seen in Figures 2.4(a), 2.4(b) and 2.4(c). NLO corrections for the annihilation process in form of a gluon exchange (2.4(d)) and ISR of a gluon (2.4(e)) are illustrated. Two examples for NLO contributions to the QCD Compton process can be seen in 2.4(f) and 2.4(g), as well as a NNLO diagram with a fermion loop in 2.4(h).

In this study, the matrix element event generator ALPGEN [35] is used for an exact calculation of the leading order matrix element in QCD and electroweak interactions for Z - and W boson production at the LHC. Higher order corrections are then modeled by parton shower simulation as performed with HERWIG [36]. It uses the parton shower algorithm which models the ISR and FSR of additional quarks and gluons by Sudakov form factors. These form factors describe the probability that a parton of certain type and momentum fraction propagates from a harder to a softer scale without emitting another parton harder than a defined resolution scale [37]. Inversely, the probability to emit at least one such parton can be obtained. In the case that a NLO generator like MC@NLO [38] is used and connected to a parton shower model, inconsistencies may appear due to double counting of partons from the hard process and from the parton shower. In this case it might be necessary to apply negative weights to some generated events to correct for this.

After simulating the hard (partonic) process, taking the PDFs into account, a set of four-momentum vectors of every real emitted particle is obtained. Those four-momentum vectors are then used for the further simulation process.

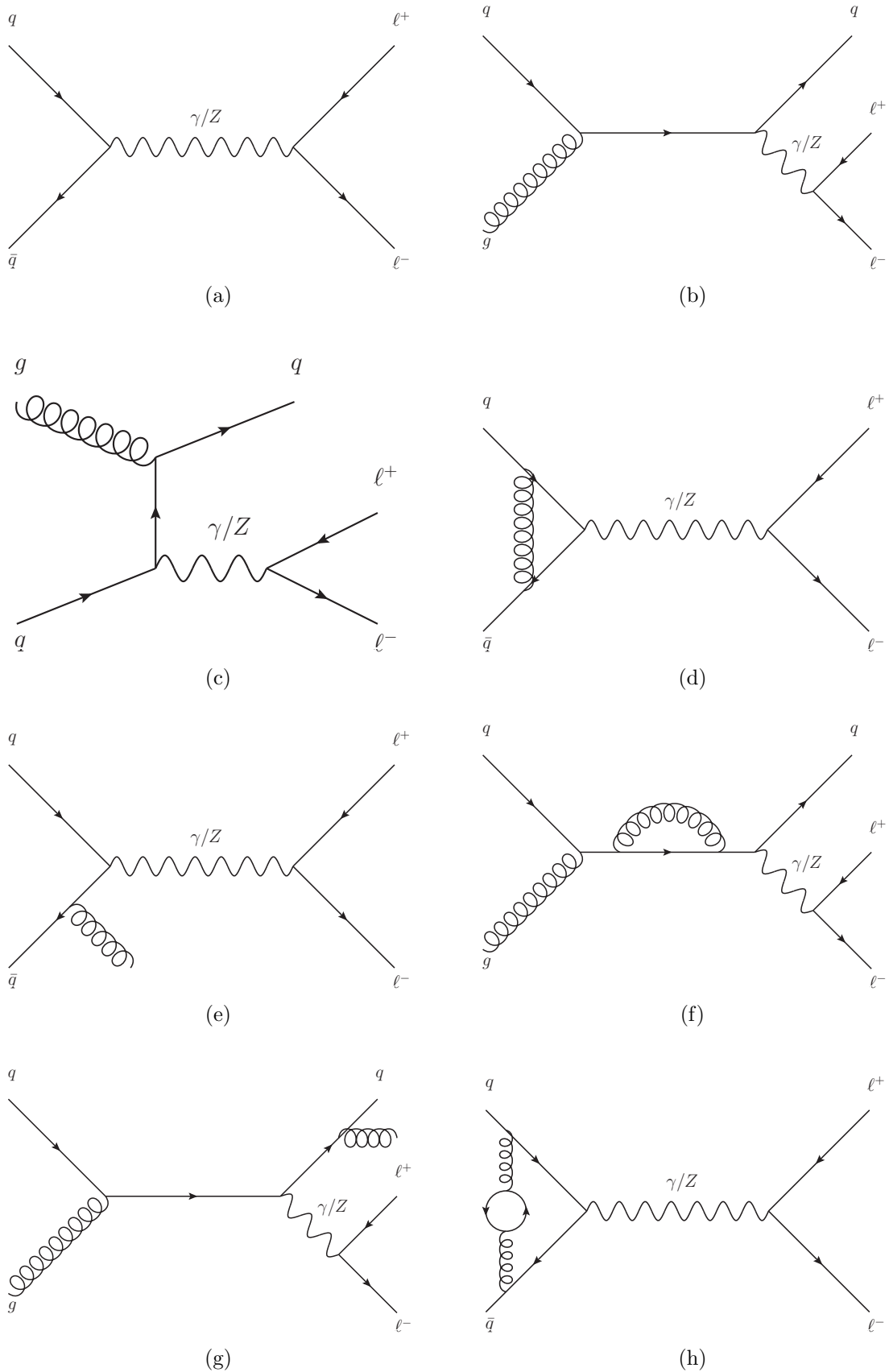


Figure 2.4: Feynman diagrams of Z boson production and decay at the LHC. Quark-antiquark annihilation 2.4(a) and QCD Compton scattering in the s-channel 2.4(b) and in the t-channel 2.4(c) are the contributions in LO. NLO corrections for the annihilation process (2.4(d), ??, 2.4(e)) and for the QCD Compton process (2.4(f), 2.4(g)) as well as a NNLO diagram with a fermion loop (2.4(h)) are shown.

2.3.2 Hadronization

Quarks and gluons are colour charged objects and can therefore not exist as free particles as described previously. They are the products of the hard scattering process but are not the observables to be measured finally. The partons are bound in hadrons again by producing quark-antiquark pairs out of the strong colour potential. This step is called hadronization and is also performed in the MC simulations.

In this study, HERWIG is used for simulating the hadronization process. The program uses the cluster model which splits all outgoing gluons into quark-antiquark or diquark-antidiquark pairs. These bundles of quarks and antiquarks are also called jets. From these jets, colour-singlet clusters are formed, which are then converted into hadrons by a simplifying and fast fragmentation algorithm [36]. It neglects constraints like strong isospin symmetry, but the resulting effects have been found to be too small to be observed in experimental data [36].

Another method is used by the MC generator PYTHIA [39], which uses the Lund string scheme for the fragmentation of partons into hadrons. In principle, it uses virtual colour strings between quark pairs with a potential which increases with the distance between the quarks. If the potential is high enough, another quark-antiquark pair is generated out of the string, which eventually fragment into hadrons.

2.3.3 The Underlying Event

If two partons interact in a p-p collision at the LHC, the remains of the protons are visible in the detector in addition to the hard interaction products and are called "underlying event". It is characterized by a colour connection between the proton remnants and the hard scattered partons, out of which quark-antiquark pairs are produced. This process is also modeled by HERWIG and the partons produced in these soft interactions are again hadronized by the cluster algorithm [36]. Usually, a number of free parameters are used to emulate the underlying event. They can be tuned to describe the experimentally measured data accordingly, as e.g. done with the ATLAS AUET1 tune [40] in this work. HERWIG also uses the external package JIMMY [41] for simulating multi-parton interactions in the soft underlying event.

2.3.4 Detector Simulation

The results of MC generators are used for predictions and comparisons with experimentally measured data. Therefore, it is necessary to perform a full detector simulation with the four-momenta of the particles obtained by the simulation chain described above. The final simulated detector response on a physics process is compared to measured data. This is done by modeling the ATLAS [3] detector in the Geant4 [42,43] framework. The interaction of all produced final state particles with the detector material is emulated. This includes the evolution of electromagnetic as well as hadronic showers in the absorbers and sensitive areas of the detector. Furthermore, the electronic response of the individual detector units is simulated and the obtained signals go through the same shaping and digitization

algorithms as those of measured data, so that the final detector response of simulation and measurements can be compared.

2.4 Cross Section Predictions for Z Boson Production at the LHC

Production cross sections of heavy bosons have been calculated theoretically up to NNLO precision [7]. This is done using several programs, like MCFM [44], FEWZ [45] and ZWPROD [46]. Different approaches are utilized by the various programs and they are used to obtain a combined result and estimation of its uncertainty. MCFM computes boson cross sections in LO and NLO with QCD perturbation expansions. FEWZ calculates W - and Z cross sections for hadron colliders up to NNLO in perturbative QCD and leptonic decays including full spin correlations. ZWPROD gives total inclusive W - and Z production cross sections also in NNLO QCD. For those calculations MSTW and CTEQ [34] PDF sets are used.

The uncertainties on the obtained cross sections are estimated from the missing higher order QCD contributions as well as uncertainties on the PDFs and in the strong coupling strength α_s . By reason of the limited order of perturbative QCD calculation, the calculations are performed at fixed factorization (μ_F) and renormalization (μ_R) scales of a process. The uncertainties are then estimated by varying those scales up and down by a factor of two. The PDF uncertainty contributions are estimated from calculations with different settings of the orthogonal eigenvectors in the parameter space of the PDF fits [7].

The cross section for Z boson production at the LHC depends on the center-of-mass energy, \sqrt{s} , and the allowed mass window of the invariant dilepton mass ($M_{\ell\ell}$). This is typically set to $\approx M_Z \pm 25$ GeV, e.g. ($66 \text{ GeV} < M_{\ell\ell} < 116 \text{ GeV}$) and includes FSR within a cone of $\Delta R < 0.1$ (as defined in (3.2) of Section 3.2) around the leptons. The result obtained for the Z boson production cross section calculation (and its decay into leptons) for $\sqrt{s} = 7$ TeV is [7]:

$$\sigma(Z(\gamma^*) \rightarrow \ell\ell) = (964 \pm 48) \text{ pb} \quad (66 \text{ GeV} < M_{\ell\ell} < 116 \text{ GeV}) \quad (2.48)$$

Also a calculation for a much broader mass window of ($40 \text{ GeV} < M_Z < 2000 \text{ GeV}$) is given for interest, but will be not used for further comparisons [7]:

$$\sigma(Z(\gamma^*) \rightarrow \ell\ell) = (1070 \pm 54) \text{ pb} \quad (40 \text{ GeV} < M_{\ell\ell} < 2000 \text{ GeV}) \quad (2.49)$$

A summary of various production cross sections in p-p as well as \bar{p} -p collisions is given in Figure 2.5. In addition to W - and Z boson cross section it shows the production cross sections of b quarks, top quarks and SM Higgs bosons of three different assumed masses. Dotted lines indicate the conditions of the Tevatron and three different LHC energies. With an increased LHC center-of-mass energy, the cross section given in (2.48) would also increase to 1437 pb for $\sqrt{s} = 10$ TeV and to 2061 pb for $\sqrt{s} = 14$ TeV [7].

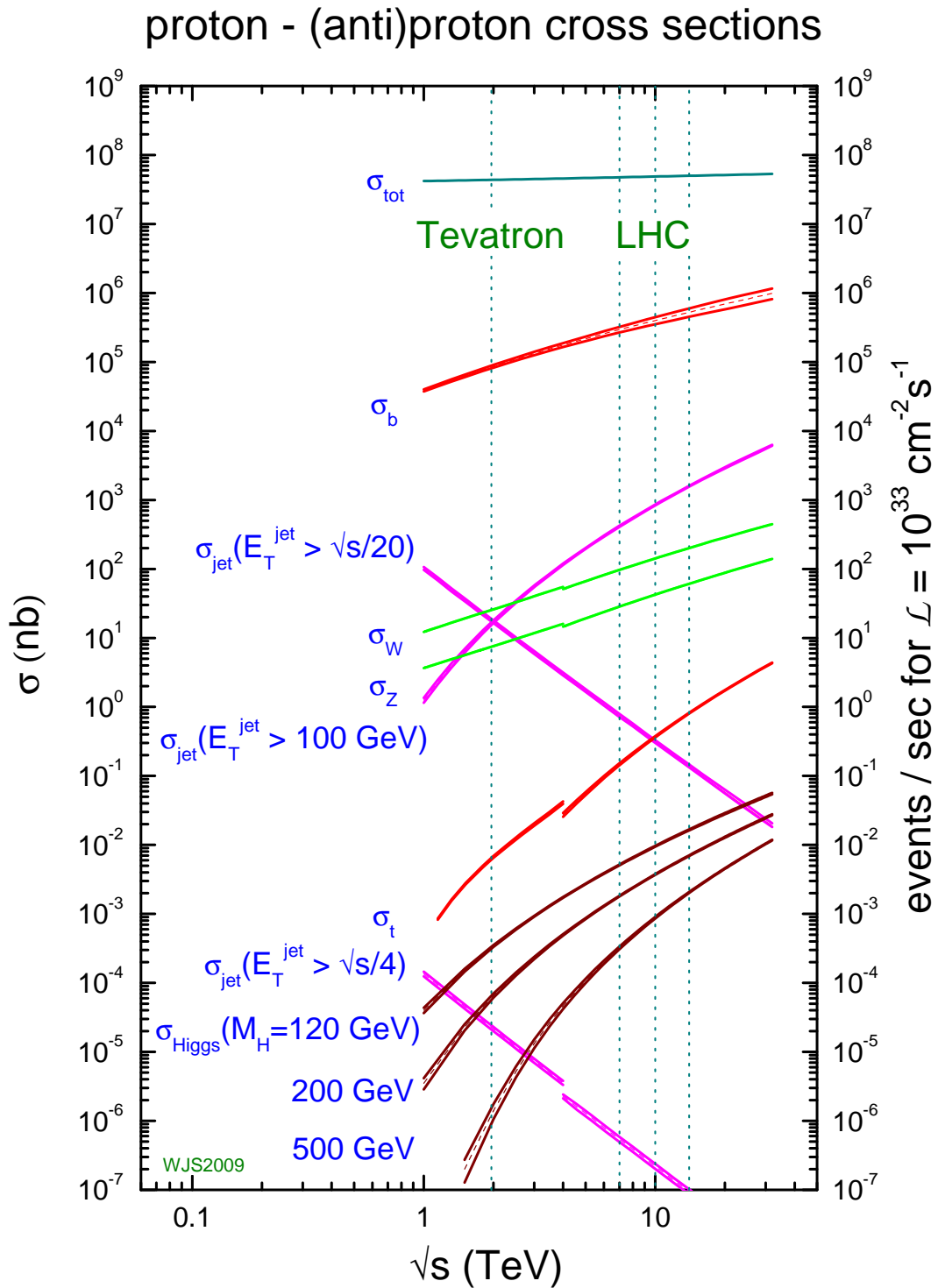


Figure 2.5: Standard Model production cross sections at the LHC and the Tevatron [47]. In addition to W - and Z boson cross section it shows the production cross sections of b quarks, top quarks and SM Higgs bosons of three different assumed masses. Dotted lines indicate the conditions of the Tevatron and three different LHC energies. The estimated theoretical uncertainties are indicated by error bands.

The main background processes to Z boson studies are the production of two or more high energetic QCD jets (multijet), W boson and top quark production. The cross section and with it the production rate of multijet events is several orders of magnitude higher than that of Z bosons. Therefore, efficient suppression methods are required for multijet events. As illustrated in Figure 2.5, the production rate of W bosons is roughly 10 times higher than that of the Z boson. Hence, this process is also an important background to study.

3 The LHC and the ATLAS Experiment

3.1 The Large Hadron Collider

The Large Hadron Collider (LHC [48, 49]) is a proton-proton collider designed for a center of mass energy of $\sqrt{s} = 14$ TeV. It is located at CERN (European Organization for Nuclear Research) on the boarder between France and Switzerland, near Geneva, in the tunnel of the previous Large Electron Positron Collider (LEP). The LHC is designed as double synchrotron with a circumference of 26.7 km and two separate beam pipes for the two proton beams in both directions. The protons are injected with an energy of 450 GeV and accelerated to a maximal energy of 7 TeV in each direction. In 2011 running, the center of mass energy was $\sqrt{s} = 7$ TeV and the maximal energy reached at the time of writing was $\sqrt{s} = 8$ TeV (4 TeV per proton beam). Not only protons, but also heavier ions, like lead, are accelerated and collided at the LHC.

The LHC beam energy is limited by the magnetic field of dipole magnets which keep the protons on the nearly circular path. In the LHC tunnel, 1232 superconducting dipoles are installed. Each is about 14 m long, cooled with superfluid helium down to 1.9 K and is designed to reach a magnetic field of up to 8.3 T. In addition, approximately 3700 multipole magnets for corrections and focusing of the beams are installed. The acceleration and compensation of synchrotron radiation losses of the protons is provided by superconducting high frequency cavities operating with 2 MV/m and 400.8 MHz.

As the LHC is a collider of same-sign charged particles, the magnetic dipole fields need to be in opposite directions in order to bend both beams on the orbit. This is reached with two separate beam pipes within one housing. One cryogenic system and one magnetic field configuration is covering both beam pipes. A schematic view is shown in Figure 3.1.

Before the protons (or ions) are injected into the LHC, they are pre-accelerated by a system of smaller accelerators. A scheme of the full accelerator chain can be seen in Figure 3.2. Protons from a hydrogen source are accelerated by a linear accelerator (LINAC) to an energy of 50 MeV and then injected to the proton synchrotron booster (PSB). It configures one high intensity proton bunch and accelerates it further to 2.1 GeV. Six bunches of the PSB are then injected into the proton synchrotron (PS) in two steps. There they are split into 72 bunches, accelerated to 26 GeV and injected to the super proton synchrotron (SPS). Three fills of the PS sum up to one fill of the SPS. The SPS is only responsible for the further acceleration to 450 GeV, which is the injection energy of the LHC. Finally, 13 SPS

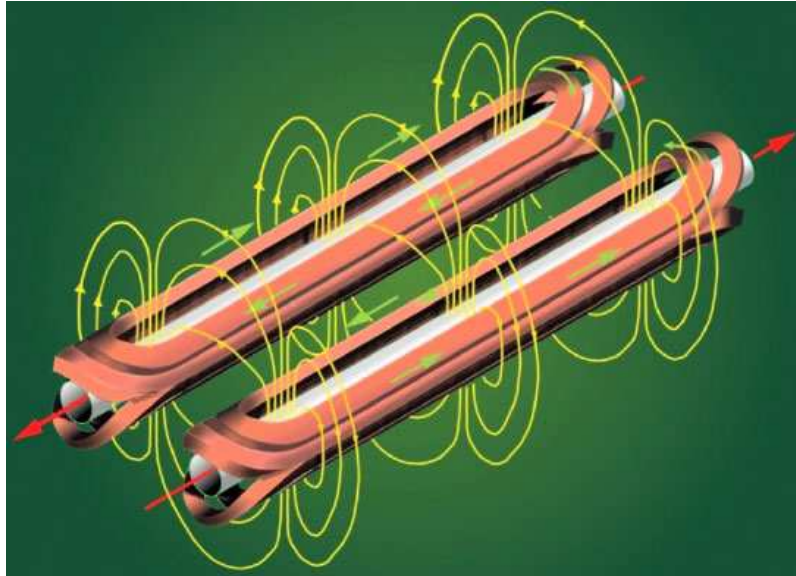


Figure 3.1: The LHC magnetic dipole field configuration [50]. As particles of the same charge are collided, the magnetic dipole fields for both beams have to be in opposite directions. The field strength of the superconducting magnets is up to 8.3 T.

fills build one LHC fill and the protons are accelerated to their final energy. The proton bunches are not distributed uniformly along the LHC but in bunch trains with a fixed bunch spacing within the trains (75 ns or 50 ns in the 2011 data taking) and larger gaps between the trains. Within these gaps the magnets for injections or beam dumping are ramped.

In contrast to an electron or positron collider, the synchrotron radiation losses of the protons are small at the LHC leading to high reachable energies on the one side. The disadvantage on the other side are the collisions of composed objects. This results in less clean collision event environments compared e.g. to an electron-positron-collider like LEP. Also the initial energy in longitudinal direction is unknown since the fundamentally interacting particles are the constituents of the protons, the quarks and gluons. Their energy fraction of the proton is unknown and can only be described on a statistical basis using the parton distribution functions (PDF). All this leads to a very challenging experimental environment for the LHC experiments.

After acceleration, the LHC works as a storage ring with four interaction points, where the protons of both beams collide. The lifetime of both beams is between 10 and 20 hours. Around the interaction points the four LHC experiments for measuring the collision events are installed, namely are ATLAS [3], CMS [4], LHCb [52] and ALICE [53]. The arrangement of the experiments at the LHC is also shown in Figure 3.2. ATLAS and CMS are designed as multipurpose detectors to cover a wide spectrum of physics analyses. LHCb is a special dedicated forward experiment for measuring CP violation and rare processes in B-meson decays. ALICE, finally, is designed to measure heavy ion collisions and study especially the properties of the quark-gluon plasma state. In the following, the ATLAS detector is described in more detail.

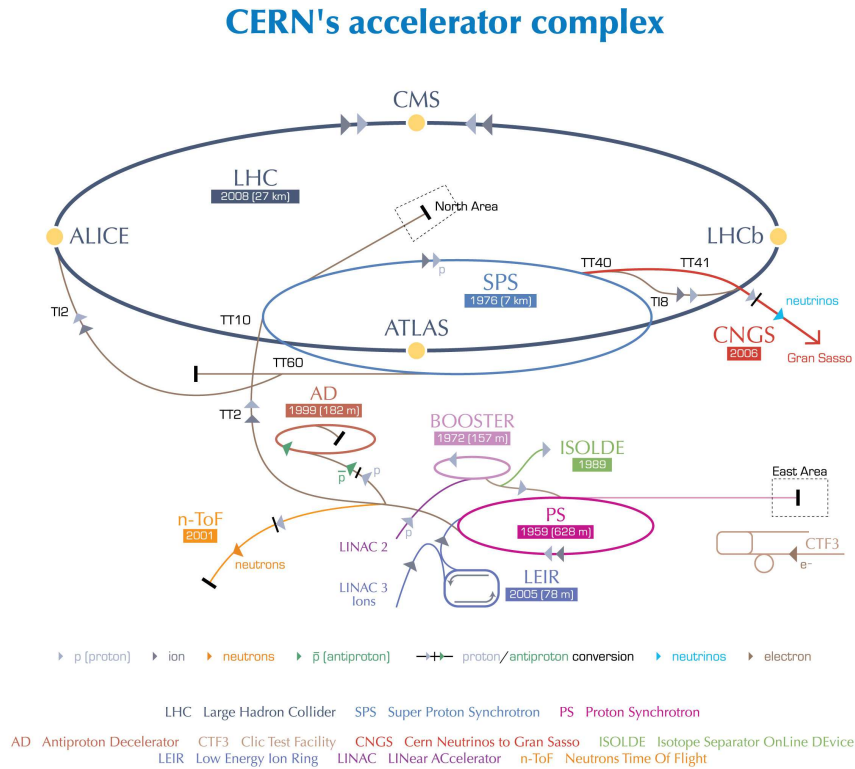


Figure 3.2: Scheme of the accelerator system at CERN [51]. The four LHC experiments are indicated as yellow dots. After multiple pre-accelerator steps, the SPS induces the particles in both directions of the LHC at 450 GeV, where they are accelerated to their final energy.

3.2 The ATLAS Experiment

The ATLAS (A Toroidal LHC ApparatuS) detector [3] is a particle detector experiment installed at one of the four interaction points of the LHC. With its design as multipurpose detector, it covers nearly the full solid angle and is able to detect particles of all known types except neutrinos or other neutral, weakly interacting particles. This is obtained with a cylindrical layout and onion-skin structure of various detector components. A schematic picture of the ATLAS detector is shown in Figure 3.3. Overall, the detector is of 44 m length and 25 m height.

The chosen coordinate system with the point of origin at the interaction point is introduced first. The cartesian coordinate system is defined with the positive x coordinate pointing to the center of the LHC ring, the y axis pointing upwards and the z axis along the beam pipe to obtain a right-handed system. Commonly used are the azimuthal angle ϕ and the pseudorapidity η , defined as

$$\eta = -\ln\left(\tan\frac{\theta}{2}\right), \quad (3.1)$$

with θ being the polar angle. The pseudorapidity has the property that only the direction

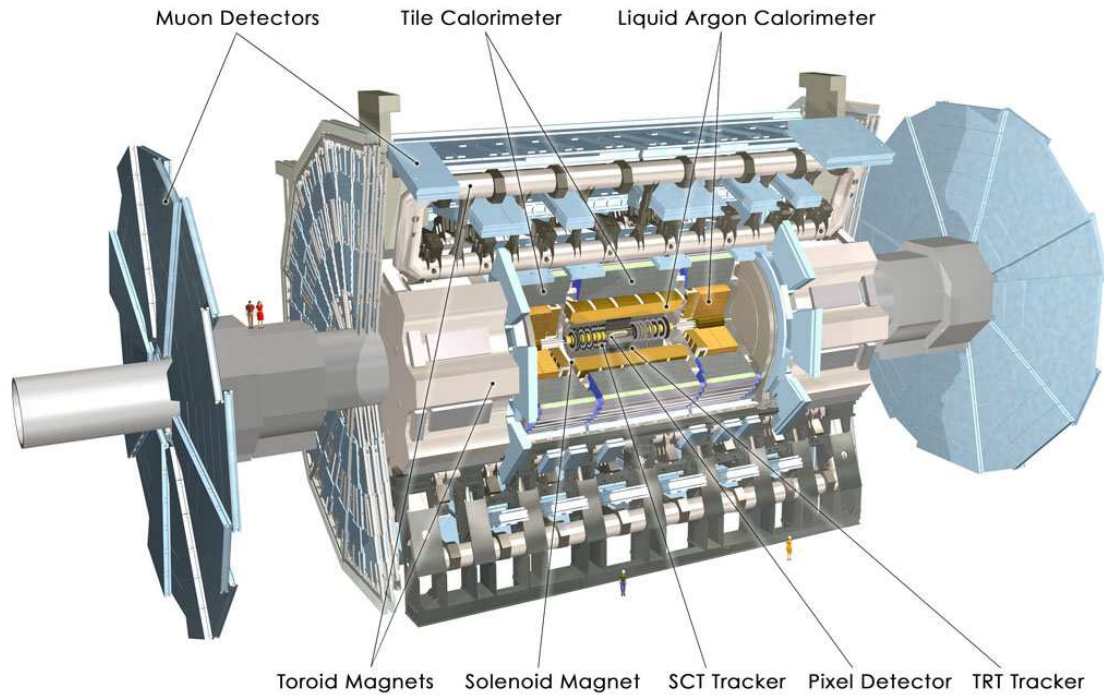


Figure 3.3: The ATLAS detector with labels for the most important elements [3]. It is designed with an inner detector for particle tracking and charge identification in the center, followed by an electromagnetic and hadronic calorimeter and surrounded by a muon spectrometer to reach maximum coverage.

of flight through the detector needs to be measured, if the mass of the particle is neglected. Therefore, care must be taken in the case that the particle mass is not negligible to its energy. Furthermore, the fluence of produced particles in inelastic p-p collisions is about constant per pseudorapidity interval in the central pseudorapidity region. With these two coordinates a two dimensional distance can be defined as

$$\Delta R = \sqrt{(\Delta\eta)^2 + (\Delta\phi)^2}, \quad (3.2)$$

whereas ϕ is given in multiples of 2π . Often used is the transverse momentum of a particle

$$p_T = \sqrt{p_x^2 + p_y^2}. \quad (3.3)$$

It plays a special role because momentum conservation can only be applied in the transverse plane, and the longitudinal momentum of the hard p-p collision process is a priori unknown as it was also described in Section 3.1.

In the inner part of the ATLAS detector, systems for particle tracking are installed followed by calorimeters for energy measurement of various particle types. In the outer part a huge muon spectrometer with a toroidal magnetic system is installed, specially dedicated for precision measurements of muons. These different subdetectors are described in more detail in the following sections.

3.2.1 The Inner Detector

The inner detector is responsible for measuring vertices, tracks of charged particles, and, from their curvature in the magnetic field, the momenta of charged particles. Therefore, the inner detector is included in a superconducting solenoid providing a magnetic field of 2 T, which is of 5.3 m length and 2.5 m diameter. The inner detector consists of three parts: the pixel detector (PIX), the silicon microstrip tracker (SCT) and the transition radiation tracker (TRT). An overview of the inner detector is given in Figure 3.4.

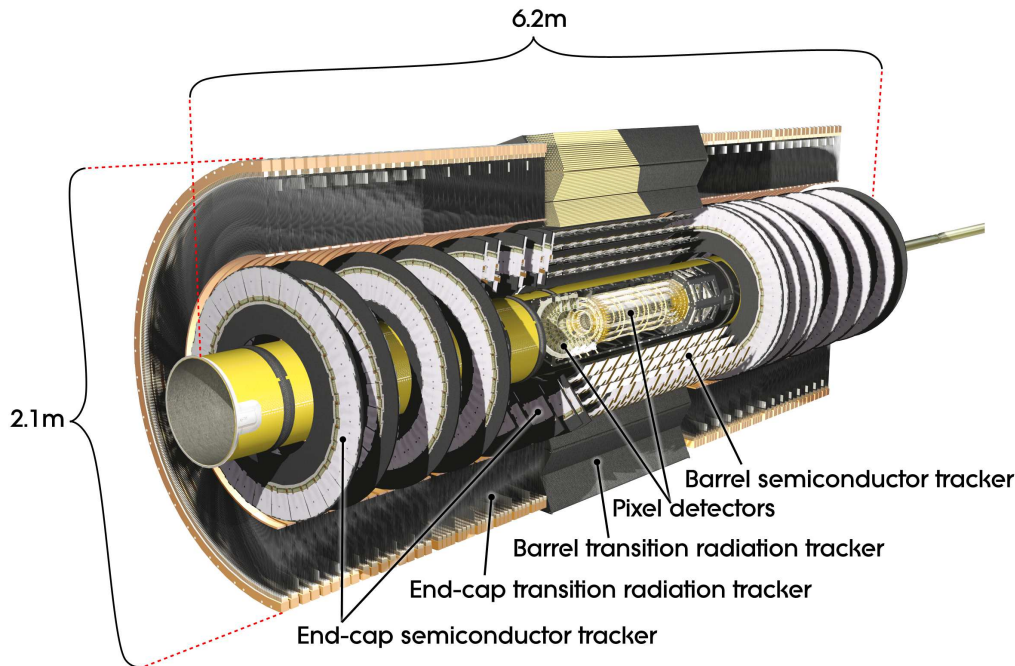


Figure 3.4: Schematic cut-away view of the inner detector of the ATLAS experiment with its three components visible, the pixel detector, the silicon microstrip tracker and the transition radiation tracker [3].

In the nominal luminosity scenario, around 1000 particles are produced at the interaction point every 25 ns. To resolve all produced tracks and vertices, a high granularity and short readout time are necessary. The silicon pixel detector around the interaction point reaches pixel sizes of $50 \times 400 \mu\text{m}^2$ with a tracking accuracy of $10 \mu\text{m}$ in ϕ and $115 \mu\text{m}$ in z . A region of $|\eta| < 2.5$ is covered with approximately 80.4 million readout channels. The pixel layers are arranged such that usually one track hits three detector layers. The innermost layer of the pixel detector is only 5 cm away from the beam pipe in transverse direction and is especially important for reconstructing primary and secondary vertices, which can be then used for tau-lepton or b-quark identification. Therefore, it is also called vertexing layer or b-layer.

For the SCT, two strip layers are needed for each space point and every track hits in average eight layers, so that 4 space points can be reconstructed. The SCT uses strip sensors of 6.4 cm length and $80 \mu\text{m}$ width. It uses 6.3 million readout channels and reaches accuracies of $17 \mu\text{m}$ in ϕ and $580 \mu\text{m}$ in z . The region of $|\eta| < 2.5$ is covered by the SCT.

The TRT, finally, provides typically 36 hits per track and covers a range of $|\eta| < 2.0$. It consists of 4 mm diameter straw tubes interleaved with fibres in the barrel and with foils in the endcap, which reach a single hit precision of $130 \mu\text{m}$ in the ϕ -plane. In the barrel region the tubes run parallel to the beam pipe and are divided at $\eta = 0$, while in the end-cap region they are arranged radially in wheel structures. The TRT uses in total 0.35 million readout channels. Charged particles passing the TRT produce transition radiation, which is measured and used mainly for electron identification. As the TRT needs to distinguish between minimum-ionizing particles and transition radiation, its front-end electronics use two different discriminators. One operates at low-threshold of $\approx 250 \text{ eV}$ for measuring minimum-ionizing signals, and one is run at high-threshold of $\approx 6 \text{ keV}$ for transition radiation measurement. Electrons with energies higher than 2 GeV usually produce between seven and ten high-threshold hits in the TRT. The low- and high-threshold hits of the TRT are relevant for particle identification in any physics analysis.

The inner detector is special dedicated to identify electrons and to separate them from pions by measuring transition-radiation photons with the straw tubes. Also the measurement of vertices and impact parameters allows the identification of heavy-flavour quark decays or tau lepton decays. At approximately $\eta = 0$, the performance is significantly reduced due to the crack region. Therefore, in physics analyses, which rely on good inner detector performance, it might be necessary to exclude this region from the analysis.

3.2.2 The Electromagnetic Calorimeter

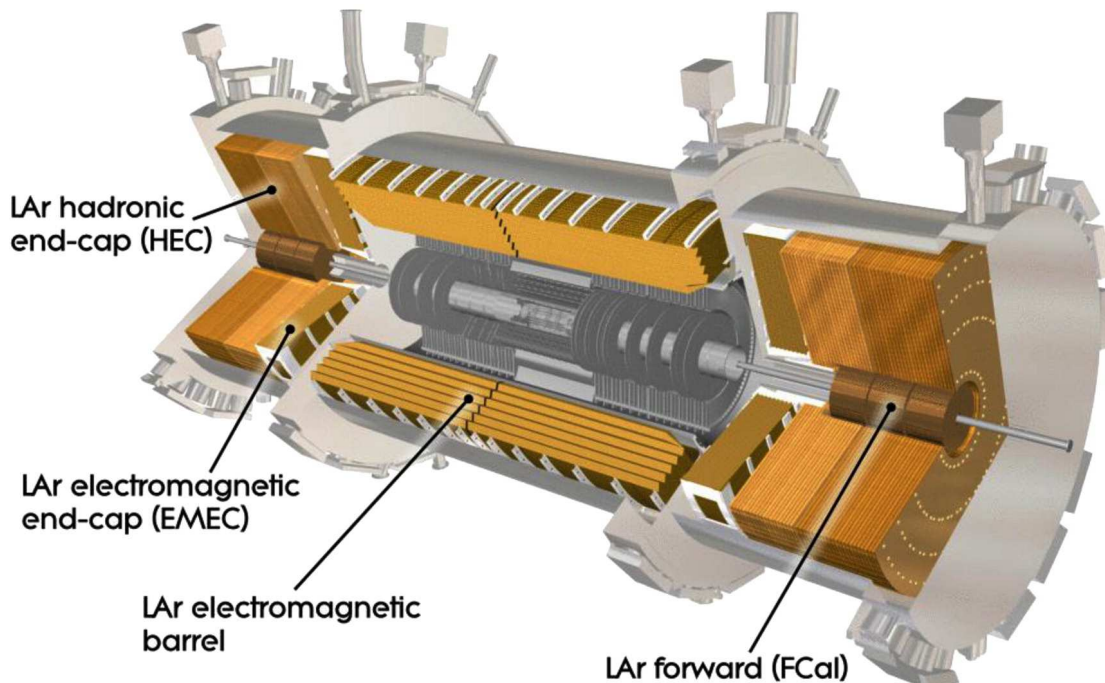


Figure 3.5: Schematic cut-away view of the electromagnetic calorimeter of the ATLAS experiment [3]. The EM barrel calorimeter is housed in a central cryostat, whereas the EMEC, the HEC and the FCal are housed in two endcap cryostats.

The liquid-argon (LAr) calorimeters of ATLAS are described here in more detail as a testbeam study of an upgrade scenario of the endcap and forward parts is described in Chapter 4. The LAr calorimeter consists of four parts: electromagnetic (EM) barrel, EM endcap (EMEC), hadronic endcap (HEC) and forward calorimeter (FCal). The HEC (as well as and parts of the FCal) belongs to the hadronic calorimetry and is further described in Section 3.2.3. A schematic overview of the LAr calorimeter system is shown in Figure 3.5.

The EM barrel part consists of two half barrels with a gap of 4 mm in between at $\eta = 0$ and covers a range of $|\eta| < 1.475$. The EMEC consists of an inner and an outer ring on each side and ranges from $|\eta| = 1.375$ to $|\eta| = 3.2$. Outside of that, the HEC covers $1.5 < |\eta| < 3.2$ and is divided into two segments. The FCal, finally, is responsible for the very forward region of $3.1 < |\eta| < 4.9$ and its three layers, FCal1, FCal2 and FCal3, are installed inside of the HEC.

The EM barrel calorimeter uses alternating layers of lead as absorbing material and LAr as active material. The layers are shaped in an accordion structure as illustrated in Figure 3.6. The accordion shape leads to a full and homogeneous coverage in ϕ .

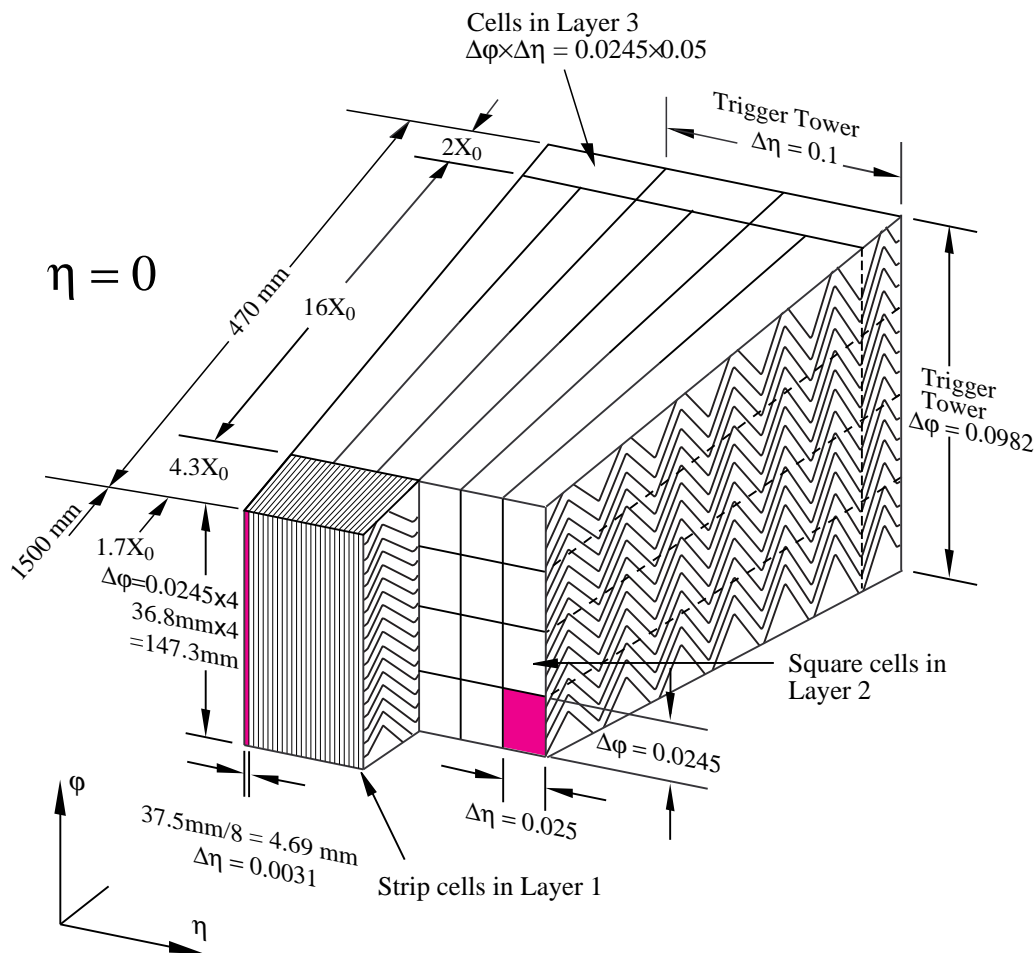
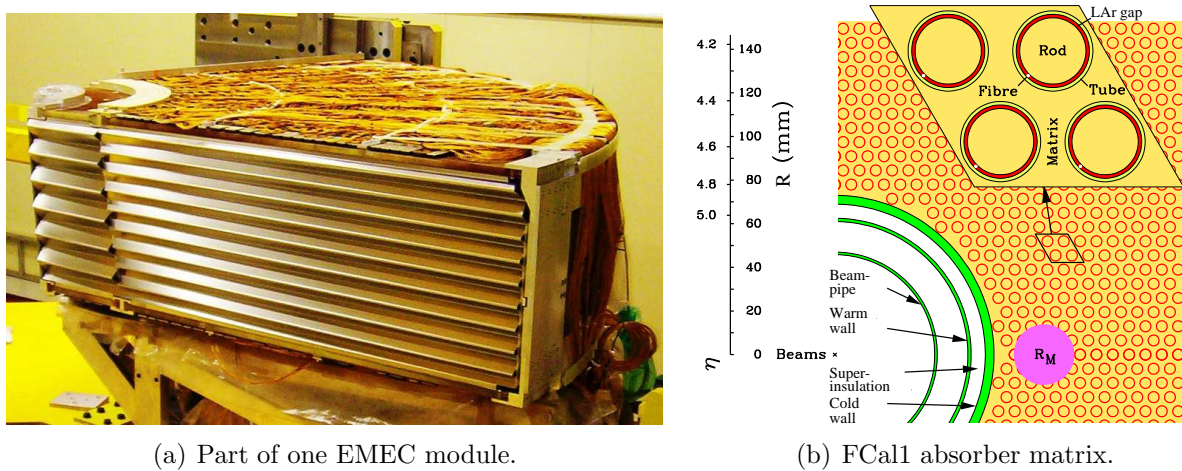


Figure 3.6: Schematic view of the accordion shape structure of the LAr barrel calorimeter [3]. The granularity of the readout cells for each of the three layers is indicated. Also the size of the level 1 trigger towers of about $\Delta\eta \times \Delta\phi = 0.1 \times 0.1$ is illustrated.

Each half barrel is made of 1024 absorbers with LAr filled gaps and readout electrodes in between. These drift gaps are 2.1 mm thick, which leads to 450 ns drift time for electrons at the nominal 2 kV operation voltage applied at the gaps. The radial thickness of the barrel modules is between 22 electromagnetic radiation lengths (X_0) in the center and 33 X_0 at the edge. The barrel modules are divided into three layers in depth (front, middle and back) and also in 3424 readout cells to reach a high granularity.

The EMEC also uses the accordion structure, but the drift gaps of the coaxial wheels are not constant for geometrical reasons. They become bigger from inner to outer sections due to the increased radius and vary between 0.9 mm and 3.1 mm. A similar structure as for the barrel with absorbers interleaved with readout electrodes is used. A picture of one EMEC module can be seen in Figure 3.7(a).



(a) Part of one EMEC module.

(b) FCal1 absorber matrix.

Figure 3.7: Left: Photograph of one side of the EMEC module with its accordion shaped structure. The two separate rings, inner ring and outer ring, are visible. Right: Scheme of the FCal1 absorber matrix around the beam pipe in perpendicular view to the beam axis. One tube group is shown with higher detail and the Moliere-radius R_M (radius of a cylinder containing 90% of the shower energy on average) is also indicated [3].

The disjunction of the two wheels is at $|\eta| = 0$ and of 3 mm width. Each EMEC module is between 24 X_0 and 38 X_0 thick. It is divided in depth in two ($2.5 < |\eta| < 3.2$) or three ($1.5 < |\eta| < 2.5$) longitudinal layers. The first layer consists of strips divided in the $|\eta|$ direction. The granularity of the middle layer is with $\Delta\eta \times \Delta\phi = 0.025 \times 0.025$ the same as for the barrel calorimeter, and the third layer is of twice coarser granularity in η . Each EMEC module provides 3984 readout channels. To obtain a linear detector response in $|\eta|$, despite the increasing LAr gaps, the applied HV decreases to higher $|\eta|$ and lower radii. It is between 1.0 kV and 2.5 kV. The exact values are summarized in Table 3.1.

The FCal, finally, is divided into one electromagnetic part (FCal1) and two hadronic parts (FCal2, FCal3). It is located in the forward region close to the beam pipe at high η and thus is exposed to the highest particle flux densities. The radiation length of the electromagnetic FCal1 is of the order of 28 X_0 . It uses an absorber matrix made of copper which holds copper tube electrodes. Within the tubes a rod with signal pin and a LAr

Table 3.1: Properties and operating parameters of the ATLAS LAr calorimeters [3].

Module	Barrel	EMEC		FCal			HEC
		outer ring	inner ring	FCal1	FCal2	FCal3	
Coverage	$ \eta < 1.52$	$1.375 < \eta < 2.5$	$2.5 < \eta < 3.2$	$3.1 < \eta < 4.9$			$1.5 < \eta < 3.2$
Number of layers	3	3	2	1	1	1	4
Radiation thickness	$22 - 33 X_0$	$24 - 38 X_0$	$26 - 36 X_0$	$28 X_0$	$\approx 7.3 \lambda$		$\approx 10 \lambda$
High Voltage [V]	2000	1000 - 2500	1800 - 2300	250	375	500	1800
Readout channels	101760	62208		3524			5632

gap between rod and tube is inserted. The LAr gaps are with $250 \mu\text{m}$ much smaller than those in the barrel and endcap calorimeters, leading to a short drift time of the electrons of about 50 ns. This is necessary to keep the signal lengths short, because of the high particle densities and thus increased positive ion buildup probability. In total the FCal1 consists of approximately 12000 tube electrodes, where four of them are grouped together to one readout channel. A scheme and a picture of the FCal1 module is shown in Figure 3.7(b).

The readout of the LAr calorimeters is described in more detail. The LAr front-end electronics is installed at the outer side of the cryostats and provide shaping and sampling of the raw detector signals as well as calibration electronics. The digitized data is sent with the LHC bunch-crossing rate of 40 MHz to the off-detector electronics, installed outside the detector cavern about 70 m away from the detector. Also the construction of trigger towers from individual channels is performed in the front-end electronics and sent to the L1 trigger processor. The off-detector electronics includes the read-out drivers which are processing and formatting the data of the front-end boards for online monitoring and sending to the data acquisition (DAQ). Here, the energy and the signal timing is calculated for each cell. A scheme of the readout can be seen in Figure 3.8.

The energy of an object is measured by reconstructing the signal amplitude of the readout cells and summing up all cells, which belong to the object. In normal ATLAS data taking operation, only 5 of the 25 ns separated samples are used for the energy (and timing) measurement, which is sufficient for an adequately reduced noise level [3]. For commissioning and test purposes, up to 32 samples can be used.

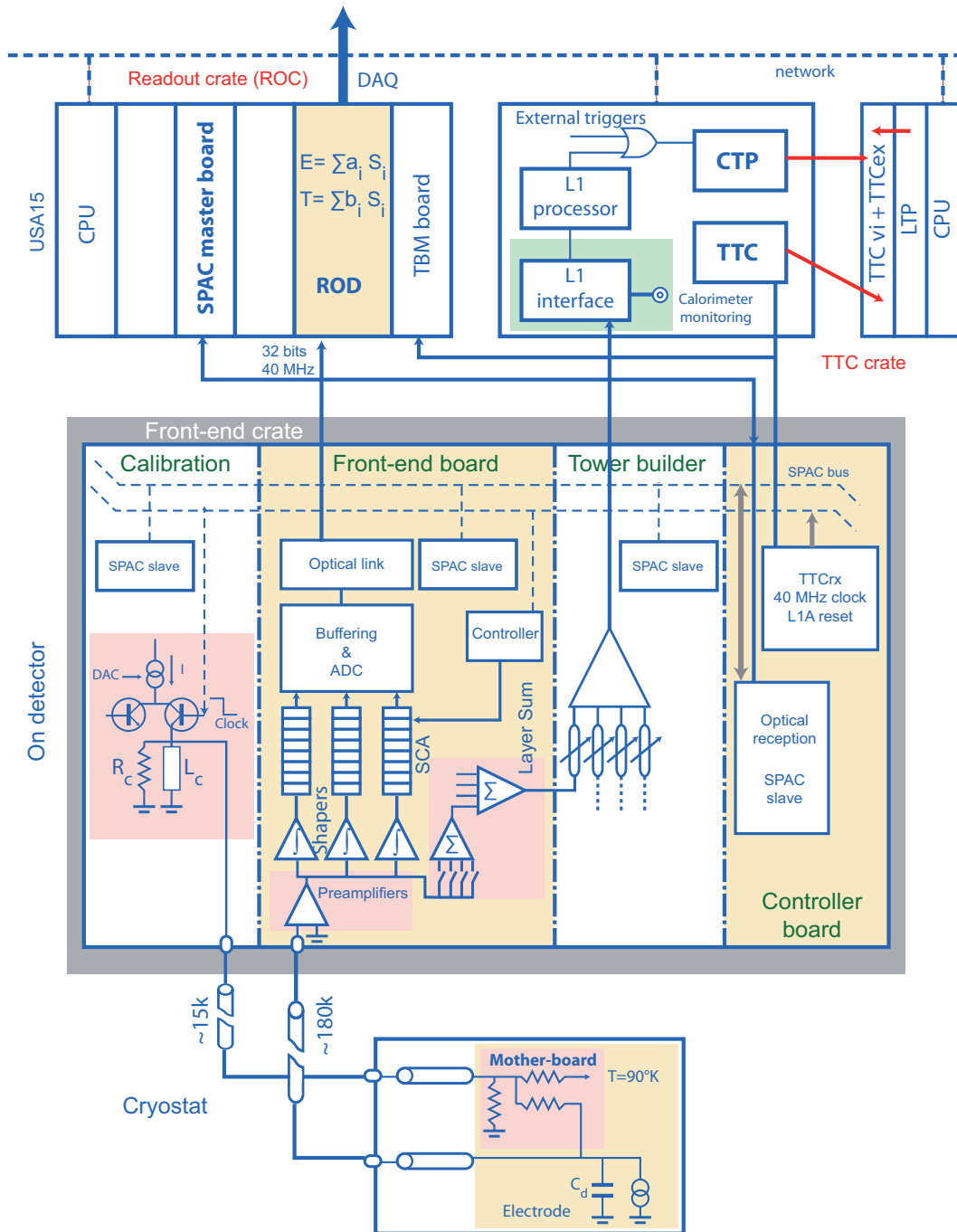


Figure 3.8: Scheme of the overall LAr detector readout electronics. The bottom part shows the cold electronics installed within the cryostat. The middle part visualizes the on-detector front-end boards mounted at the outer side of the cryostats together with boards for calibration and tower building. The top part shows the off-detector electronics with the readout driver (ROD) boards, LAr tower-builder boards and L1 trigger electronics. They are installed outside the detector cavern and get their data at 40 MHz from the front-end electronics [3].

3.2.3 The Hadronic Calorimeter

Hadronic calorimetry in ATLAS is divided into three parts: the hadronic tile calorimeter in the barrel (tile), the HEC and the FCal2 and FCal3 modules in the forward regions. The HEC and the FCal parts use LAr technology, which was described in Section 3.2.2, while the tile is a sampling calorimeter using steel as absorber and scintillating tiles as the active material. It consists of a barrel part covering $|\eta| < 1.0$ and two extended barrel parts covering $0.8 < |\eta| < 1.7$. The tile is located directly outside of the LAr calorimeter cryostats. An overview of the hadronic calorimeters together with the EM ones can be seen in Figure 3.9.

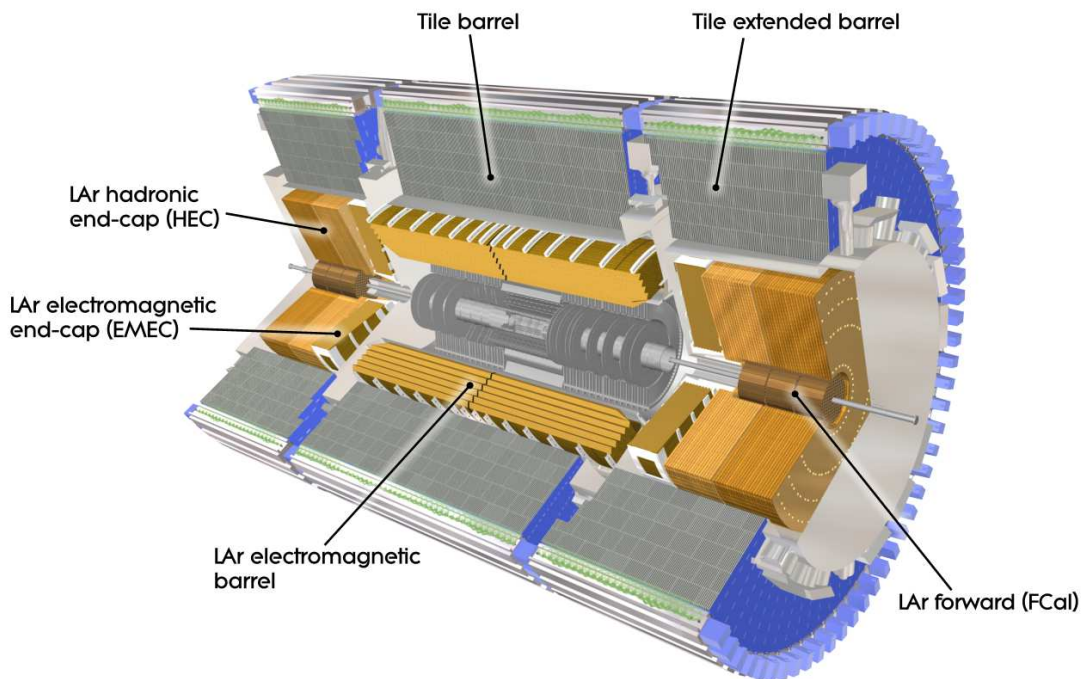


Figure 3.9: Cut-away view of the hadronic calorimeter of the ATLAS experiment around the LAr calorimeters. It is a steel-scintillator sampling calorimeter and consists of the three modules, the barrel part and the two extended barrel modules [3].

The tile calorimeter is divided into three layers in depth. At the transverse region of $|\eta| = 0$, it is 9.7 hadronic interaction lengths, λ , thick. Optical fibres are installed for the readout at the edges of the scintillating tiles. They apply wavelength shifting and are connected to two separate photomultiplier tubes (PMTs), which are, together with all front-end electronics, housed in 1.4 m long aluminium cases, called drawers. Readout cells similar to the LAr calorimeters are constructed by grouping the fibres η for the PMTs. The PMTs signals are then grouped and summed in $\Delta\eta \times \Delta\phi = 0.1 \times 0.1$ trigger towers and are digitized and stored in local pipeline memories. If the event is selected by the trigger, they are sent via optical fibres to the off-detector read out drivers (RODs).

The HEC covers the region of $1.5 < |\eta| < 3.2$ and is divided into two wheels, similar to the EMEC. Each wheel includes two layers in depth, which is a total of four layers for the HEC. It also uses copper as absorber material and LAr gaps of 8.5 mm thickness as active material. To exclude gaps in the detection coverage of particles, it overlaps slightly with the tile in the inner and with the FCal in the outer region. A high voltage of 1800 V is applied at the LAr gaps to obtain a drift time of 430 ns of the electrons. The granularity of the readout cells is $\Delta\eta \times \Delta\phi = 0.1 \times 0.1$ for $\eta < 2.5$ and $\Delta\eta \times \Delta\phi = 0.2 \times 0.2$ for $\eta > 2.5$. The total number of readout channels is 5632.

In the very forward region, the FCal2 and FCal3 modules are responsible for the hadronic calorimetry. In contrast to their EM counterpart, the FCal2 and FCal3 modules use tungsten as absorber to increase shower containment and reduce the lateral extend of hadronic showers. The LAr gaps are of 0.376 mm (FCal2) and 0.508 mm (FCal3) thickness. Further parameters of the FCal and also the HEC are summarized in Table 3.1, together with those of the other LAr calorimeter modules. The small FCal gaps compared to the barrel ones lead to an acceptable rate of positive ion build-up, even at the high particle flux of the very forward region. In addition, the radiation thickness is increased with that design, which shields the forward muon spectrometer. The tube structure of the absorber matrix is similar to that of the FCal1. The number of readout channels is reduced for the FCal2 and FCal3 by grouping not only four, but six (FCal2) or nine (FCal3) tubes to one readout channel.

3.2.4 The Muon Spectrometer

The muon spectrometer is the outermost layer of the ATLAS detector. Therefore, the most of the electromagnetically and hadronically interacting particles like electrons, photons or hadrons are absorbed already in the calorimeters. Besides the undetectable neutrinos, muons are the only particles which can reach the muon spectrometer with a high probability. This is due to their long flight length and small interaction rate with detector material. Hence, detected signals in the muon spectrometer can be assigned to muon candidates.

The muon system is based on several layers of tracking chambers combined with a strong magnetic field. The overall layout of the muon spectrometer can be seen in Figure 3.10. The magnetic field is produced by one large air-core toroid magnet in the barrel region and two end-cap toroid magnets. The orientation is such that the magnetic field is orthogonal to the majority of the muon trajectories. An overview of the magnet system is given in Figure 3.11. The magnetic field produced is of about 0.5 T for the barrel toroid and 1.0 T for the end-cap toroids.

The bent muon tracks are measured by typically three layers of detection chambers of different types. Two types are used for the precision measurement itself while additional two types form the muon trigger system. Monitored Drift Tubes (MDT) are used for measuring the track coordinates with high accuracy over a wide η range. Cathode Strip Chambers (CSC) have a higher granularity to cover the larger rapidity range of $2.0 \leq \eta \leq 2.7$. Resistive Plate Chambers (RPC) and Thin Gap Chambers (TGC) are used for the trigger system in the barrel region and in the end-cap region, respectively, to cover a range of $\eta \leq 2.4$.

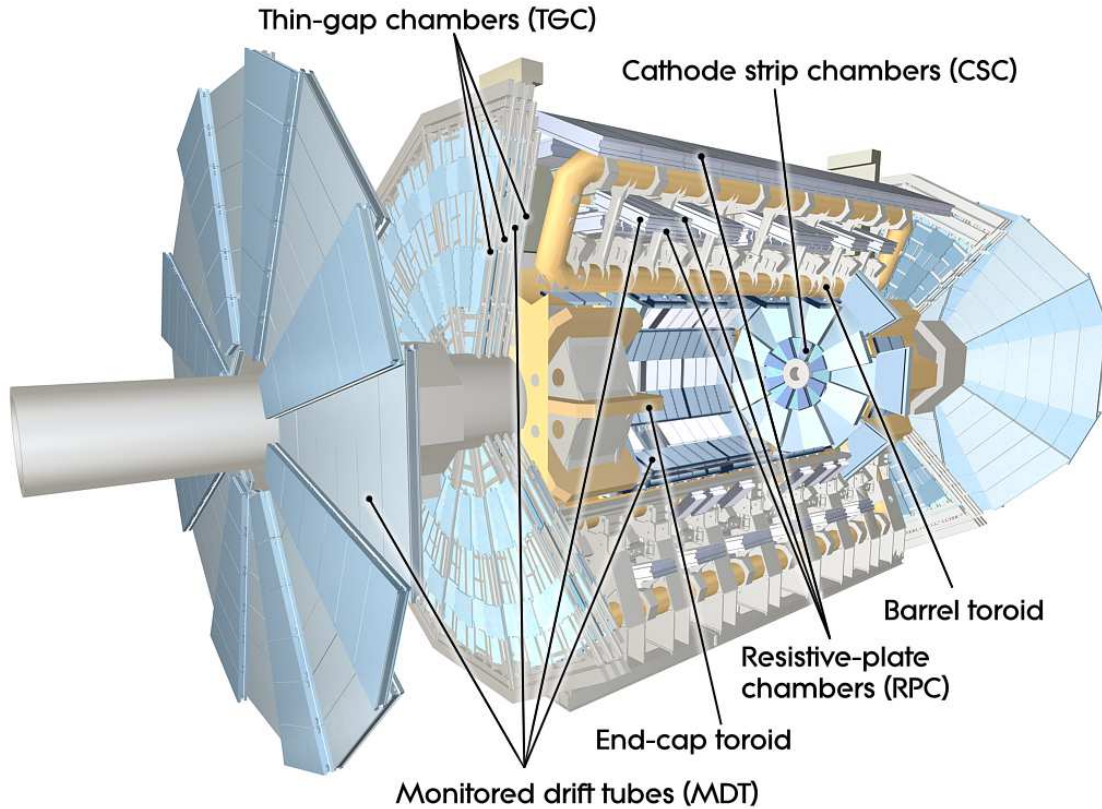


Figure 3.10: Schematic view of the muon spectrometer system of the ATLAS detector [3]. It is the outermost part constructed around the calorimeter system, including a big toroid magnet system, which is highlighted as the yellow parts. The bent muon trajectories are measured with three layers of four different tube or chamber detector types.

They provide bunch-crossing identification, p_T measurement for the triggers and the muon coordinate perpendicular to the one provided by the MDT and CSC instruments. More details of the individual chambers can be found in Reference [3].

3.2.5 Luminosity Measurement

The measurement of the luminosity delivered to the ATLAS experiment is an important key issue for any physics analysis. It is directly related to the precision of cross section measurements and important for background modeling and the sensitivity in searches for new physics. Two main challenges are dealt with: the measurement of relative luminosity changes down to short time scales on the one hand and the calibration to absolute luminosities on the other hand. This is done with special dedicated detectors, LUCID and BCM, on bunch-by-bunch basis, and also LAr calorimeters in the forward region are used for longer time scales.

LUCID is a Cherenkov integrating detector using with C_4F_{10} gas filled aluminum tubes and is located at both sides of the detector 17 m away from the interaction point. It measures inelastic $p-p$ scattering for online relative luminosity monitoring. Charged particles produce

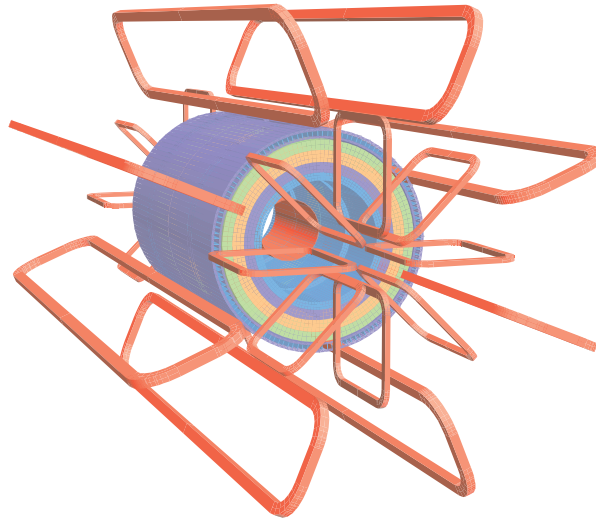


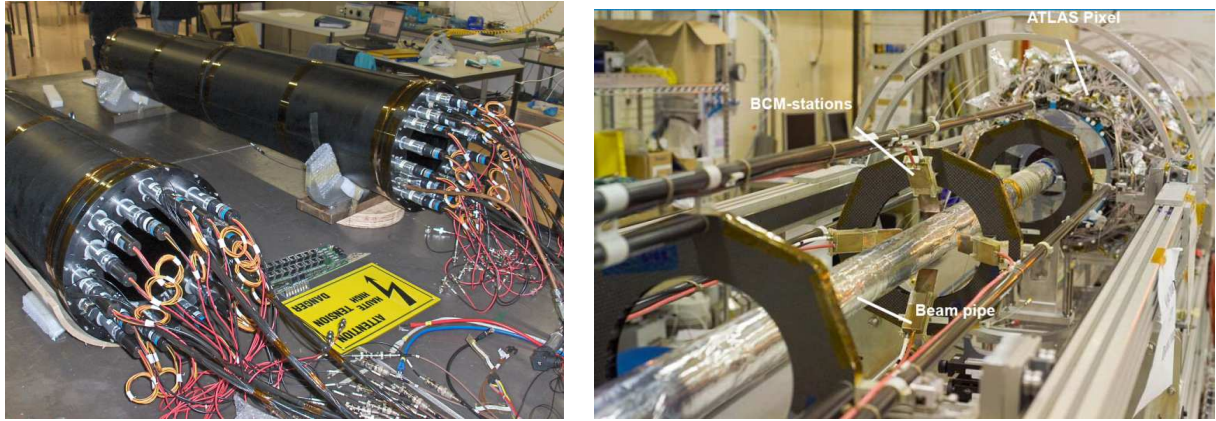
Figure 3.11: Scheme of the magnet system of the ATLAS muon spectrometer [3]. It consists of a barrel toroid with eight air coils and two smaller end-cap toroids. Also shown is the central solenoid inside the calorimeter to provide the field for the inner detector and the tile calorimeter modelled by four layers of magnetic properties.

Cherenkov photons in the gas which are reflected at the inner side of the tubes until they are detected by photomultipliers (PMTs) at the back of the tubes. The signal readout is connected to the LHC clock and therefore events can be measured for each bunch crossing individually in the range of $5.6 < |\eta| < 6.0$.

BCM is the Beam Conditions Monitor which includes four diamond sensors on each side of the ATLAS interaction point at $|\eta| = 4.2$. These sensors are very radiation hard and are mainly designed to measure the beam loss level and trigger a beam dump request, if the ATLAS inner detector could be damaged. The BCM also provides a fast relative luminosity measurement for individual bunch crossings. The LUCID and BCM detectors before their installation are shown in Figure 3.12.

Further, the high voltage return currents of the EMEC and the FCal calorimeters from both end-cap sites and also the TileCal PMT currents are used for high precision determination of relative luminosity changes. These currents are proportional to the number of charged particles passing through the calorimeters and therefore proportional to the number of minimum-bias events and to the luminosity as shown in [54]. The calorimeter measurements are also used for determining the long-term stability of the various luminosity monitors and the dependence on pileup [55]. The LAr calorimeter currents are read out on timescales of a few seconds and the precision and agreement of the various devices is at 2% or less.

The absolute calibration of the luminosity monitors is done with van der Meer (vdM) scans [56] in special dedicated runs where the absolute luminosity is obtained from machine parameters. The input luminosity delivered by the LHC can be calculated as



(a) The LUCID tubes before their installation. (b) The BCM in front of the ATLAS pixel detector around the beam pipe.

Figure 3.12: Photographs of the LUCID (left) and the BCM (right) before installation. The LUCID modules are located in 17 m distance at both sites of the interaction point while the BCM sensors are at 1.84 m from the interaction point [3].

$$\mathcal{L} = \frac{f_b n_1 n_2}{2\pi \Sigma_x \Sigma_y} \quad (3.4)$$

with f_b being the LHC bunch-crossing frequency, n_1 and n_2 the protons per bunch in the two colliding beams and Σ_x and Σ_y the horizontal and vertical profiles of the beams. During a vdM scan, the beams are separated by a known distance in steps allowing a direct measurement of the profiles Σ_x and Σ_y . The bunch charge product, $n_1 n_2$, can be measured externally, and therefore the absolute luminosity for unseparated beams can be obtained. The calibration is done with an uncertainty of 3.7% for the 2011 data taking. The main contribution is with 3.0% due to the uncertainty on the measured bunch charge product ($n_1 n_2$) [56].

3.2.6 The Trigger System

The bunch-crossing rate is at 40 MHz with the design 25 ns bunch spacing and 20 MHz with the 50 ns bunch spacing as it is used in the 2011 and 2012 data taking periods. With an average final event size of about 1.3 Mbyte this is by far too much data to write out permanently. Therefore, a multilevel trigger system is used to select interesting events using fast trigger algorithms. The first step is the level 1 (L1) trigger which looks for typical signatures of electrons, muons, photons, jets, and tau candidates with high p_T and large missing and summed transverse energy. It selects events using only limited detector information from the calorimeters and the muon detectors for further use within $2.5 \mu\text{s}$ to reduce the rate down to 75 kHz [3]. A scheme of the L1 trigger working principle is shown in Figure 3.13.

The level 2 (L2) trigger step uses more detector information to further select the events. This is based on regions of interest (ROI), which are η and ϕ regions of interesting detector activity defined by the L1 trigger. In these ROIs the L2 uses the full detector information with the full granularity and precision. The average event processing time is of around 40 ms and the trigger rate is reduced to 3.5 kHz after the L2. Finally, the event filter (EF)

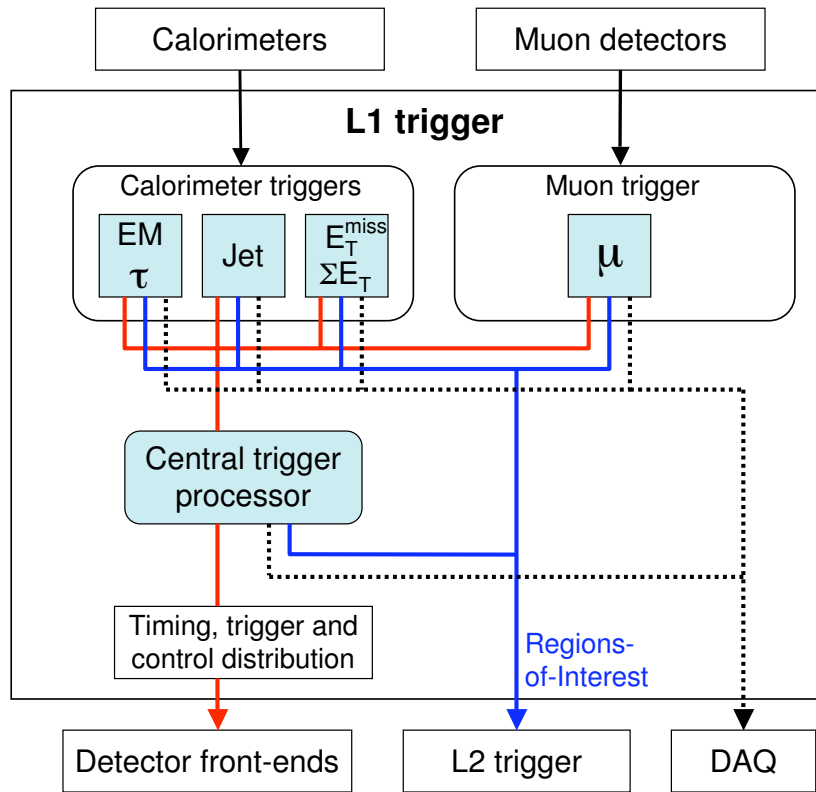


Figure 3.13: Scheme of the L1 trigger. The calorimeters and muon detectors send their data to the central trigger processor (CTP) where the L1 decision is computed and sent to the detector front-end boards, the L2 trigger system and to the DAQ [3].

step reduces the rate to 200 Hz, which is then the final data recording rate. It processes the events by offline algorithms within 4 s per event on average. The event filter is also the trigger which needs to be chosen for a physics analysis as it is the last one in the chain and the first step of the event selection. The complete trigger menu available for the 2011 data taking run is described in detail in [57].

3.2.7 Data Taking

ATLAS started to take data of p - p collisions in March 2010. Until July 2011, about 1.6 fb^{-1} of data have been recorded with a center of mass energy of 7 TeV. This is the dataset used for the $Z \rightarrow \tau\tau$ cross section measurement described in Chapter 5. Overall around 5 fb^{-1} were recorded at $\sqrt{s} = 7 \text{ TeV}$ until October 2011. The LHC data taking continued in 2012 with $\sqrt{s} = 8 \text{ TeV}$ and about 18 fb^{-1} have been recorded at that center of mass energy until the time of writing.

The data taking is divided in periods labelled from A to M (except for C) for the 7 TeV data. A further subdivision are the runs which usually correspond to one LHC fill. One run, finally, contains many luminosity blocks of a few minutes length. A summary of the data taking periods is given in Table 3.2 together with the corresponding range of runs and the

integrated luminosity recorded. Relevant data taking configurations, like the trigger menu, are constant within one run but can change from period to period or also within one period.

Table 3.2: Summary of data taking periods for the 7 TeV LHC run.

Period	Runs	Luminosity recorded by ATLAS [pb^{-1}].
A	177531 - 177965	8.3
B	177986 - 178109	17.0
D	179710 - 180481	178.8
E	180614 - 180776	50.2
F	182013 - 182519	152.2
G	182726 - 183462	560.8
H	183544 - 184169	278.3
I	185353 - 186493	399.2
J	186516 - 186755	232.9
K	186873 - 187815	660.2
L	188902 - 190343	1568.8
M	190503 - 191933	1121.8

4 Testbeam Study of Liquid-Argon Calorimeter Performance at High Rates

4.1 Upgrade Plans of the LHC and the ATLAS Calorimeters

The Large Hadron Collider (LHC) started operation in 2009 and delivered about 5 fb^{-1} collision data to both multi-purpose experiments, ATLAS and CMS, at a center of mass energy of 7 TeV until the end of 2011. A data collection of around 25 fb^{-1} at 8 TeV is expected until the end of 2012. This will allow a measurement of the properties of newly discovered particles with a higher precision and to extend the mass range for new physics searches. For a rich physics program, an increase of the instantaneous luminosity of the LHC is planned in multiple steps of upgrades. Furthermore, a factor of 2 in average luminosity will be gained by luminosity leveling. Therefore several phases of shutdowns are foreseen, where machine upgrades as well as upgrades of the LHC detectors will take place.

The highest instantaneous luminosity achieved at the time of writing is around $6 \times 10^{33} \text{ cm}^{-2}\text{s}^{-1}$. A first shutdown with technical improvements will take place in 2013 and 2014 with the main goal to reach a center of mass energy between 13 TeV and 14 TeV. An instantaneous luminosity of $1\text{-}2 \times 10^{34} \text{ cm}^{-2}\text{s}^{-1}$ is planned to be reached after this Phase0 shutdown. Data taking will then continue until 2018, when a second shutdown is foreseen to upgrade for the Phase1 running. In this shutdown, improvements are foreseen which allow a luminosity of about $3 \times 10^{34} \text{ cm}^{-2}\text{s}^{-1}$. Finally, a third upgrade phase (PhaseII) will follow in 2022 to make the LHC and the experiments suitable to run at $5\text{-}7 \times 10^{34} \text{ cm}^{-2}\text{s}^{-1}$ instantaneous luminosity. This long term schedule [58] is very preliminary and may change in time. In any case, it is important to study which detector components need upgrades or replacements for the different upgrade steps and to develop detailed technical designs to satisfy the high luminosity running requirements.

A main challenge is the high particle flux through the detector components with an increased luminosity, especially in the forward and endcap regions of the detector. With an inelastic p-p cross section of $\sigma_{inel} = 80 \text{ mb}$ and a design luminosity of $10^{34} \text{ cm}^{-2}\text{s}^{-1}$, the event rate would be at 8×10^8 inelastic events per second. A resulting particle flux between $5\text{-}16 \times 10^{12} \text{ F}_{neq}/\text{year}$ for the FCal and $0.5\text{-}5 \times 10^{12} \text{ F}_{neq}/\text{year}$ for the EMEC has been calculated from simulations [3]. F_{neq} is the 1 MeV neutron equivalent fluence, while the particle flux consists mainly of photons, pions, neutrons, electrons, protons and muons.

As the inelastic event rate and with it the particle flux are in first order proportional to the luminosity, these estimated fluxes through the calorimeters are expected to also increase with a factor of up to 7 (Phase II), accordingly to the luminosity.

Regarding the ATLAS calorimeters, the endcap calorimeters HEC, EMEC, and FCal are exposed to the highest particle fluxes and thus are affected most by increased luminosities. Especially the FCal1 module, due to its position near to the beam pipe, will get close to its operation limit because of positive ion build-up and large currents drawn. Simulations have already shown that at the luminosities expected after the Phase II upgrade, a significant part of the FCal1 below $|\eta| < 3.8$ will show marginal performance and even unstable degraded operation [58]. Two possible scenarios are considered at the time of writing: the installation of an additional mini-FCal in front of the present FCal module and the replacement of the FCal1 with a new one (HL-FCal1) which would use smaller LAr gaps of only 100 μm instead the 250 μm ones.

A testbeam study is set up to test the operation of small test modules of the HEC, the EMEC, the FCal1 and a prototype of the HL-FCal1 in high intensity environments. The aim is to prove that these modules operate well in the high luminosity (HL) LHC phase. This testbeam study and its results are the topic of this chapter, where especially the measurement and analysis of the HV return currents are part of this work.

4.2 Testbeam Parameters and Setup

The Hilum testbeam project has started in 2006 with the goal to simulate the particle fluxes through calorimeter test modules similar to the LHC environment up to very high instantaneous luminosities. It is installed at beamline 23 of the U-70 proton synchrotron at IHEP in Protvino, Russia [59] to send the primary proton beam through the calorimeters. The U-70 operates since 1967 and reaches a maximum beam energy of 76 GeV. The synchrotron ring uses up to 30 RF proton bunches. With a circumference of 1.48 km, the bunch spacing between each single RF bunch is around 165 ns. The RF bunch structure of the synchrotron is kept during the extraction of the beam so that the calorimeter response to one bunch corresponds to that of one particle pulse in ATLAS.

The beam energy used for the testbeam study is 50 GeV and only every sixth RF bunch out of the 30 bunches is filled with protons. This leads to a bunch spacing of roughly 990 ns, which is enough to measure well separated bunches preventing overlaps from following calorimeter signals. A scheme of the accelerator operation is shown in Figure 4.1. One accelerator fill is extracted over around 1.2 s which is defined as one spill and the spill cycle time is about 9.5 s.

The extraction is done by using a bent crystal extraction technique [60] which allows to scrape only a part of the proton bunch from the circulation orbit into the extraction orbit. The extracted beam intensity ranges approximately from 10^6 p/spill to 3×10^{11} p/spill. The experimental setup in beamline 23 includes the beam instrumentation, absorbers and three cryostats housing the calorimeter test modules. A schematic overview of the experimental setup can be seen in Figure 4.2.

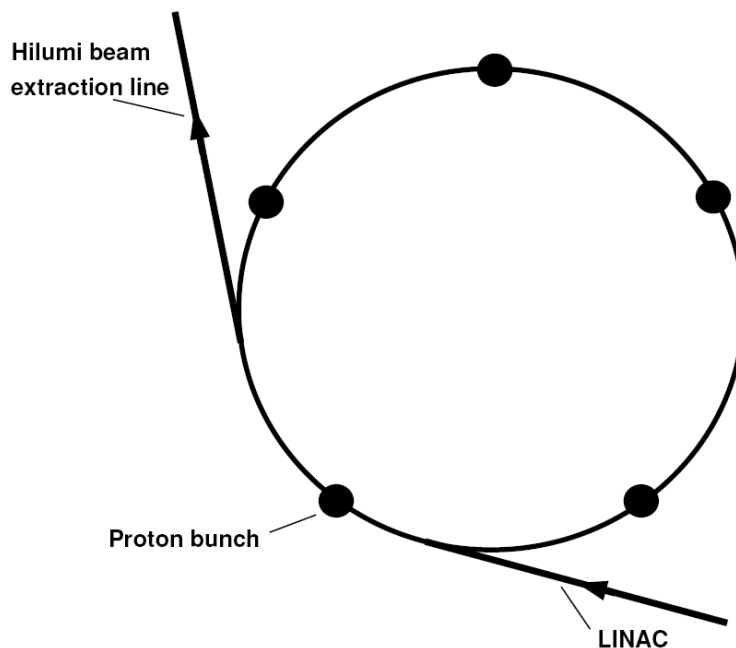


Figure 4.1: The figure shows the working scheme of the U-70 proton accelerator for the Hilum testbeam project. Five out of 30 RF bunches are filled and extracted over about 1.2 s via a bent crystal extraction technique.

Beam instrumentation and intensity measurement is one priority in the testbeam setup, as it is the reference quantity to compare the measured calorimeter pulses and HV currents with. A secondary emission chamber measures the beam intensity and profile in the two dimensions orthogonal to the beam axis. Six scintillation counters are installed for beam intensity measurement, three within the beam line (S1, S2, S3) for low intensities less than 10^7 p/spill and three at around 45° with respect to the first absorber for intensities up to 10^{10} p/spill. The latter ones are working in coincidence and are hence called scintillation counter monitor (SM). Further, an air Cherenkov monitor provides bunch-based beam intensity monitoring with a timing resolution of several ns. A scintillation counter hodoscope is used for additional beam profile and beam position measurement also at low intensities. It uses 16 scintillation strips in the horizontal and in the vertical orientation perpendicular to the beam axis. Finally, a DC ionization chamber measured the beam intensity of the spills over a wide beam intensity.

After the beam instrumentation, a first absorber with a hadronic interaction length of 0.7λ is installed, followed by the cryostat with the FCal test module. A second absorber of 1.8λ in front of the cryostats including the EMEC and HEC modules reduces the flux through them even more. This setup is optimized to achieve particle fluxes through the different calorimeter modules corresponding to the relative fluxes in ATLAS. They vary with the position in η and the material in front of each calorimeter.

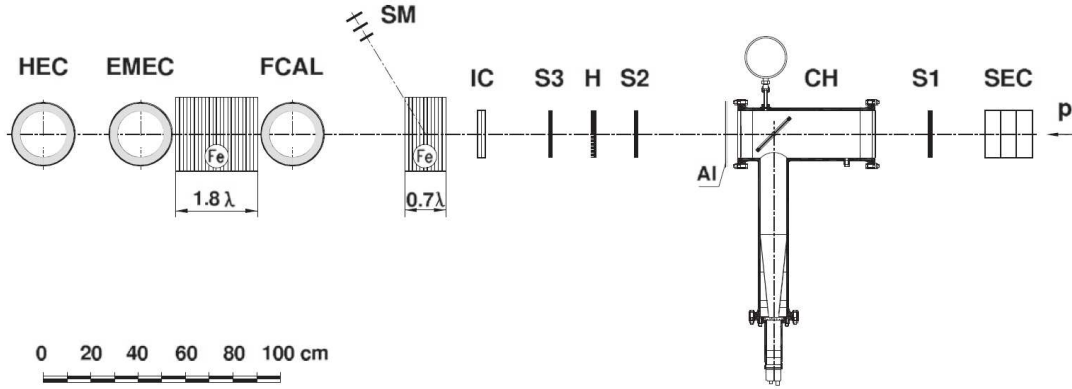


Figure 4.2: Layout of the experimental setup in beamline 23 of the U-70 accelerator [61]. The beam direction is from right to left.

4.3 The Calorimeter Test Modules

The test modules are installed in individual cryostats which are filled with argon of high purity of < 1 ppm oxygen equivalent contamination. They are cooled with liquid nitrogen to keep the argon liquid at a constant level in the cryostats. An increased pressure of about 1.5 bar is applied to prevent inflow of the outside air. In the first cryostat the FCal test module is housed. It consists of two parts: one with $250 \mu\text{m}$ LAr gaps similar to the FCal1 in ATLAS and one with $100 \mu\text{m}$ LAr gaps to test also the proposed upgrade module. Both parts include 16 tubes each, which are grouped together to four readout and four high voltage (HV) channels. A nitrogen cooling loop provides additional cooling directly at the module to prevent strong heating during high beam intensities. The cryostats can be moved horizontally to the beam so that both FCal parts can be centered to the beam separately. A schematic view of the FCal module layout together with a photograph can be seen in Figure 4.3.

The EMEC test module is housed in the middle cryostat and is designed accordingly to the EMEC calorimeter in ATLAS. It consists of four 2 mm lead absorber plates, covered with stainless steel, and three pairs of copper electrodes in between the absorbers. The 2 mm gaps between the absorbers and the electrodes are filled with liquid argon to form the active medium. This is illustrated in Figure 4.4 on the right. The electrodes are divided in four quadrants. Thus, the EMEC test module includes four signal readout channels and three HV channels. The HEC test module is also constructed to represent a small fraction of the actual ATLAS HEC calorimeter and consists of four readout and four HV channels. The size of this module in direction to the beam is about 50 cm^2 . The layout is illustrated on the left picture of Figure 4.4.

4.4 Test Module Readout and Signal Degradation

Charged particles passing the LAr gaps of the calorimeter modules ionize the argon and the electrons and ions begin to drift in the electrical field immediately. As the electrons drift orders of magnitude faster than the ions [62], they are the main source of the signal

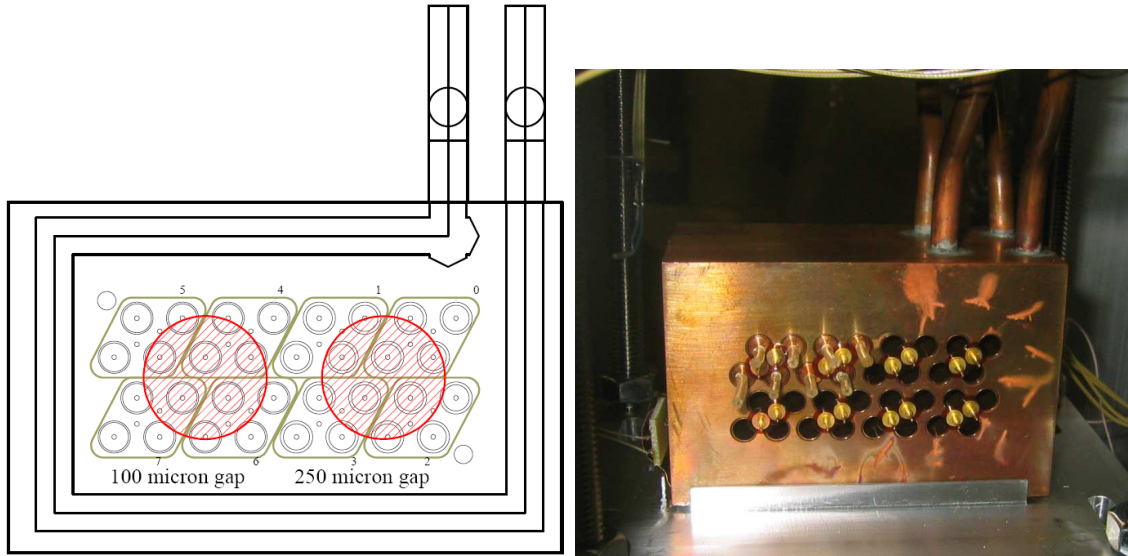


Figure 4.3: Left: layout of the FCal test module with the two parts visible the approximate beam size indicated. Right: photograph of the FCal module with some rods taken out. Visible is also the liquid nitrogen cooling loop.

production. This is caused by a current induced by the drifting electrons, which has its maximum shortly after ionization. With time more and more electrons reach the electrode and the number of drifting charges and thus the induced current decreases linearly. This leads to a typical triangular signal form at the electrodes which is then shaped to a bipolar pulse by the readout electronics. The pulse is then digitized by sampling ADCs, each 25 ns. This is illustrated on the left plot of Figure 4.5 showing theoretical curves for the triangular signal overlaid with the shaped pulse. For the testbeam studies, two ADCs are used with an offset to reach an effective sampling rate of 12.5 ns. In addition, two gains are available: low and medium. The readout chain is modelled with high accuracy, which is illustrated in the right plot of Figure 4.5, where the response of one channel of the HEC test module to a calibration pulse overlaid with the corresponding model function is shown. The observed deviations are below 3%.

One main goal is to study the calorimeter behaviour and signal degradation with increased beam intensities. At high ionization rates positive ions build up in the LAr gaps due to their slow drift velocity. These charge carriers accumulate in the gap and reduce the electric field by shielding. A critical situation is reached, when the accumulated charge in the gap becomes equal to the applied charge at the electrode by the HV. Then, the electric field over the gap can partly drop to zero. This defines the critical ionization rate, D_C , and would reduce or even stop the drift of the electrons leading to a reduction of the induced signal. A detailed description of the processes can be found in [62], while here just an overview of the most important aspects is given.

The relative ionization rate, r , is defined as the absolute ionization rate, D , divided by the critical ionization rate, D_C :

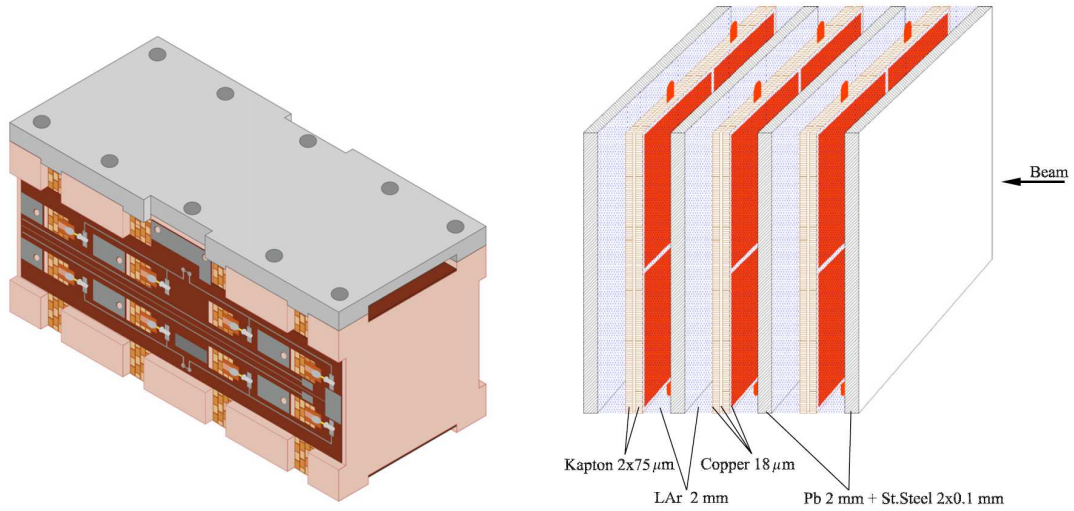


Figure 4.4: Shown are layouts of the HEC test module on the left and of the EMEC test module on the right.

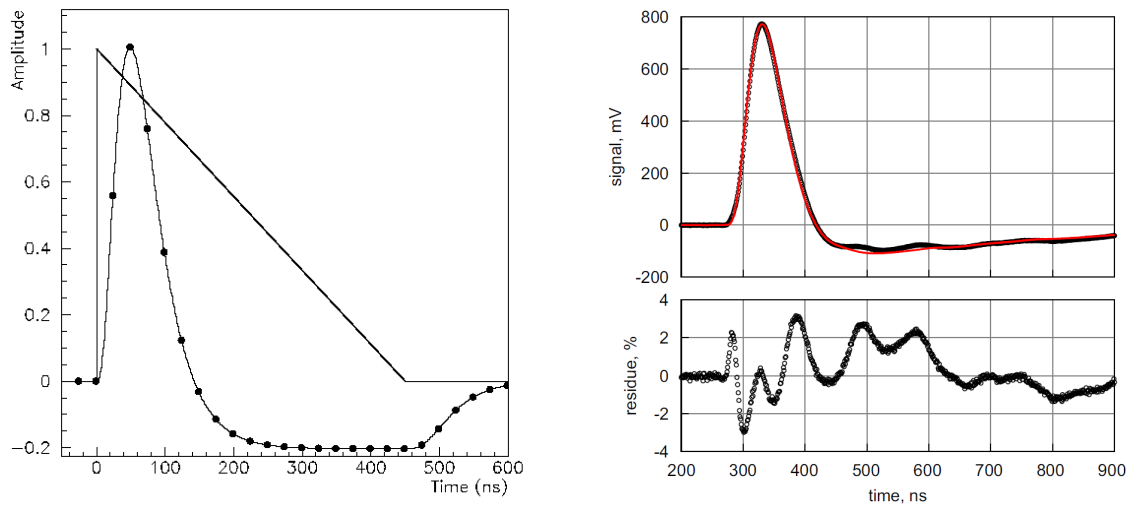


Figure 4.5: Left figure: theoretical prediction of the triangular and the shaped signal for a 2 mm LAr gap of the EMEC. Right figure: response of one channel of the HEC test module to a calibration pulse, compared to a model function.

$$r = \frac{D}{D_C}. \quad (4.1)$$

Apart from the ionization rate, the signal degradation also depends on the recombination rate, w . To study the signal degradation in the testbeam and investigate the beam intensity at which the ionization rate becomes critical, the signal amplitude normalized to the bunch intensity is of interest. The theoretical calculations [62] predict a flat dependence of the normalized signal amplitude, s , on the relative ionization rate below the critical intensity and a reduction proportional to:

$$s \propto \frac{1}{r^{1/4}} \quad (4.2)$$

above the critical intensity for the limit $w \rightarrow 0$. The exact behaviour depends on w and simulations for different recombination rates together with analytic curves as calculated in [62] can be seen in Figure 4.6. Simulations with $w = 0$ and ideal conditions (LAr pollution, electron velocity distribution) can be described exactly by the theoretical calculations, while those with higher recombination rates and more realistic conditions differ more from the calculations [62]. The observation of that breakpoint can be used to determine the critical intensity for each calorimeter module.

Also the high voltage (HV) return currents, which compensate the charge flow over the gap, can be used to determine the critical intensity and the critical current. The measurement and analysis of these currents is the main topic of this chapter and is described in detail in the following sections.

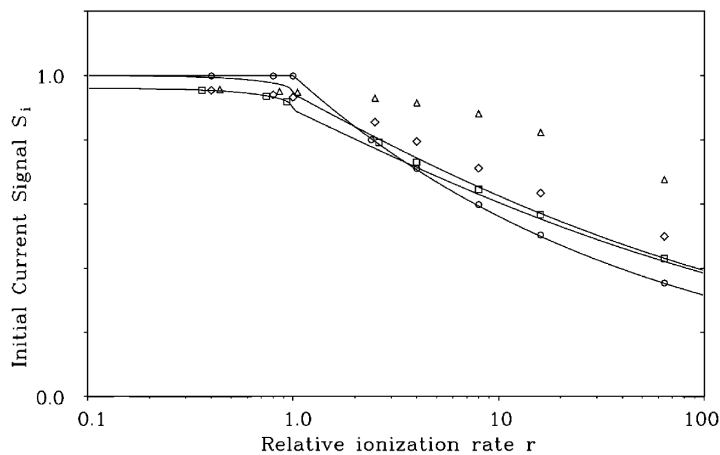


Figure 4.6: Normalized signal amplitude as a function of the relative ionization rate. The curves represent analytic calculations and the data points are simulations for different recombination rates between 0 (circles) and highest value of more than 5000 (triangles) [62].

4.5 Measurement and Analysis of the HV Currents

A testbeam study on the relative luminosity measurement of the LHC with the HV return currents of the ATLAS forward calorimeters has been presented in [54]. Here, the HV

currents of the EMEC test module are analysed to extract the critical current and critical intensity in the HiLum testbeam project.

4.5.1 Device for Precision HV Current Measurement

The three HV channels of the EMEC are powered by an ISEG [63] HV power supply. The maximum voltage is 2500 V and the maximum current drawn is 10 mA. For a high precision measurement and logging of the currents, an external device is installed between the HV power supply and the calorimeter test module. It uses the voltage drop over a 125 Ω resistor which is then digitized with a 24 bit ADC. That way, a digital resolution of 1.2 nA/bit is achieved, leading to an effective resolution of about 20 nA due to electronics noise. A photograph of the device can be seen in Figure 4.7. The measuring rate is 10 Hz per channel and a timestamp of 10 ms precision is added to each measurement by a microcontroller. All data is sent to a data acquisition computer for an online monitor as well as permanent storage.

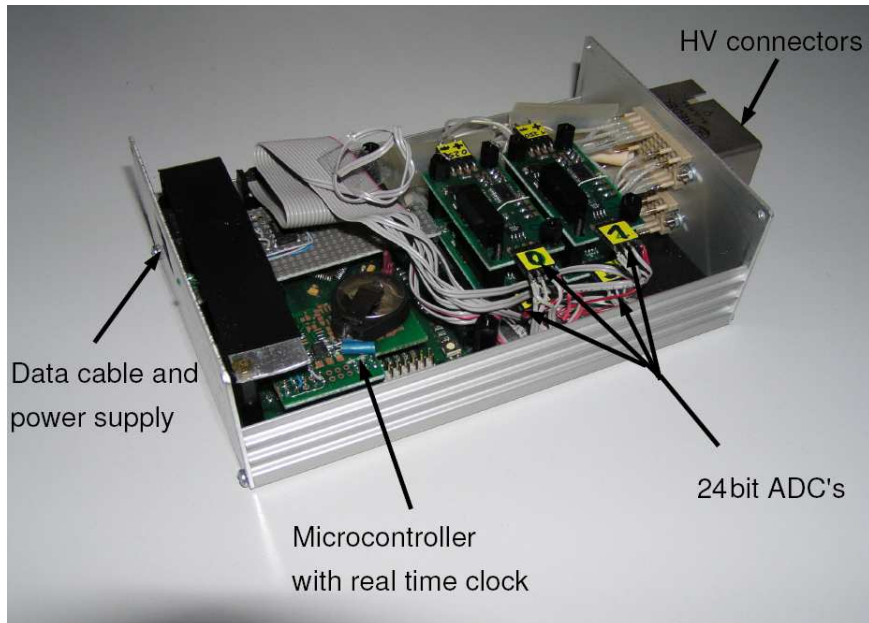


Figure 4.7: HV current measurement device used for precision measurements of the HV return currents of the LAr calorimeter test modules during the HiLum testbeams in Protvino, Russia.

4.5.2 Testbeam Data Taking

Here, a summary of the testbeam data taking and all runs relevant for the study of the EMEC module currents is given. A main aim of the testbeam project is the study of the calorimeter readout signals in dependence of the beam intensity and also on the HV applied at the LAr gaps. Therefore, several runs at multiple HV steps have been performed for each beam intensity period delivered by the accelerator. The runs took usually about 10 min with several minutes interruption between them to adjust the new voltage to the

calorimeter modules. Quality criteria for run periods which can be used for a study of the HV currents in dependence of the beam intensity are:

- good overall operation and data quality
- constant beam position
- constant HV applied to the calorimeter test module
- reasonably long time interval for sufficient statistics.

The runs satisfying these requirements which are used for the study are summarized in Table 4.1. Due to the risk of a HV breakthrough in the EMEC test module, the HV has been limited to 1.2 kV during the testbeam run in 2010. Multiple HV steps are chosen to scan the behaviour at different voltages. The selected runs include two different voltages applied: 1.0 kV and 1.2 kV.

Table 4.1: Summary of testbeam runs used for analysis of the EMEC HV currents. The duration includes the time between spills and also possible time without beam and thus does not correspond to the effective beam time.

Run number period	Duration [h:min]	HV applied to EMEC	Beam intensity [p/s]
712-715	1:12	1.2 kV	$6 \times 10^7 - 4 \times 10^8$
718-727	8:27	1.0 kV	$7 \times 10^7 - 2 \times 10^9$
737-747	4:28	1.0 kV	$2 \times 10^8 - 7 \times 10^{10}$
745-763	7:19	1.2 kV	$6 \times 10^7 - 3 \times 10^8$
797-827	11:06	1.0 kV	$3 \times 10^7 - 2 \times 10^{10}$

The beam intensity is measured by different devices as described in Section 4.2. The Cherenkov monitor turned out to be the device with the most linear and reliable behaviour over the whole intensity range and hence it is used to compare the HV currents with the beam intensity. Therefore, good operation conditions of the Cherenkov monitor are also a criteria for the data period selection.

4.5.3 Analysis of the EMEC Currents

The timestamp attached to each HV current measurement is not synchronized with the DAQ timestamp and the bunch trigger. Therefore, measurements within a spill (signal) need to be separated from those between the spills when no beam is present (background). This is done by obtaining the distribution for background-only for the three channels from data without beam. Those are dominated by electronics noise and assumed to be Gaussian distributed. Hence, a gaussian fit is applied and a threshold of 5σ is applied to define signal measurements to be above the threshold. The thresholds obtained for the three channels are summarized in Table 4.2.

If several measurements within 0.6s are above the threshold, without a background measurement in between, they are identified as a spill. The analysis of the HV currents as a

Table 4.2: Thresholds to separate signal measurements from background only ones in nA. They are obtained from Gaussian fits of the background distributions and by taking the 5σ deviation from the mean value of the background.

HV channel	Threshold [nA]
0	556
1	454
2	427

function of the beam intensity is done on a spill-by-spill basis. To each spill signal identified in the HV current data, a corresponding measurement from the Cherenkov data is assigned, if the timestamps do match within ± 3 s. This can compensate for possible asynchronous running of the clocks and also prevents assigning the wrong spills in both data sets, as the distance between two subsequent spills is about 9.5 s. The integrated currents over each spill are calculated to compare them with the beam intensities also integrated over the spills. The integral, I , is calculated as:

$$I = \sum_{i=1}^n (s_i - B) \cdot d, \quad (4.3)$$

with s_i being one measurement within the spill, n the number of such signal measurements, d the time between two measurements and B the mean of the background before the corresponding spill. The time interval, d , is usually 0.1 s and B is calculated as a usual mean value from m background measurements b_j :

$$B = \frac{1}{m} \sum_{j=1}^m b_j. \quad (4.4)$$

To calculate the uncertainty on the integrated currents, the electronics noise as the main source of uncertainty is obtained from the background measurements. First, the uncertainty on the subtracted pedestal B is given by

$$\Delta B = \frac{1}{\sqrt{m \cdot (m-1)}} \sqrt{\sum_{i=1}^m (B - b_i)^2}, \quad (4.5)$$

and the uncertainty on a single measurement is also caused by electronics noise and obtained from the fluctuation in the background as

$$\Delta s_i = \sqrt{m} \cdot \Delta B. \quad (4.6)$$

Finally, the uncertainty on the integral over the spill includes the uncertainties on B and s_i and is calculated by:

$$\Delta I = \sqrt{[(n \cdot d \cdot \Delta B)^2 + n \cdot (d \cdot \Delta s_i)^2]} = n \cdot d \cdot \Delta B \cdot \sqrt{1 + \frac{m}{n}}, \quad (4.7)$$

in which the uncertainty on the time interval d is negligible. This procedure is also described in Reference [54]. The HV channels of the EMEC are arranged longitudinally to

the beam, with each channel covering the full transverse plane (compare right picture of Figure 4.4). Therefore, no significant differences between the HV currents in the different channels depending on the beam position are expected.

4.5.4 Beam Intensity Measurement

The beam intensity in the testbeam runs is monitored by several devices to provide measurements on timescales with spill resolution as well as with bunch resolution. The scintillation counters S1-S3 and the scintillation counter monitor (compare Figure 4.2) sample the beam intensity in time slices of 4.096 ms and record the data of the whole spill. Thus, given a bunch spacing of 1 μ s, one time slice sums over about 4000 bunches and fluctuations below that cannot be resolved. The counters S1-S3 can be used for the lowest intensities up to 10^7 p/spill and the SM for higher intensities up to 10^{10} p/spill. The ionization chamber measures the intensity integrated over the spill also up to medium intensities of $\approx 7 \times 10^7$ p/spill.

For the highest intensities in the range 7×10^{10} - 10^{12} p/spill the secondary emission chamber provides beam profile as well as beam intensity monitoring. It uses three electrodes arranged longitudinally to the beam and separated by 3 mm. Each electrode consists of 16 aluminium coated polyimide strips of 18 cm length and 1 cm width in the horizontal and in the vertical plane, respectively. The high voltage is applied to the middle electrode. The absolute calibration is done with activated aluminium foils which stay directly in the beam for a longer period. Their activation due to the beam is measured with the reaction $^{27}\text{Al}(p,3p3n)^{22}\text{Na}+\gamma(1275\text{ keV})$ and their known cross section of $\sigma = 10.6 \pm 1.1$ mb. The precision of this calibration method is about 15 % [61].

Most important for the analysis described here is the Cherenkov monitor, which can be used over a very wide intensity range and also is able to resolve single bunches. Therefore, it is able to monitor intensity fluctuations within the spill. It is filled with air and coupled to a XP2020 photo multiplier. It is read out with two different data streams. The first one is an integrating ADC with a gate width of 100 ns and synchronized to the accelerator RF at 6 MHz which records all bunches of the spill. And secondly a sampling ADC with a sampling frequency of 200 MHz is used which is read out every 5 ns also for the full length of the spill. It can be adapted to the operation conditions by adjusting the high voltage and also the pressure. It is calibrated at low intensities for different HV and pressure settings by using a green and a blue LED [61].

The beam intensity measurements of the Cherenkov monitor relative to the ionization chamber and secondary emission chamber are shown in Figure 4.8 for different calibrations of the various HV settings. A good linearity between the individual devices is observed in the relevant intensity range. The curve for the absolute calibration of the Cherenkov counter with the activated aluminium foils is shown in the left plot of Figure 4.9. The measurements of a typical spill are shown on the right plot of Figure 4.9 for two different time scales. The beam intensity variations in the 10 ms range are clearly visible as well as the resolution of single bunches with a distance of ≈ 1 μ s.

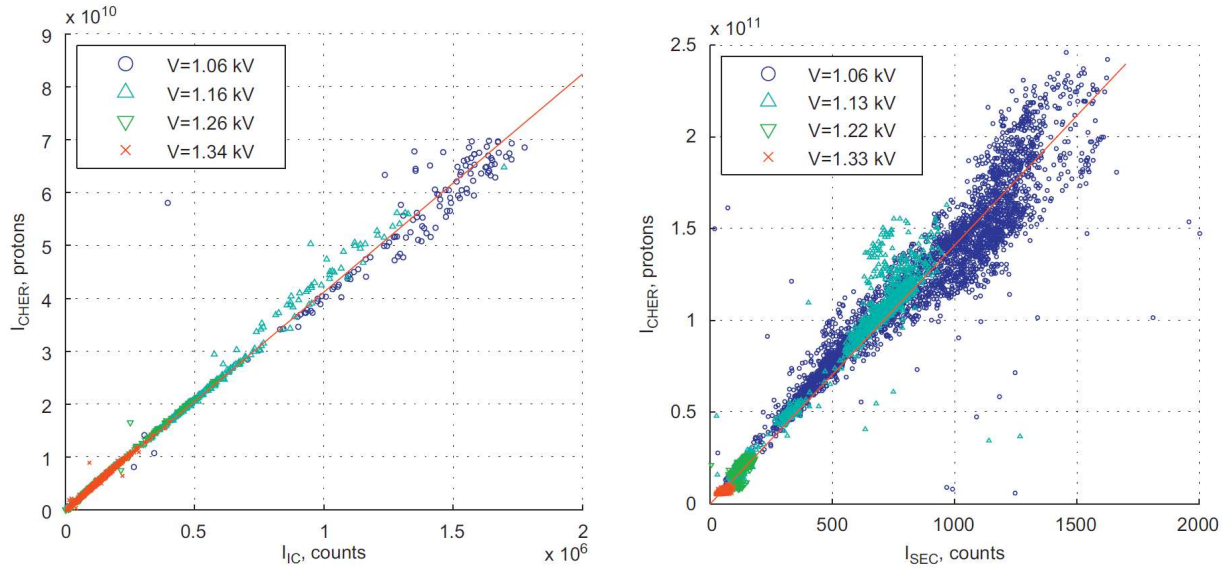


Figure 4.8: Left: Measured beam intensity of the Cherenkov monitor as a function of the ionization chamber measurements up to $7 \times 10^{10} p/s$. Right: Cherenkov counter measurements against the intensity as measured by the secondary emission chamber in the range up to $2.5 \times 10^{11} p/s$. The different symbols show different HV settings with calibration constants applied as obtained from the LED calibration [61].

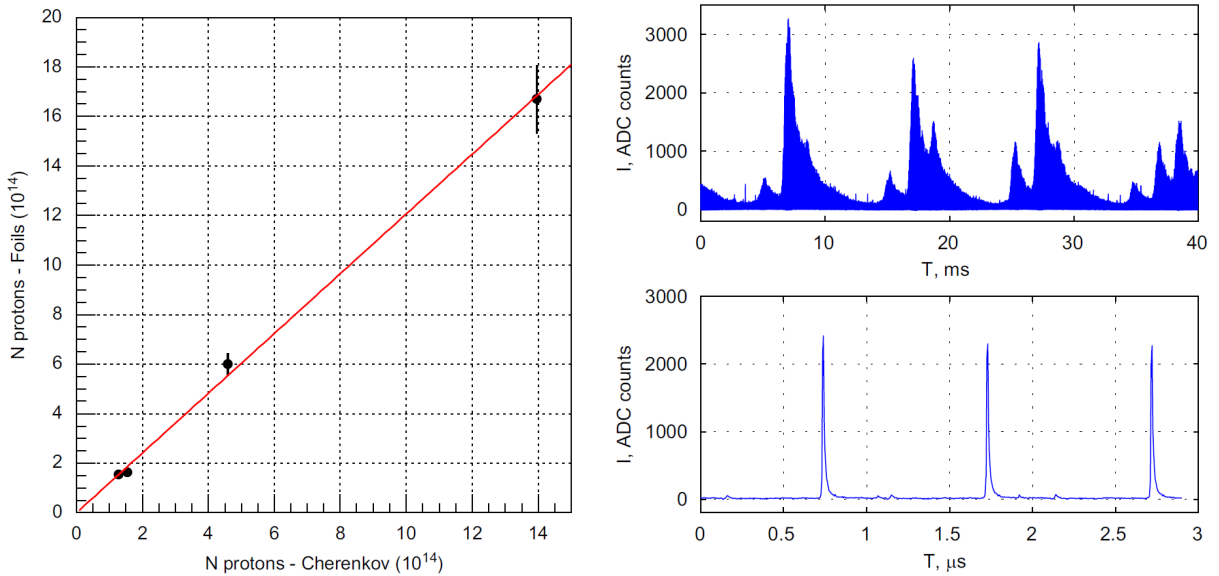


Figure 4.9: Left: Absolute calibration of the Cherenkov monitor with activated aluminium foils. Right: Cherenkov counter measurements for two different time scales. With the 40 ms range on the upper plot, the beam intensity variations within the spill are visible. The lower plot shows the individual bunches with data of a few μs [61].

4.5.5 Comparison of EMEC Currents to Beam Intensity

The EMEC test module is connected to the HV power supply and also to the HV current measuring device over a low pass filter with a time constant of 34 ms. That averages out the beam intensity fluctuations on this timescale. Global beam intensity variations during the spills do not affect the comparison when taking the integrated values over the spill. The Figures 4.10-4.14 show the resulting comparison between the HV currents on the vertical axis and the beam intensity as measured by the Cherenkov monitor on the horizontal axis for the five run periods summarized in Table 4.1. Each data point corresponds to the integrated values of one spill. The error bars correspond to the uncertainty calculated from Equation 4.7 for the HV data and the uncertainty on the beam intensity is estimated with 3.5%. The sets of four diagrams for each run period include from the top left to bottom right the three channels 0,1,2 and the summed HV current of the three channels. The sum is only calculated, if a spill can be identified in the HV data in all three channels as described in Section 4.5.3 and thus corresponds to the total current measured in the EMEC module.

The HV currents are expected to depend linearly on the beam intensity below the critical intensity. In this non-critical case, a higher density of charged particles flowing through the LAr gaps lead to a proportional higher production of ion-electron-pairs. They all drift to the electrode due to the HV applied and thus the HV current will also increase proportionally to the beam intensity. This behaviour is also confirmed in [54] and used for a relative luminosity monitoring of the LHC using the HV currents of the ATLAS FCal and EMEC.

Above the critical intensity, this linear behaviour is not valid anymore due to charge buildup and increased recombination effects as described in Section 4.4. To first order, a dependence of the HV current i on the beam intensity I of $i = I^{3/4}$ is predicted [62, 64].

The critical beam intensity, I_c , and the critical HV current, i_c (current drawn at the I_c), are unknown. However, there are estimates for those values, which are for the two different voltages applied during the analysed runs [64]:

$$1.0 \text{ kV} : I_c = 0.77 \cdot 10^8 \text{ p/s}, \quad i_c = 9 \mu\text{A} \quad (4.8)$$

$$1.2 \text{ kV} : I_c = 1.15 \cdot 10^8 \text{ p/s}, \quad i_c = 11 \mu\text{A}. \quad (4.9)$$

These are only first order predictions and need to be measured. Therefore, a fit function is used to describe the data in the intensity intervals:

$$i = \begin{cases} i_c \times \frac{I}{I_c}, & \text{for } I < I_c \\ i_c \times \left(\frac{I}{I_c}\right)^p, & \text{for } I > I_c, \end{cases} \quad (4.10)$$

with the critical intensity, I_c , the critical HV current, i_c , and the exponent, p , as free fit parameters. Those fit curves are included in the Figures 4.10-4.14 as a red line.

For each run period, individual fits are applied for each measured HV channel and the summed data. The obtained fit parameters are given in Table 4.3.

For a comparison of the fit parameters obtained for I_C , i_C and p with the predictions, the values from the summed channels are used as they include all EMEC module data. The critical values I_C and i_C need to be converted from protons/spill in protons/s and from $\mu\text{C}/\text{spill}$ in μA . Therefore, the values need to be divided by the spill length and thus the exact average spill length has to be evaluated. The 1.2s spill length mentioned previously is just a rough estimate and is extracted from the HV current data with higher precision. This is done by using each single signal measurement (within the spill) of the HV currents and dividing the integral over the corresponding spill by that measurement. The distributions of these values are created for each channel individually and filled with all data used in the five run periods.

As each spill is expected to have a plateau in the measured current in between the increasing and decreasing flank due to the low pass filtering and most values should, on average, lie within the plateau, a peak should be visible in the distribution described above. This peak would correspond to the average initial spill length before any filtering, as the integral over the spill stays unchanged by shaping it with the low pass filter and the integral divided by the plateau value does therefore still correspond to the initial spill length. Those distributions together with a gaussian fit of the peak are shown in Figure 4.15. The gaussian fits are used, as the fluctuations of the currents at the plateau are expected to be due to electronics noise which is also gaussian distributed. The mean values of the spill length obtained from the means of the gaussian fits are 1.191s (channel 0), 1.187s (channel 1) and 1.189s (channel 2). Hence, an average spill length of 1.19s is used, very close to the rougher estimate of 1.20s.

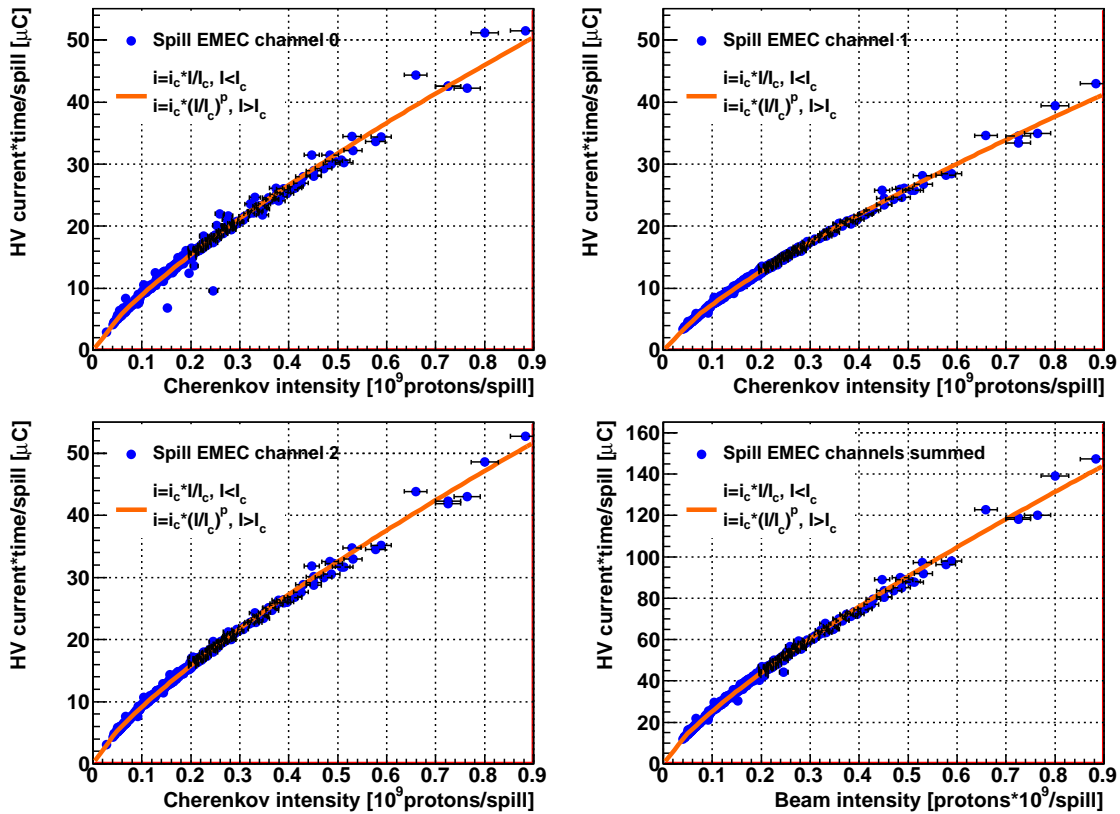


Figure 4.10: HV current in dependence of beam intensity for run period 712-715.

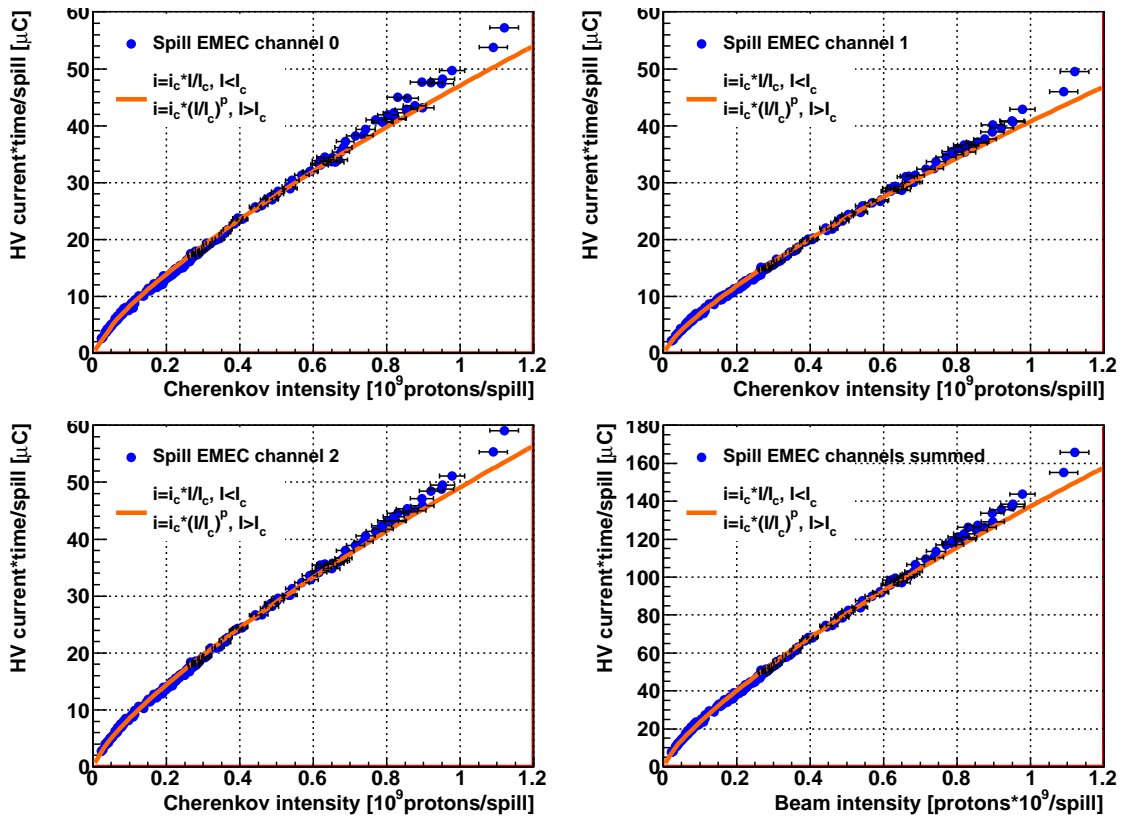


Figure 4.11: HV current in dependence of beam intensity for run period 718-727.

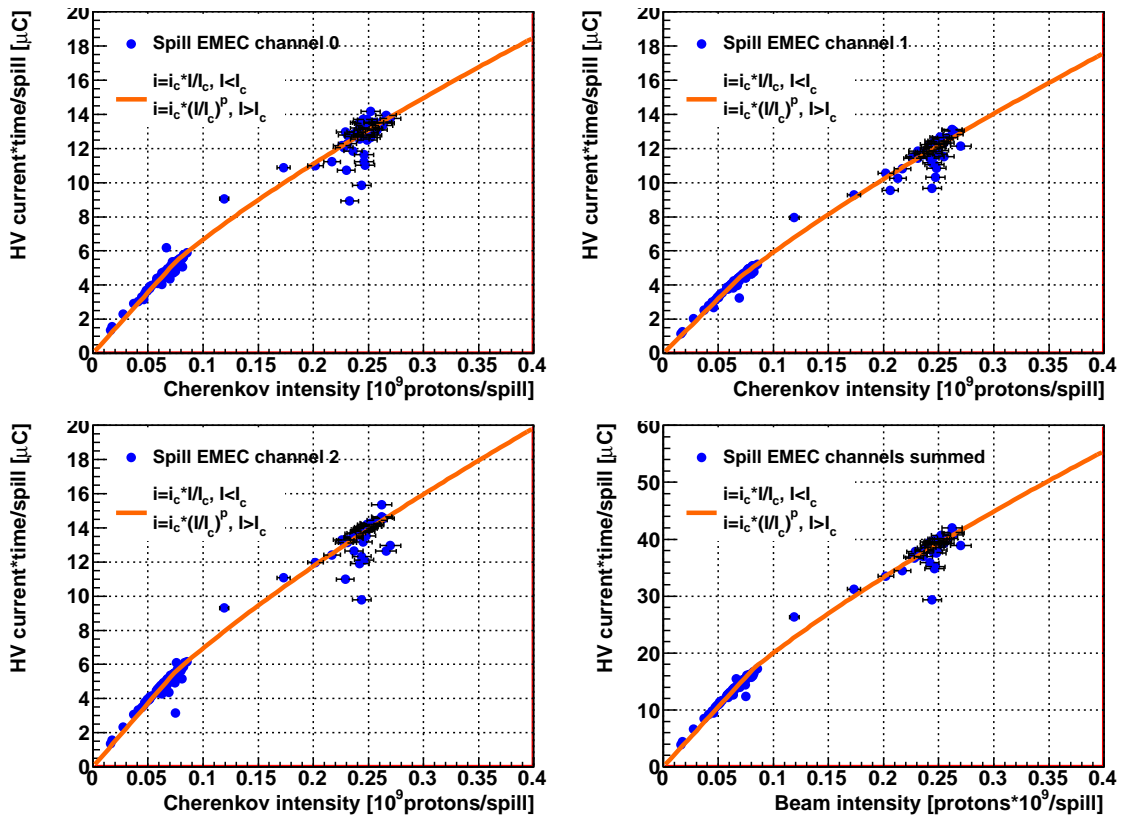


Figure 4.12: HV current in dependence of beam intensity for run period 737-747.

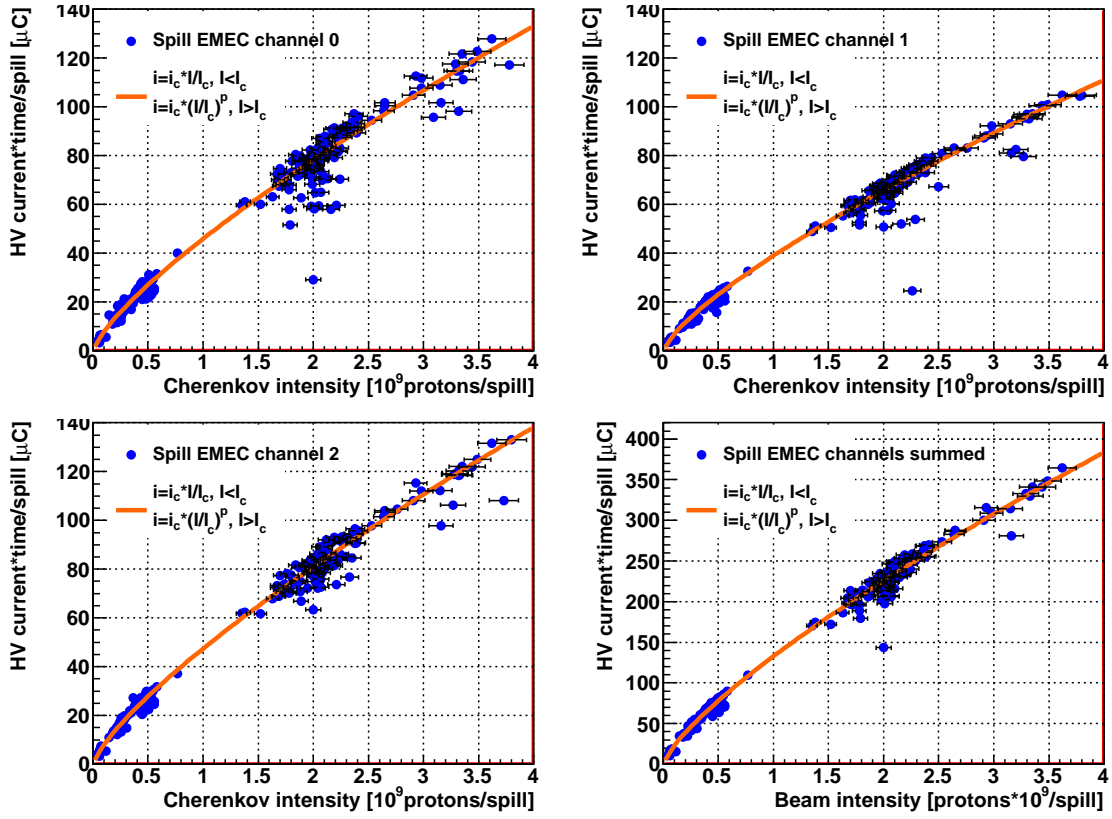


Figure 4.13: HV current in dependence of beam intensity for run period 745-763.

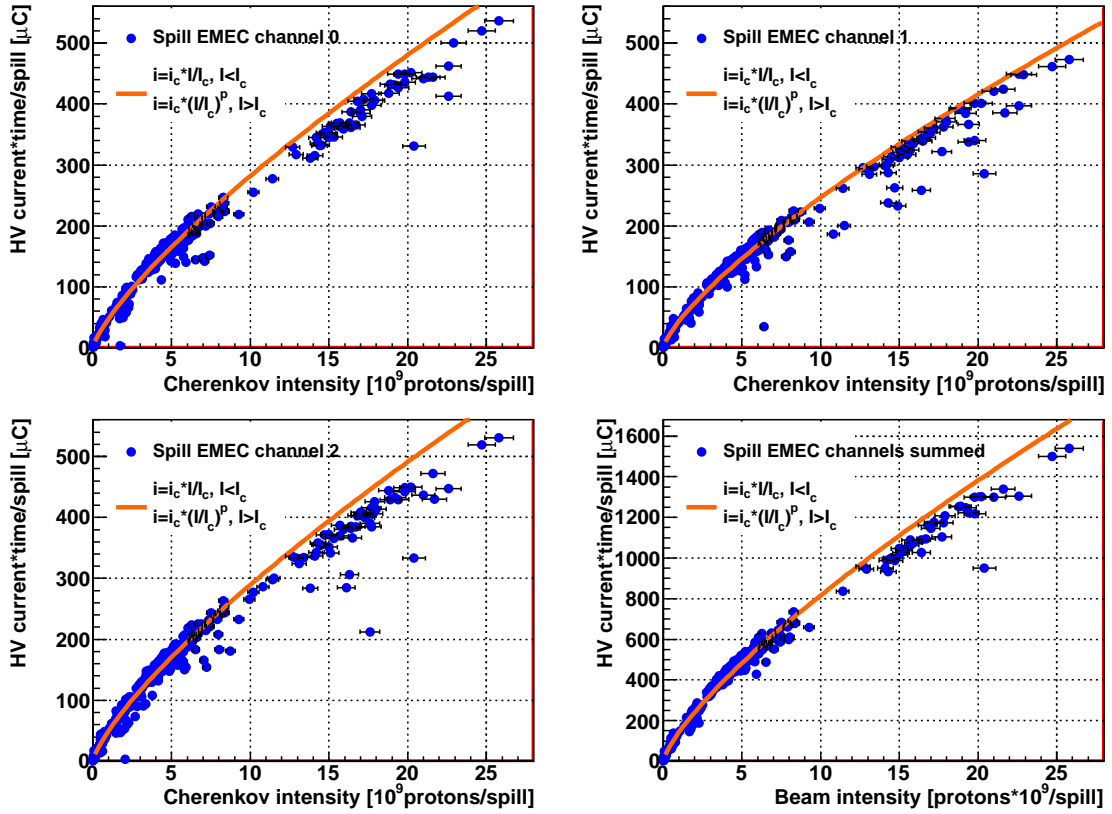


Figure 4.14: HV current in dependence of beam intensity for run period 797-827. The small discrepancies between data and fits at the highest intensities are commented in the text at the end of Section 4.5.6.

Table 4.3: Summary of the fit parameters obtained by applying the fit equation 4.10 to the five analysed run periods. The values for i_c is the integrated current over the spill in $\mu\text{C}/\text{spill}$, while I_c is given in protons/spill. The relevant values are those obtained from the summed channels corresponding to the whole EMEC test module and thus they are highlighted. Uncertainties given with ± 0.00 are smaller than ± 0.005 .

Run period	Channel	I_c [10^8 p/spill]	i_c [$\mu\text{C}/\text{spill}$]	p	χ^2/DoF
712-715	0	0.61 \pm 0.00	6.02 \pm 0.02	0.788 \pm 0.002	3.00
	1	0.71 \pm 0.00	5.62 \pm 0.01	0.784 \pm 0.002	0.87
	2	0.47 \pm 0.03	5.05 \pm 0.26	0.789 \pm 0.002	0.88
	$\sum(0, 1, 2)$	0.50\pm0.00	14.69\pm0.04	0.792\pm0.002	1.04
718-727	0	0.60 \pm 0.00	5.63 \pm 0.02	0.757 \pm 0.002	3.41
	1	0.28 \pm 0.00	2.61 \pm 0.01	0.769 \pm 0.002	1.92
	2	0.28 \pm 0.00	3.22 \pm 0.03	0.762 \pm 0.003	1.68
	$\sum(0, 1, 2)$	0.28\pm0.00	8.90\pm0.04	0.765\pm0.002	1.84
737-747	0	0.77 \pm 0.00	5.49 \pm 0.02	0.736 \pm 0.004	4.52
	1	0.69 \pm 0.47	4.44 \pm 1.00	0.785 \pm 0.999	2.27
	2	0.75 \pm 0.00	5.59 \pm 0.02	0.757 \pm 0.004	4.11
	$\sum(0, 1, 2)$	0.82\pm0.00	17.33\pm0.06	0.736\pm0.005	2.49
745-763	0	0.80 \pm 0.02	6.62 \pm 0.17	0.768 \pm 0.002	11.07
	1	0.87 \pm 0.02	6.18 \pm 0.25	0.756 \pm 0.002	7.50
	2	0.75 \pm 0.00	6.46 \pm 0.14	0.771 \pm 0.001	5.64
	$\sum(0, 1, 2)$	0.81\pm0.02	19.45\pm0.47	0.766\pm0.002	4.96
797-827	0	0.34 \pm 0.00	3.58 \pm 0.01	0.769 \pm 0.001	31.71
	1	0.67 \pm 0.00	5.72 \pm 0.02	0.753 \pm 0.001	33.61
	2	0.58 \pm 0.00	5.73 \pm 0.01	0.762 \pm 0.001	35.25
	$\sum(0, 1, 2)$	0.68\pm0.00	18.46\pm0.05	0.758\pm0.001	25.14

The values obtained for the critical beam intensity and the critical HV current using the extracted spill length are summarized in Table 4.4 for the sum of the three channels. Also the average values for the run periods with 1.0 kV applied and those with 1.2 kV applied are included in the last three rows. For the exponent, p, also the average over all five analysed run periods is given, as it is not expected to depend on the applied high voltage.

The critical values, I_c and i_c , are predicted to depend on the applied high voltage and thus are only averaged for the corresponding run periods with constant voltage. The uncertainties assigned to the average values are not taken from the uncertainties on the fit results themselves, but are calculated as uncertainties of a gaussian mean value as:

$$\Delta X = \frac{1}{\sqrt{l \cdot (l-1)}} \sqrt{\sum_{i=1}^l (X - x_i)^2}, \quad (4.11)$$

if X is the mean of l individual values x . The reason are beam condition fluctuations which lead to rather large variations also between the fit results of run periods with the same high voltage applied. This could be due to beam position fluctuations or instabilities in the beam intensity structure. Therefore, the variations between the run periods are assigned as systematic uncertainties by taking the uncertainty on the average values.

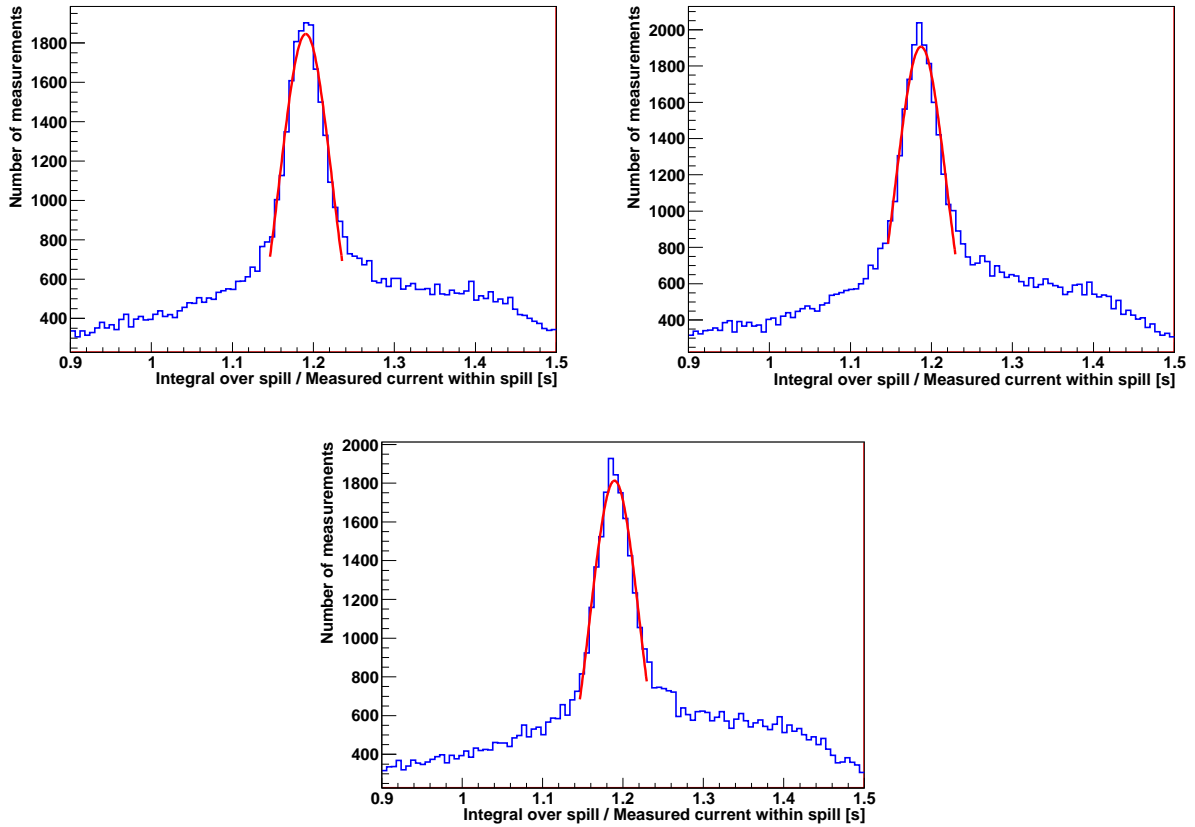


Figure 4.15: Distributions of the integrated HV current over the spill divided by a single measurement within this spill for all signal measurements in the five analysed run periods together. This distribution is shown for each HV channel individually. Top left: channel 0, top right: channel 1, bottom: channel 2. Fits of gaussian functions are applied to evaluate the average initial spill length.

This summarizes all types of possible effects affecting the HV current dependency on the beam intensity. It is much higher than the uncertainty on the obtained fit parameters, which is strongly constrained by the high number of measurements within a run period.

4.5.6 Discussion Considering the Predictions

The comparison of the averaged fit results obtained as summarized in Table 4.4 with the predictions as given in Equations 4.8 and 4.9 lead to lower measured values for I_C and higher measured values for i_C relative to the predictions. The exponent above the critical intensity, p , averaged over all run periods analyzed, agrees well with the model prediction. The comparison of the numbers, together with their deviations, is summarized in Table 4.5. The reasons for the observed deviations are assigned to rather high uncertainties on the particle flux and energy deposits in the calorimeter test modules, predicted by GEANT4 Monte Carlo simulations of the testbeam setup. These are estimated to be $\approx 46\%$ [61] and the uncertainty on the absolute beam intensity measurement is 15% .

This influences the predicted intensity at which space charge effects become important and

Table 4.4: Summary of the fit parameters for the summed channels with I_c and i_c divided by the spill length. The lower three rows give also the values averaged for the 1.0 kV run periods, the 1.2 kV run periods and all five run periods. The global average is not given for the critical intensity and the critical current as a dependence on the applied voltage is predicted. The uncertainties given for the averaged values are not the averaged uncertainties of the fit values, but are calculated as uncertainty on a gaussian mean value. See text for more details. Uncertainties given with ± 0.00 are smaller than ± 0.005 .

Run period	Applied HV	$\sum(\text{Channels } 0, 1, 2)$		
		$I_c [10^8 p/s]$	$i_c [\mu A]$	p
712-715	1.2 kV	0.42 ± 0.00	12.34 ± 0.03	0.792 ± 0.002
718-727	1.0 kV	0.24 ± 0.00	7.48 ± 0.04	0.765 ± 0.002
737-747	1.0 kV	0.69 ± 0.00	14.56 ± 0.05	0.736 ± 0.005
745-763	1.2 kV	0.68 ± 0.02	16.34 ± 0.39	0.766 ± 0.002
797-827	1.0 kV	0.57 ± 0.00	15.51 ± 0.04	0.758 ± 0.001
Average 1.0 kV runs		0.50 ± 0.14	12.52 ± 2.54	0.753 ± 0.011
Average 1.2 kV runs		0.55 ± 0.14	14.34 ± 2.71	0.779 ± 0.020
Average all runs		-	-	0.763 ± 0.009

Table 4.5: Comparison of obtained parameters averaged over the corresponding run periods with the model predictions. The uncertainties are given as described in the text. For each quantity also the deviation in % relative to the prediction is given.

	1.0 kV runs	1.2 kV runs	all
Predicted $I_c [10^8 p/s]$	0.77	1.15	-
Average measured $I_c [10^8 p/s]$	0.50 ± 0.14	0.55 ± 0.14	-
Deviation	35.1 %	52.2 %	-
Predicted $i_c [\mu A]$	9	11	-
Average measured $i_c [\mu A]$	12.52 ± 2.54	14.34 ± 2.71	-
Deviation	39.1 %	30.4 %	-
Predicted p	0.75	0.75	0.75
Average measured p	0.753 ± 0.011	0.779 ± 0.020	0.763 ± 0.009
Deviation	0.4 %	3.9 %	1.7 %

with it also the predicted and obtained critical intensity I_c .

Given these uncertainties and the large range of beam intensities used for the analysis, the order of the predictions are overall confirmed very well within the uncertainties. The power of the dependence of the HV current on the beam intensity above the critical value should not depend on the absolute calibration uncertainties for the beam intensity and should also depend much weaker on the Monte Carlo simulation results of the test beam setup. The final result for the exponent p is given with $p = 0.76 \pm 0.01$ (rounded result from Table 4.5) with a prediction of $p = 0.75$. Given the model prediction uncertainties of the ionized LAr properties, like the exact recombination rate, w , the obtained agreement is remarkable.

It is observed that in the runs with the highest beam intensity of up to 2.5×10^{10} p /spill, the HV current tends to drop slightly faster than with the power ≈ 0.76 , as can be seen in Figure 4.14. This indicates that the conditions at these very high intensities start to differ from the rather ideal model predictions. A description about the testbeam results of the pulse shape analysis can be found in Appendix B.

4.6 Summary of Results

The overall results of the testbeam study show that the endcap calorimeters, EMEC and HEC, are suitable for an operation in the upgraded LHC environment (compare Appendix B). Below the critical regime, the HV return currents depend linearly on the beam intensity, as could also be confirmed by previous studies [54]. Above the critical intensity, the behaviour becomes non-linear and model predictions could be well confirmed by the obtained testbeam results.

The linear behaviour below critical intensities, respectively luminosities at the LHC, is used to perform a precise relative luminosity determination for ATLAS by measuring the HV currents of the EMEC and FCal calorimeters. This is applied in the 2011 data taking [55] for cross-check measurements and to increase the precision. An accurate luminosity determination is a key issue for many physics analyses, like searches for new physics signatures or cross section measurements.

5 $Z \rightarrow \tau\tau$ Cross Section Measurement with 1.34-1.55 fb⁻¹

5.1 Introduction

In the following, an analysis for measuring the cross section of the process $Z \rightarrow \tau\tau$ is presented. This is an important SM process, sensitive to the proton PDFs and to the $Z \rightarrow \tau\tau$ branching ratio (BR), as well as a crucial background in searches for the Higgs boson at the LHC in the $H \rightarrow \tau\tau$ decay channel.

Measured are the sub-channels $Z \rightarrow \tau\tau \rightarrow \mu\tau_h + 3\nu$, where one tau decays into a muon and two neutrinos and the other into hadrons and one neutrino ($\mu\tau_h$ channel), and $Z \rightarrow \tau\tau \rightarrow e\tau_h + 3\nu$, where the first tau decays into an electron instead a muon ($e\tau_h$ channel). These results are combined with those of the $Z \rightarrow \tau\tau \rightarrow e\mu + 4\nu$ measurement [65]. In the following τ_h stands for a hadronically decaying tau lepton.

The total cross section is obtained by measuring the cross section times branching ratio in the fiducial region (geometrical and kinematical acceptance) and by combining this with the well known BR of the tau lepton and the fraction of events accepted by the fiducial cuts. This fraction is obtained using MC generator level studies.

5.2 Data and Monte Carlo Samples

The analysis is performed with proton-proton collision data at $\sqrt{s} = 7$ TeV recorded by the ATLAS experiment in 2011. The data corresponds to an integrated luminosity of 1.55 fb⁻¹ in the $\mu\tau_h$ channel and 1.34 fb⁻¹ in the $e\tau_h$ channel. The ATLAS data taking is divided into periods, which are named with capital letters starting from A. Each period contains several runs and a run groups together a number of luminosity blocks. The luminosity blocks are defined as intervals of nearly constant instantaneous luminosity and are usually of around 1-2 minutes, while one run corresponds to one LHC fill and is typically of the order of 10 h [49]. Only ATLAS data runs and luminosity blocks are considered, where all detector parts relevant for this analysis are fully operational. This is done by applying a good runs list (GRL), which gives the runs and luminosity blocks, where all detector parts relevant for the analysis are working without problems. This analysis includes data from periods B-J.

The integrated luminosity of each channel is calculated with the official ATLAS luminosity calculation framework [55], applying the GRL and the triggers described in the next section. The different amounts of integrated luminosity in the two channels are due to slightly

different data taking periods included, at which the corresponding trigger is available in stable conditions and was operated without prescales. A prescaled trigger with the prescale factor X means that only every X^{th} triggered event is stored in order to limit the data rate.

A combination of datasets with different and prescaled trigger configuration requires the use of different weighted subsets and results in additional uncertainties. As this and the additional effort are not in relation to the gained amount of statistics, the periods B-E are not included in the analysis of the $e\tau_h$ channel.

5.2.1 Trigger Requirements

The triggers used in the $\mu\tau_h$ channel are isolated (isolation requirements for muons and electrons are explained in Sections 5.4.1 and 5.4.2) muon triggers with $p_T > 15$ GeV. For periods B-I the event filter trigger labelled "EF_mu15i" is used and for period J the trigger labelled "EF_mu15i_medium", which requires slightly tighter identification requirements on the muon, is used. This reduces the trigger rate to compensate for the increased instantaneous luminosity in period J and to keep the triggers without prescale.

In the $e\tau_h$ channel, a combined trigger for electrons and hadronically decaying tau leptons with $E_T > 15$ GeV for the electron part and a threshold of $E_T > 16$ GeV for the visible tau decay products, labelled as "EF_tau16_loose_e15_medium", is used. The muon and electron trigger efficiencies and scale factors are discussed in Section 5.9.1.

5.2.2 Monte Carlo Simulations

Monte Carlo (MC) simulations are used to simulate signal and background processes and to compare them to the measured data. The MC samples are generated starting with matrix elements of the partonic process at $\sqrt{s} = 7$ TeV followed by the hadronization and a full detector simulation of the outgoing particles using the Geant4 program [42, 43], as described in Section 2.3. A set of such simulated events is called a MC sample and includes all relevant information, like the reconstructed charge and four-momenta of all measurable particles as reconstructed by the detector. In contrast to the measured data, also particle truth information is available in MC samples. These are properties like the generated particle kinematics, which can differ from that reconstructed by the detector. This information can be used e.g. to evaluate the detector performance on Monte Carlo basis.

The γ^*/Z signal sample and W background sample, which simulate the production and decay of γ^*/Z and W bosons, are generated with Alpgen [35]. The CTEQ6L1 PDFs [34] with the ATLAS AUET1 tune [40] are used and the hadronization and underlying event are simulated with Herwig [36] and JIMMY [41]. Those samples are split with regard to the number of initial partons (N_{PX}) generated in addition to the hard boson production process. This ranges from zero to five ($N_{\text{P0}} - N_{\text{P5}}$) and is related to the number of additional jets which could be reconstructed in the detector. The γ^*/Z MC samples are also divided in terms of phase space: those with the invariant mass of the decay products at generator level between $10 \text{ GeV} < M_{\ell\ell} < 40 \text{ GeV}$ and those with $M_{\ell\ell} > 40 \text{ GeV}$. Events with $M_{\ell\ell} < 10 \text{ GeV}$ are not included and can be neglected as events with low invariant

masses are rejected by the analysis cuts (see Section 5.5).

The $t\bar{t}$ and diboson samples are generated with MC@NLO [38] and HERWIG [36], respectively. The tau decays are simulated with TAUOLA [66] and the final state radiation is modeled using PHOTOS [67]. For the comparison with the measured data, the samples are normalized to NNLO cross sections [68–70]. A list of the Monte Carlo samples used is given in Tables 5.16, 5.17, 5.18 and 5.19 at the end of this chapter.

5.2.3 Pile-up Simulation

The LHC was running with two different bunch spacing configurations in 2011. One LHC fill consists of several bunch trains with a given bunch spacing within the trains and a larger gap between the trains. During period B the spacing between two bunches inside a bunch train was 75 ns, while 50 ns was used from period D onwards (a summary of the data taking periods was given in Section 3.2.7). Pile-up can be divided into two categories: out-of-time pile-up and in-time pile-up. The first category contains overlapping interactions from two subsequent bunch crossings, while the second category contains several p-p collisions in the same bunch crossing.

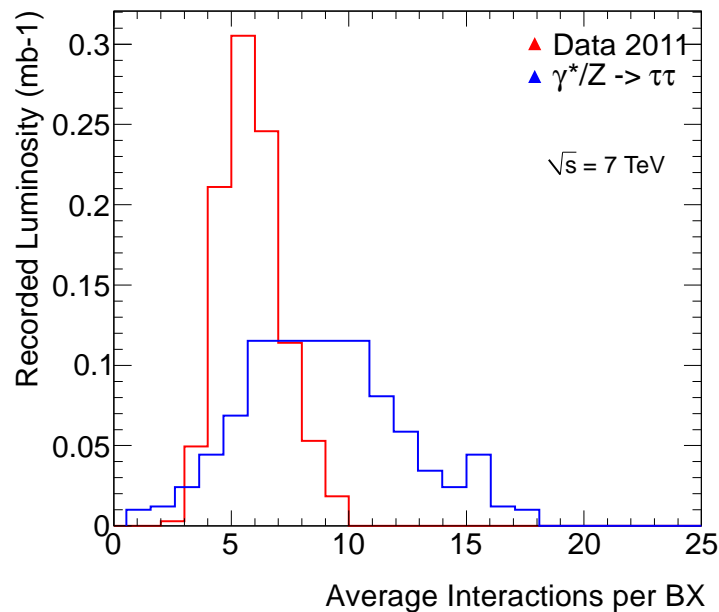


Figure 5.1: Shown is the average number of pile-up interactions, $\langle\mu\rangle$, per bunch crossing (BX) in data (red) and γ^*/Z Monte Carlo (blue) before applying event weights to the MC sample.

In order to account for that, the average number of pile-up interactions per bunch crossing, $\langle\mu\rangle$, is used to categorize the data and Monte Carlo samples. The MC samples are produced with certain pile-up conditions. These usually differ from the conditions in data and therefore a reweighting of the Monte Carlo has to be done. This is done on event level by

comparing the $\langle\mu\rangle$ distribution in data and Monte Carlo and calculating a scale factor with which the Monte Carlo events are weighted. The $\langle\mu\rangle$ distributions of 2011 data and γ^*/Z MC before applying the event weight are shown in Figure 5.1.

5.2.4 Tau Trigger Weighting

The trigger cuts applied on data in the $e\tau_h$ channel could not be simulated in full detail on the Monte Carlo samples since the full information needed for the hadronic tau trigger part is not available. The reason is a change in the tau part of the trigger algorithm during data taking, while the Monte Carlo samples (MC10b production) were produced with the previous algorithm. Therefore, the trigger efficiencies of this part of the trigger are measured in data as a function of E_T of the hadronic tau candidate and applied to all MC samples in the $e\tau_h$ channel as an additional weight. The tau trigger weighting is documented in Appendix C. Since higher order effects are not taken into account by this method, kinematic distributions between data and MC are expected to not agree as good as in the $\mu\tau_h$ analysis channel. This is considered in the systematic uncertainties of the cross section measurement, as described in Section 5.9.

5.3 Event Preselection

After requiring the good run list and the trigger requirements, described in Section 5.2.1, a further preselection of events is applied to reject events which miss quality requirements or contain objects with reconstruction problems.

5.3.1 Good Run List

The Good run list (GRL) is used at the beginning of the event selection to include only those runs where all detector components relevant for this analysis are in nominal condition. The GRL used is generated with the ATLAS GRL generator [71] and is labelled as: "data11_7TeV.periodAllYear_DetStatus-v28-229pro08-07_CoolRunQuery-00-04-00_Z_tautau_1h.xml". The requirements and components verified to function correctly by this GRL are:

- global detector status
- solenoid magnet
- toroid magnet
- muon trigger system
- MUID algorithm for combined muons
- STACO algorithm for combined muons
- electron trigger
- electron combined algorithms (barrel, end caps, forward regions)
- jet trigger
- jet combined algorithms (barrel, end caps, forward regions)
- E_T^{miss} trigger
- E_T^{miss} combined algorithm
- tau trigger
- tau combined algorithm

- pixel vertex layer
- tracking system
- inner detector vertex finding algorithms
- inner detector good beam spot position
- luminosity system.

The total integrated luminosity is calculated including only the runs satisfying these requirements and amounts to 1.55 fb^{-1} in the $\mu\tau_h$ channel and 1.34 fb^{-1} in the $e\tau_h$ channel, as described previously.

5.3.2 Vertex Requirement

Vertex reconstruction algorithms in ATLAS reconstruct event and particle vertices from inner detector tracks and divide them into the categories: primary vertex from a primary proton-proton interaction, and secondary vertex from decays of long-lived particles. Here, collision events are required to have at least one reconstructed primary vertex (PV) with at least four inner detector tracks associated to that vertex. The tracks have to fulfil the following criteria:

- $p_T^{track} > 1 \text{ GeV}$
- $N_{SCT}^{hits} + N_{pixel}^{hits} \geq 7$
- $|d_0^{PV}| < 2 \text{ mm}$
- $|z_0^{PV}| \times \sin \theta < 10 \text{ mm}$,

where d_0^{PV} is the transverse impact parameter with regard to the primary vertex in the R - ϕ plane which also defines the point of closest approach (pca). z_0^{PV} is the distance between the PV and the track on the z -axis in projection of the plane perpendicular to the PV-pca direction. These definitions are illustrated in Figure 5.2.

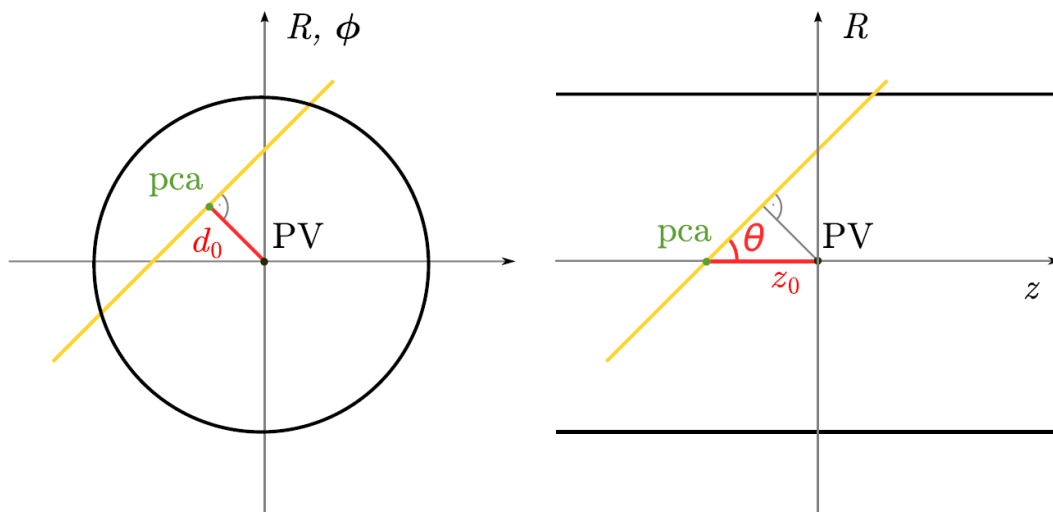


Figure 5.2: Illustration of the definitions of d_0 in the R - ϕ plane (left) and z_0 in the R - z plane (right) [72]. The projection plane for the definition of z_0 is given by the point of closest approach (pca) in the R - ϕ plane. Therefore, the pca is located on the z axis in the R - z plane by definition.

5.3.3 Calorimeter Jet Cleaning

Calorimeter jets are reconstructed from calorimeter cell clusters with a certain signal amplitude above the noise level. A more detailed description of calorimeter jets and their reconstruction is given in Section 5.4.3. Such clusters can be caused not only by particles passing the detector, but also from increased coherent electronic noise levels or discharges in the hadronic end-cap calorimeter or less likely in the electromagnetic calorimeter. Cosmic ray muons passing through the calorimeters and emitting bremsstrahlung can also deposit localized energy uncorrelated with proton-proton collisions.

Such objects can be reconstructed as a jet (fake jets) or distort the measurement of missing transverse energy, E_T^{miss} , significantly. To minimize such events, special dedicated cleaning requirements have been developed by the JetETmiss working group of ATLAS and are applied to the jets. They include cuts on the energy fraction of the jet which is deposited in the electromagnetic or hadronic part of the calorimeter to suppress coherent noise fakes. Also cuts on the time difference between the jet signal and a bunch crossing are applied to suppress fakes originating from cosmic ray muons. The variables used for the jet cleaning are:

- HECf, the energy fraction deposited in the HEC
- EMf, electromagnetic fraction
- LArQ, the energy fraction deposited in LAr cells with a quality factor greater than 4000. The quality factor measures the deviation of the measured pulse shape (s_i^{meas}) to a predicted pulse shape (s_i^{pred}) and is calculated as $\sum_{i \text{ samples}} (s_i^{\text{meas}} - s_i^{\text{pred}})^2$.
- HECQ, the same as LArQ but calculated for the HEC only.
- t, jet timing calculated as the energy squared cells mean time
- Eneg, negative energy on the jet (below noise level)
- CHf, jet charge fraction calculated as the ratio of sum p_T of tracks associated to the jet and the calibrated jet p_T .
- Fmax, maximum energy fraction in one calorimeter layer.

The exact cuts on these cleaning variables applied in the analysis are summarized in Table 5.1. In case at least one jet which fails those cleaning requirements is found, the whole event is rejected. In this way mis-reconstruction of missing transverse energy due to bad quality or fake jets is avoided.

5.3.4 Liquid-Argon Calorimeter Hole Cleaning

During the data taking in 2011, four front-end-boards (FEBs) of the electromagnetic liquid-argon calorimeter stopped working, leading to an area of strongly reduced reconstruction performance. This "liquid-argon hole" was present in the data taking periods E-H. To exclude misidentification or mismeasurement of electrons, hadronically decaying taus or jets in this area, the event is rejected if such an object is reconstructed within this area, as detailed in Table 5.2.

When running over the Monte Carlo events the event is not skipped, if one of those objects falls inside the hole region. Instead a weight is applied to the event, which corresponds to

Table 5.1: Cut values for jet cleaning cuts used in the analysis.

Treatment	Requirements
HEC spikes	(HECf > 0.5 & HECq > 0.5)
	OR E _{neg} > 60 GeV
	OR HECf > (1 - HECQ)
EM coherent noise	EMf > 0.9
	& LArQ > 0.8
	& η < 2.8
Non-collision background and cosmics	t > 10 ns
	OR (EMf < 0.05 & CHf < 0.1 & η < 2.0)
	OR (EMf < 0.05 & η ≥ 2.0)
	OR (F _{max} > 0.99 & η < 2.0)
	OR (EMf > 0.95 & CHf < 0.05 & η < 2.0)

the luminosity fraction in data where the problem was present. This is a fraction of 0.44 in the $\mu\tau_h$ channel and 0.38 in the $e\tau_h$ channel.

Table 5.2: The η and ϕ coordinates for the Liquid-Argon hole cleaning. The limits of the objects can vary as the reconstruction algorithms and e.g. the ΔR cones used can differ. In case at least one object inside the Liquid-Argon hole is found, the event is rejected.

Object	η coordinates	ϕ coordinates
Electrons	$-0.10 < \eta < 1.55$	$-0.888 < \phi < -0.492$
Tau candidates	$-0.10 < \eta < 1.55$	$-0.900 < \phi < -0.500$
Jets	$-0.20 < \eta < 1.60$	$-0.988 < \phi < -0.392$

5.4 Reconstructed Physics Objects

To reduce the amount of proton-proton collision events without interesting signal signature (background), which is orders of magnitude larger than the $Z \rightarrow \tau\tau$ signal, a couple of event and object cuts are applied to the data and in the same way to the MC samples.

Here, the semileptonic decay modes are considered and therefore the signal events are characterized by one isolated (isolation is described in Sections 5.4.1 and 5.4.2) muon or electron and one hadronic tau candidate. The latter one is caused by the tau lepton decaying into hadrons and can be reconstructed as a hadronically decaying tau lepton. The neutrinos from the tau decays lead to a significant missing transverse energy, which can be expected in the signal events.

Overall, the analysis is based on many different physics objects and makes use of the entire ATLAS detector. In the following, when describing particles like electron or muon, always the particle as well as its anti-particle, like positron and anti-muon, is included.

5.4.1 Muons

Muons are unstable particles, but with a mean lifetime of $\tau_\mu = 2.2 \times 10^{-6}$ s [20] they usually fly through the entire detector before they decay. Therefore, they can be directly measured mainly in the inner detector and muon spectrometer as described in Chapter 3.

The muon candidates [73] are reconstructed by combining inner detector tracks with those of the muon spectrometer and considering energy losses in the calorimeter. Both tracks are then used to calculate a combined transverse momentum of the muon, p_T^μ . The p_T^μ is required to be above 17 GeV and the muons also need to be within $|\eta| < 2.4$. Further, inner detector track quality criteria are applied to suppress the amount of fake muons. These criteria include cuts on the number of hits in the B-layer, the pixel detector, the SCT and the TRT. The exact cut values are summarized in Table 5.3. Also, a longitudinal impact parameter requirement of $z_0 < 10$ mm with respect to the primary vertex is required.

Table 5.3: Inner detector quality requirements for muons.

Region	Requirement
$ \eta < 2.7$	$N_{\text{B layer}}^{\text{hits, expected}} = 0 \text{ OR } N_{\text{B layer}}^{\text{hits}} > 0$
	$\& N_{\text{pixel}}^{\text{hits}} + N_{\text{pixel sensors}}^{\text{dead}} > 1$
	$\& N_{\text{SCT}}^{\text{hits}} + N_{\text{SCT sensors}}^{\text{dead}} > 5$
	$\& N_{\text{pixel}}^{\text{holes}} + N_{\text{SCT}}^{\text{holes}} < 3$
$ \eta < 1.9$	$N_{\text{TRT}}^{\text{outliers}} / (N_{\text{TRT}}^{\text{hits}} + N_{\text{TRT}}^{\text{outliers}}) < 0.9$
	$\& N_{\text{TRT}}^{\text{hits}} + N_{\text{TRT}}^{\text{outliers}} > 5$
$1.9 \leq \eta < 2.7$	$(N_{\text{TRT}}^{\text{hits}} + N_{\text{TRT}}^{\text{outliers}} > 5$
	$\& N_{\text{TRT}}^{\text{outliers}} / (N_{\text{TRT}}^{\text{hits}} + N_{\text{TRT}}^{\text{outliers}}) < 0.9$) $\text{OR } (N_{\text{TRT}}^{\text{hits}} + N_{\text{TRT}}^{\text{outliers}}) < 6$

Furthermore, an isolation requirement is applied for the muons, as it is expected that those produced by a Z boson decay, in contrast to muons from heavy quark decay, have less additional energy deposits in a certain cone around it. Therefore an isolation cone of $\Delta R = 0.4$ around the muon candidate is defined and the sum of the transverse momentum of charged particles measured in the inner detector, divided by the transverse momentum of the muon itself, is required to be less than 0.03: $\sum p_T^{\text{track}}(\Delta R < 0.4) / p_T^\mu < 0.03$. Such a requirement is also defined for the sum of the transverse energy measured in the calorimeters around the muon direction. This second isolation requirement is applied as: $\sum E_T^{\text{cell}}(\Delta R < 0.3) / p_T^\mu < 0.04$. The muon momentum or energy is subtracted when calculating the sum within the cone. The distributions of these isolation variables for data and Monte Carlo simulations can be seen in Figure 5.3. The cut values are optimized in terms of QCD multijet suppression and $Z \rightarrow \tau\tau$ signal efficiency.

5.4.2 Electrons

The electron candidates are formed by matching clusters reconstructed in the electromagnetic (EM) calorimeter to inner detector tracks from charged particles. The EM clusters are reconstructed from longitudinal towers with a total reconstructed energy in the transverse

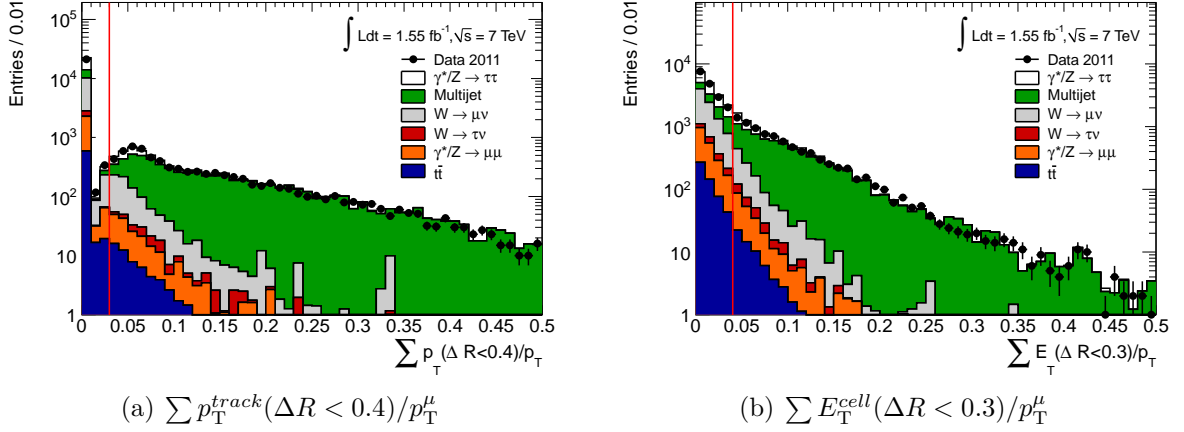


Figure 5.3: The distributions of the isolation variables $\sum p_T^{track}(\Delta R < 0.4)/p_T^\mu$ (a) and $\sum E_T^{cell}(\Delta R < 0.3)/p_T^\mu$ (b). The distributions are shown for muons which have passed the selection requirements except for the isolation. Backgrounds are estimated as described in Section 5.7. The applied cuts are indicated as vertical line.

direction above 2.5 GeV. The reconstructed electron is required to have a transverse momentum, p_T^{el} , greater than 17 GeV and to be within $|\eta| < 2.47$, where the transition region between the barrel and endcap calorimeter, $1.37 < |\eta| < 1.52$, is excluded. Further identification requirements, labelled as tight, are applied. They include tight requirements on the energy-to-momentum ratio and on the track-to-calorimeter-cluster matching criteria of $|\Delta\phi| < 0.02$ and $|\Delta\eta| < 0.005$ [74]. Also, at least one hit in the vertexing layer of the pixel detector to suppress photon conversions and a high ratio of high-threshold to low-threshold hits in the TRT to suppress charged hadrons are required. These cuts are η - and E_T dependent [74]. Further, a transverse impact parameter requirement of $|d_0| < 1$ mm is applied to reject fakes from heavy particle decays with secondary vertices.

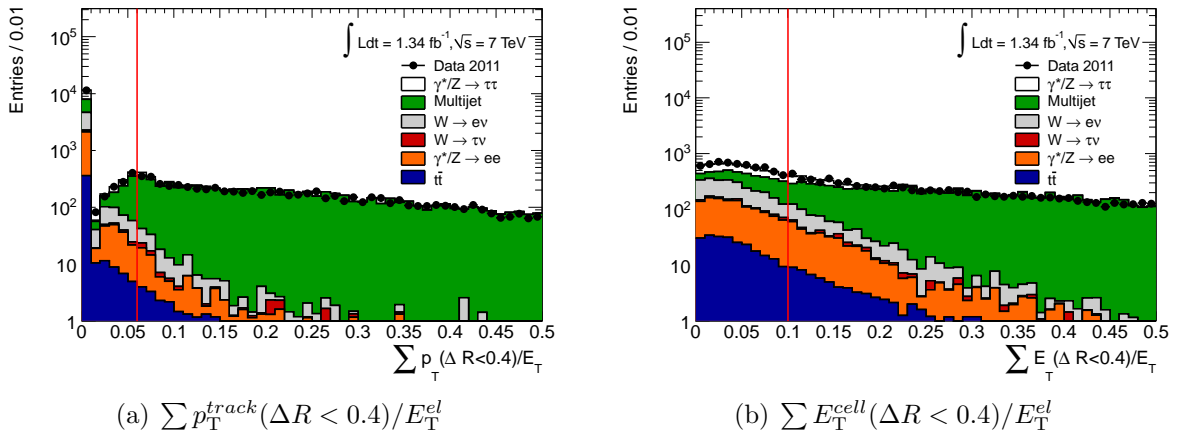


Figure 5.4: The distributions of the isolation variables $\sum p_T^{track}(\Delta R < 0.4)/p_T^{el}$ (a) and $\sum E_T^{cell}(\Delta R < 0.4)/p_T^{el}$ (b). The distributions are shown for electrons which have passed the selection requirements except for the isolation. Backgrounds are estimated as described in Section 5.7. The applied cuts are indicated as vertical line.

Similar to the muons, isolation requirements are defined for the electrons. Here, the total measured transverse track momentum or measured cluster energy in a cone around the electron candidate is divided by the energy of the electron itself as measured in the calorimeter. For the electrons, the optimal isolation requirements found are: $\sum p_{\text{T}}^{\text{track}}(\Delta R < 0.4)/E_{\text{T}}^{\text{el}} < 0.06$ and $\sum E_{\text{T}}^{\text{cell}}(\Delta R < 0.4)/E_{\text{T}}^{\text{el}} < 0.1$. As for the muons, also the momentum or energy of the electron is subtracted from the calculated sum within the cone. The distributions of the isolation variables for the electrons are shown in Figure 5.4 for data and Monte Carlo.

5.4.3 Jets

Calorimeter jets are collections of energy measured in a detector region and most likely caused by the interaction of hadronized quarks or gluons with the detector material. This interaction can produce additional hadrons and leptons, ending up in an electromagnetic cascade. These cascades are measured in the ATLAS sampling calorimeters by cluster algorithms and associating possible inner detector tracks to the reconstructed clusters. Jets are reconstructed in this analysis using the anti- k_{T} algorithm [75], with a distance parameter $R = 0.4$. It uses three-dimensional topological calorimeter energy clusters [76] as input. Jet candidates are required to have $p_{\text{T}}^{\text{jet}} > 20$ GeV and a pseudorapidity within $|\eta| < 4.5$.

5.4.4 Taus

With a mean lifetime of $\tau_{\tau} = 2.9 \times 10^{-13}$ s [20] ($c\tau_{\tau} = 87$ μm), the majority of the tau leptons decay already within the ATLAS beam pipe. Therefore, they can be identified only by their decay products. They decay in 35% of the cases leptonically into an electron and two neutrinos or a muon and two neutrinos and with 65% probability into hadrons and one tau neutrino [20]. The hadronic decay modes are further considered here for the identification and they are dominated by decays into one or three charged pions and possible additional neutral pions plus the neutrino. Hence these decays can be categorized into candidates with one charged track (1-prong tau candidates) and three charged tracks (3-prong tau candidates). Decays with five or more charged hadrons are very rare and therefore can be neglected.

The reconstruction of hadronic tau candidates is seeded by calorimeter jet candidates with a transverse momentum $p_{\text{T}}^{\text{jet}} > 10$ GeV. Then a correction to the reconstructed energy at the electromagnetic scale is applied. Inner detector tracks with $p_{\text{T}}^{\text{track}} > 1$ GeV and fulfilling minimum quality criteria are associated to the tau candidate. These quality criteria are [77]:

- Number of hits in the pixel detector ≥ 2
- Number of hits in the SCT and pixel detector ≥ 7
- $|d_0| < 1.0$ mm
- $|z_0 \times \sin \theta| < 1.5$ mm,

where $|d_0|$ is the closest distance between the track and the primary vertex in the x-y-plane and z_0 is that distance in the z-direction.

Table 5.4: Identification variables for the BDT algorithm to identify hadronically decaying tau leptons.

Variable	Definition	Description
R_{Cal}	$R_{\text{Cal}} = \frac{\sum_i^{\Delta R_i < 0.4} E_{T,i} \times \Delta R_i}{\sum_j^{\Delta R_j < 0.4} E_{T,j}}$	The width of the shower within $\Delta R = 0.4$ weighted by the transverse energy.
f_{HT}	$f_{\text{HT}} = \frac{\text{High-threshold TRThits}}{\text{Low-threshold TRThits}}$	The ratio of high-threshold TRT hits to low-threshold TRT hits is useful to distinguish tau candidates from electrons.
m_{cluster}	$m_{\text{cluster}} = \sqrt{(\sum_{\text{cluster}} E)^2 - (\sum_{\text{cluster}} P)^2}$	The invariant mass of the clusters associated to the seed jet.
$S_{\text{leadtrack}}$	$S_{\text{leadtrack}} = \frac{d_0}{\delta d_0}$	The impact parameter significance of the tau leading track.
f_{core}	$f_{\text{core}} = \frac{\sum_i^{\Delta R_i < 0.1} E_{T,i}}{\sum_j^{\Delta R_j < 0.4} E_{T,j}}$	The transverse energy fraction within the cone $\Delta R = 0.1$ of the tau candidate.
m_{tracks}	$m_{\text{tracks}} = \sqrt{(\sum_{\text{tracks}} E)^2 - (\sum_{\text{tracks}} P)^2}$	The invariant mass of the tracks associated to the tau candidate.
R_{track}	$R_{\text{track}} = \frac{\sum_i^{\Delta R_i < 0.4} p_{T,i} \times \Delta R_i}{\sum_i^{\Delta R_i < 0.4} p_{T,i}}$	The width of the tau track system, weighted by the transverse momentum.
$S_{\text{T}}^{\text{flight}}$	$S_{\text{T}}^{\text{flight}} = \frac{L_{\text{T}}^{\text{flight}}}{\delta L_{\text{T}}^{\text{flight}}}$	The significance of the transverse flight length, calculated from the secondary vertex of multi-prong tau candidates.
f_{track}	$f_{\text{track}} = \frac{p_{\text{T}}^{\text{leading track}}}{p_{\text{T}}^{\text{taucandidate}}}$	The momentum fraction of the leading track associated to the tau candidate.
$f_3^{\text{lead cluster}}$	$f_3^{\text{lead cluster}} = \frac{E_{\text{3 highest energy clusters}}}{E_{\text{all clusters of the tau candidate}}}$	The ratio of the energy of the three highest energy clusters to all clusters, corresponding to the tau candidate.
ΔR_{max}	$\Delta R_{\text{max}} = \sqrt{(\eta_{\text{tau}} - \eta_{\text{trk}})^2 + (\phi_{\text{tau}} - \phi_{\text{trk}})^2}$	The maximum distance between a track within the core associated to the tau candidate, and the tau axis.
$N_{\text{iso}}^{\text{track}}$	$N_{\text{iso}}^{\text{track}} = \sum(\text{tracks}_{\text{isolation cone}})$	The number of tracks within the isolation cone of the tau candidate.

For this study, tau candidates are required to have $|\eta| < 2.47$, excluding the crack region, $1.37 < |\eta| < 1.52$, and $p_{\text{T}}^{\text{tau}} > 20$ (25) GeV in the $\mu\tau_h$ ($e\tau_h$) channel. The higher $p_{\text{T}}^{\text{tau}}$ requirement in the $e\tau_h$ channel is necessary due to the tau trigger, to avoid the steep part of the turn-on curve, as the tau trigger identification is also included in the trigger algorithm in this channel. In addition, tau candidates which have their leading track within $|\eta| < 0.03$ are excluded, since the misidentification rate from electrons is found to be unacceptably high in this region. The reason is reduced TRT information due to the crack region at $\eta = 0$.

Although hadronically decaying tau candidates are seeded by calorimeter jet reconstruction algorithms, they show some characteristic differences to quark or gluon initiated jets. Taus themselves are light, colourless objects which decay into mesons via weak interaction. This leads to a low hadronic multiplicity and more narrow signatures with a less wide spread energy deposit in the calorimeter, compared to jets. Based on this, a number of detector variables can be found to discriminate hadronically decaying tau candidates from jets on a statistical basis. Here, a τ identification method is used, based on Boosted Decision Trees (BDT) to combine a set of discriminating variables to one output score. The discriminating input variables are defined and described in Table 5.4 and more details can be found in [77]. Distributions of these variables and the BDT output score are studied in Section 5.6 when a pure sample of hadronic tau candidates is obtained after the full event selection.

The cut on the BDT score for the identification is dependent on p_{T} of the tau candidate, as described in [77]. The reason is a p_{T} dependence of some discriminating variables. Finally, a tau identification efficiency is reached which is nearly flat in p_{T} . A medium BDT identification category for the tau candidates is found to give an optimal working point between signal efficiency and background suppression (mainly multijets) for this study. This is done by applying a set of p_{T} dependent cuts on the BDT score. The working point corresponding to approximately 61% overall signal efficiency [77]. Also electrons can be falsely reconstructed as hadronically decaying tau candidates. Therefore, a dedicated selection to reject fake τ candidates from electrons is finally applied. It is based on shower shape variables and track information and is described in detail in [77].

5.4.5 Missing Transverse Energy

As the incoming protons collide in longitudinal direction with a negligible transverse energy, it is known that the transverse momentum sum of the incoming particles before the collision is zero. Due to momentum conservation, also the sum of the transverse momentum components of all outgoing particles after the collision has to be zero. But some particles, like the neutrinos, cannot be measured in the detector and thus are missing in the measured momentum or energy sum. Therefore, the transverse energy which is missing to the measured vector sum for reaching a balance, is called missing transverse energy ($E_{\text{T}}^{\text{miss}}$). It is relevant to get hints about potentially produced neutrinos.

The $E_{\text{T}}^{\text{miss}}$ is constructed from energy deposits in the electromagnetic as well as the hadronic calorimeter and from reconstructed muon tracks. It is calculated as the vectorial sum in the two dimensional plane perpendicular to the beam axis:

$$E_T^{\text{miss } x} = E_T^{\text{miss } x}(\text{calo}) + E_T^{\text{miss } x}(\text{muon}) - E_T^{\text{miss } x}(\text{energy loss}), \quad (5.1)$$

$$E_T^{\text{miss } y} = E_T^{\text{miss } y}(\text{calo}) + E_T^{\text{miss } y}(\text{muon}) - E_T^{\text{miss } y}(\text{energy loss}), \quad (5.2)$$

$$E_T^{\text{miss}} = \sqrt{(E_T^{\text{miss } x})^2 + (E_T^{\text{miss } y})^2}, \quad (5.3)$$

where $E_T^{\text{miss}}(\text{calo})$ is obtained from the energy deposits in the calorimeter cells inside three-dimensional topological clusters. They are associated with identified physics objects and calibrated to the energy scale of the corresponding object. The association order is: electrons, photons, hadronically decaying tau leptons, jets and muons. Remaining cell energy not associated to an identified object is also included in the calculation. $E_T^{\text{miss}}(\text{muon})$ is the vector sum of the measured muon momenta, measured in the muon spectrometer and reconstructed within $|\eta| < 2.7$. In addition, within $|\eta| < 2.5$ only reconstructed muon candidates matched to an inner detector track are considered. Finally, $E_T^{\text{miss}}(\text{energy loss})$ is a term correcting for the energy loss of muons in the calorimeters due to ionization [78]. It is subtracted from the previous terms in order to avoid double counting of the measured muon signal energy.

5.4.6 Overlap Removal

The reconstruction and identification algorithms in ATLAS are such that the same detector signature can be reconstructed by more than one particle reconstruction algorithm. For example, one track with sufficient transverse momentum and matched to a deposition in the calorimeter can be reconstructed as an electron, a tau and also as a jet candidate. To avoid double counting of individual physical objects, an overlap removal is applied to remove objects reconstructed in the same ΔR cone. This is done in order to remove objects with a high misidentification rate and keep those with a low one. Therefore, jets are removed, if they overlap within $\Delta R = 0.4$ with a tau candidate, an electron or a muon. This is relevant for the jet cleaning described above. Tau candidates are removed if they overlap with an electron or a muon within $\Delta R = 0.4$, and electrons are removed if they overlap with a muon within $\Delta R = 0.2$. By applying the overlap removal in this order, the object with the higher reconstruction purity is kept while the one with the lower purity is rejected.

For the overlap removal and also the dilepton veto, described below, not the full object selections are applied, but looser criteria are applied. They are summarized for the electron, muon and hadronic tau candidates in Table 5.5.

Table 5.5: Preselection criteria for electrons, muons, hadronic taus and jets used for the overlap removal and dilepton veto.

Electrons	Muons	Hadronic taus
$E_T > 15 \text{ GeV}$	$p_T > 6 \text{ GeV}$	$p_T > 25 \text{ GeV}$
$ \eta < 2.47$, excluding $1.37 < \eta < 1.52$ medium identification [74]	$ \eta < 2.7$	$ \eta < 2.47$, excluding $1.37 < \eta < 1.52$ $ \eta_{\text{leading track}} < 0.03$

5.5 Event Selection

For measuring the $Z \rightarrow \tau\tau$ cross section, a pure sample of $Z \rightarrow \tau\tau$ events with low background contamination and a selection with optimal purity times efficiency is needed in order to reduce the relative statistical uncertainty. The majority of the large QCD multijet background at a hadron collider is already suppressed by the tau identification and the muon and electron isolation requirements. The selection of event level cuts described in the following sections is applied to suppress mainly events from $W \rightarrow \ell\nu$, $W \rightarrow \tau\nu \rightarrow \ell\nu\nu$, and $\gamma^*/Z \rightarrow \ell\ell$ decays with additional jets, misidentified as a tau decay. In the following ℓ (lepton) stands either for a muon, μ , or an electron, e . Events from those decays, produced with an additional quark or gluon jet faking the tau candidate, have a similar signature as the $Z \rightarrow \tau\tau \rightarrow \ell\tau_h + 3\nu$ signal events with one tau candidate, one muon or electron and possibly missing transverse energy.

5.5.1 Dilepton Veto

Events with more than one muon or electron are rejected which already removes a large amount of the $\gamma^*/Z \rightarrow \ell\ell$ background. The same loosened preselection criteria are applied to the second lepton, as for the overlap removal described previously in 5.4.6. Only those events can pass, where either one of the muons or electrons is not reconstructed or identified as such and where the muon, electron or an additional jet is reconstructed as a tau candidate. Due to their energy deposition in the calorimeter, electrons are much more tau like than muons, this misidentification is much more probable for $\gamma^*/Z \rightarrow ee$ events than for $\gamma^*/Z \rightarrow \mu\mu$ events. The distributions of the number of leptons before applying this veto can be seen in Figure 5.5.

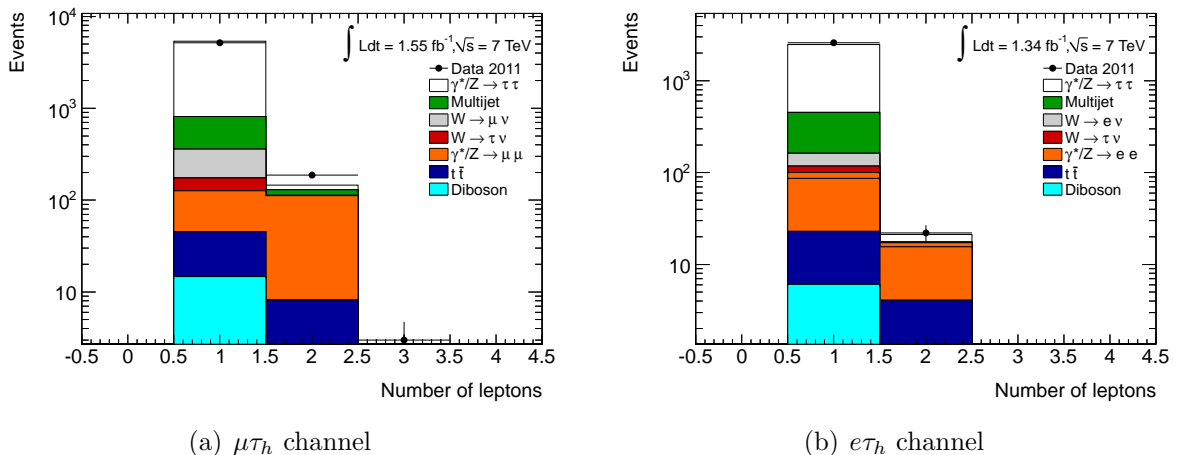


Figure 5.5: The distributions of the number of reconstructed leptons are shown for the (a) $\mu\tau_h$ and (b) $e\tau_h$ final states. The distributions are shown for events which have passed all event selection cuts except the veto itself. Backgrounds are estimated as described in Section 5.7. Smaller deviations as the bin at two leptons in (a) are normal and covered by the uncertainties on the MC simulations as described in Section 5.9.

5.5.2 Opposite Charge Between the Lepton and the Hadronic Tau Candidate

The tau candidate and the lepton need to have opposite charge, as expected in events from a Z decay. In addition to the suppression of multijet background, this reduces also all electroweak background processes with one extra jet faking the hadronic tau candidate.

5.5.3 Reduction of W +jets Background

Mainly cuts on two kinematic variables are used to suppress background from W +jets events. The first discriminating variable is $\sum \cos \Delta\phi$, defined as:

$$\sum \cos \Delta\phi = \cos(\phi(\ell) - \phi(E_T^{\text{miss}})) + \cos(\phi(\tau_h) - \phi(E_T^{\text{miss}})). \quad (5.4)$$

$Z \rightarrow \tau\tau \rightarrow \ell\tau_h + 3\nu$ signal events have their E_T^{miss} pointing in the direction between the hadronically decaying tau and the lepton in the x-y-plane, if the p_T of the Z is non-zero. The reason is that the E_T^{miss} results mainly in the vectorial momenta sum of the neutrinos, which are Lorentz boosted into the direction of the tau or the lepton. This is illustrated in the left picture of Figure 5.6. In this case the variable $\sum \cos \Delta\phi$, as defined above, is positive. It is negative when the E_T^{miss} points away from the direction between the tau and the lepton candidate. This is usually the case for $W \rightarrow \ell\nu$ and $W \rightarrow \tau\nu \rightarrow \ell\nu\nu\nu$ background events, where an additional jet can fake the tau candidate. Here the neutrino balances the lepton in the W -decay, while the jet recoils against the W -system, as illustrated in the middle and right pictures of Figure 5.6. In conclusion, $\sum \cos \Delta\phi$ is mainly at negative values for such background events as can be seen in Figure 5.7, showing the distributions of $\sum \cos \Delta\phi$ for the $\mu\tau_h$ channel and the $e\tau_h$ channel.

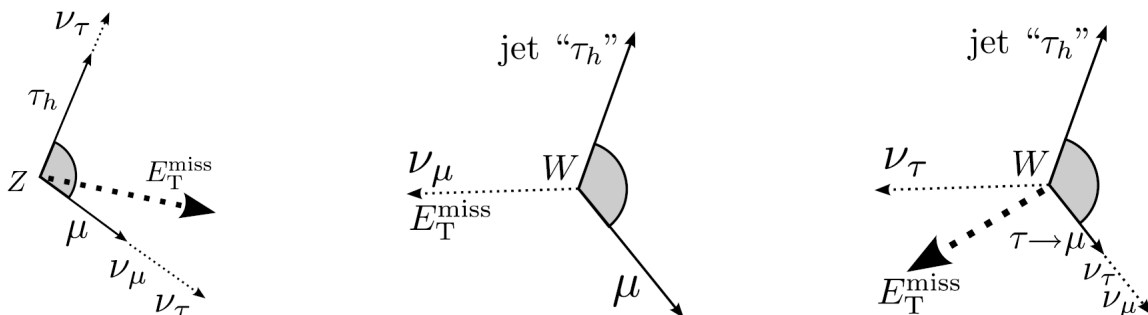


Figure 5.6: Diagrams of Z and W boson decays in the plane fixed by their decay products [79]. Left picture: decay of a Z boson with non-zero transverse momentum into two tau leptons, where one decays further hadronically and the other into a muon and two neutrinos. The E_T^{miss} vector is then the sum of the transverse momenta of the three neutrinos. Middle picture: decay of a W boson into a muon and one neutrino in association with an additional jet which is misreconstructed as a tau candidate, indicated with "tau_h". Right picture: decay of a W boson into a tau lepton and one neutrino, where the tau lepton decays further into a muon and two additional neutrinos.

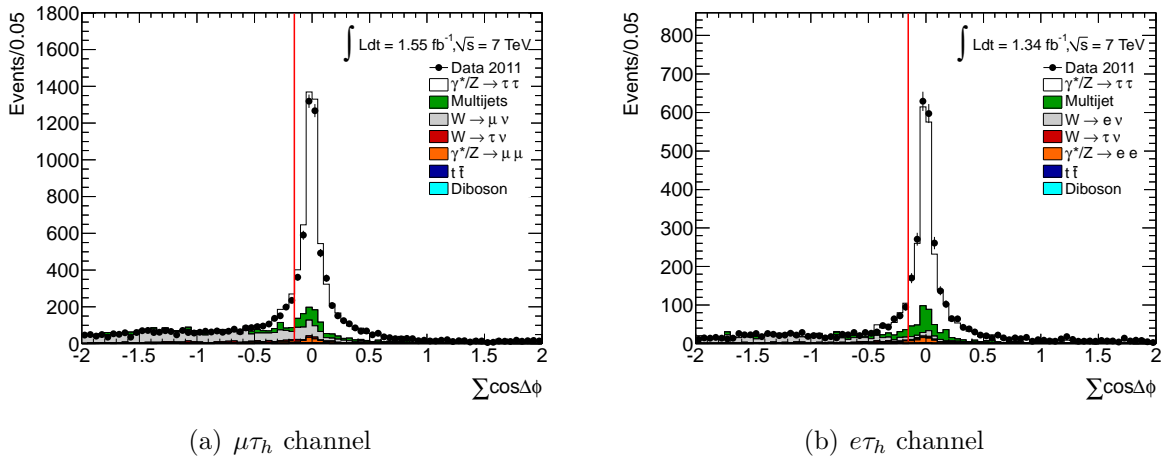


Figure 5.7: The distributions of $\sum \cos \Delta\phi$ are shown for the (a) $\mu\tau_h$ and (b) $e\tau_h$ final states. The distributions are shown for events which have passed all event selection cuts except the cuts on the variables themselves, which are indicated as vertical line. Backgrounds are estimated as described in Section 5.7.

The peak of signal events at around zero corresponds to events where the p_T of the Z is nearly zero. A requirement of $\sum \cos \Delta\phi > -0.15$ is applied to separate signal from background events. For low values of E_T^{miss} the resolution of the direction of E_T^{miss} is reduced. Since in this case $\sum \cos \Delta\phi \approx 0$, these events are kept and the effect is negligible.

To further suppress background events from W decays, the transverse mass is used as second discriminating variable, which is calculated as follows:

$$m_T = \sqrt{2 p_T(\ell) \cdot E_T^{\text{miss}} \cdot (1 - \cos \Delta\phi(\ell, E_T^{\text{miss}}))}. \quad (5.5)$$

Here signal events have on average a smaller angle between the lepton and E_T^{miss} as the decay of the tau into a muon or electron is associated with three neutrinos, whereas that into hadrons only with one neutrino, leading to a E_T^{miss} favoured in the direction of the lepton. This reduces the last factor of the m_T term. Also in contrast to the W decay events described above, the energy of the neutrinos from both tau decays tend to compensate partially, because both taus are back-to-back in first approximation. This, together with the reduced visible lepton p_T due to the neutrinos, suppresses the first factor of the m_T term. Therefore, the $Z \rightarrow \tau\tau$ signal events are expected to accumulate at low values of m_T , whereas the W background events are expected at higher values. This can be seen in the distributions of Figure 5.8. To pass the selection a cut at $m_T < 50$ GeV is required.

5.5.4 Final Requirements on the Tau Candidate

Furthermore, only events are used where the hadronic tau candidate has exactly one or three tracks reconstructed in the inner detector. Also the tau candidate has to have a reconstructed charge of exactly +1 or -1. The charge is calculated as the sum of the track charges as measured in the inner detector. The distribution of the number of tracks for the hadronic tau candidate before these two requirements is shown in Figure 5.9. The signal events in the bin with two tracks consist approximately half of three-prong taus where one

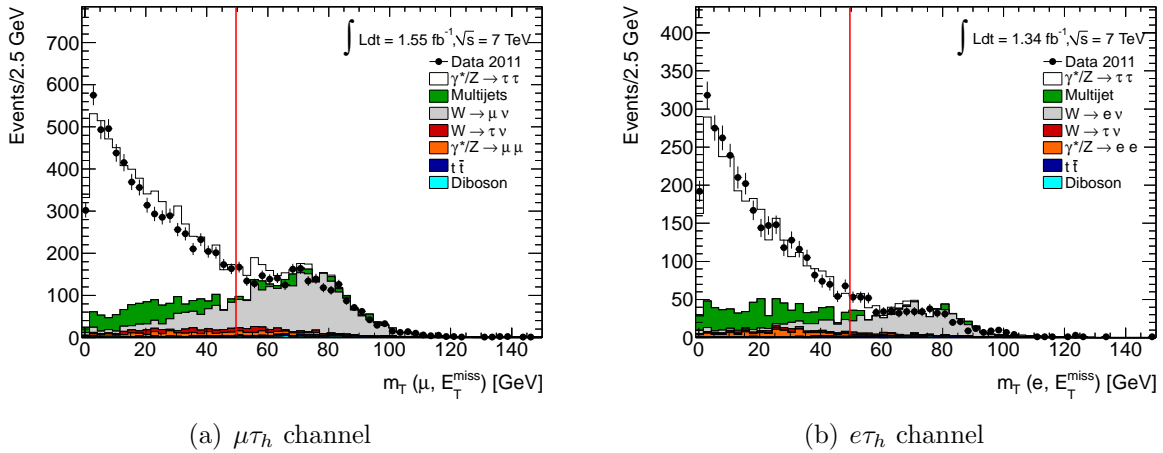


Figure 5.8: The distributions of m_T are shown for the (a) $\mu\tau_h$ and (b) $e\tau_h$ final states. The distributions are shown for events which have passed all event selection cuts except the cut on the variable shown, which are indicated as vertical line. Backgrounds are estimated as described in Section 5.7.

track is not reconstructed or falling inside the crack region of the inner detector. The other half consists of one-track candidates where an additional track close to the tau direction is picked up. This track can come e.g. from tracks produced by other objects in the event, or from a photon conversion in a π^0 decay.

In order to reduce $\gamma^*/Z \rightarrow ee$ events reconstructed as signal, a special dedicated selection to suppress electron fakes is applied to the tau candidate, as described in Section 5.4.4 and Reference [77]. Also muons are able to fake tau candidates, but due to their relatively high mass compared to electrons, the fraction of energy which muons deposit in the electromagnetic calorimeter is comparably small. Therefore, to reduce the number of $\gamma^*/Z \rightarrow \mu\mu$ events where the muon is mis-reconstructed as tau candidate, the fraction of transverse energy deposited by the tau candidate in the e.m. calorimeter is required to be greater than 0.1.

5.5.5 Visible Mass Window

To finally increase the $Z \rightarrow \tau\tau$ signal purity, the invariant mass of the visible decay products of the tau and the lepton, the so-called visible mass m_{vis} , is required to be within $35 \text{ GeV} < m_{\text{vis}} < 75 \text{ GeV}$. As the energy carried away by the neutrinos is not included in m_{vis} , the $Z \rightarrow \tau\tau$ signal peak is shifted away from around 90 GeV like in the $Z \rightarrow ee$ or $Z \rightarrow \mu\mu$ events down to approximately 60 GeV. Therefore, an increased separation between signal and those background events is achieved with that cut.

The distributions of m_{vis} after all previous selection cuts, except the cut on the m_{vis} window, is shown in Figure 5.10 for the $\mu\tau_h$ channel and the $e\tau_h$ channel. Remarkable is the much higher number of $Z \rightarrow ee$ events which pass the event selection until this step in the $e\tau_h$ channel than $Z \rightarrow \mu\mu$ events in the $\mu\tau_h$ channel. This is due to the higher probability that an electron is misidentified as hadronically decaying tau compared to a muon. For the final

event selection the difference in background contribution is small as the visible mass cut suppresses the majority of the $Z \rightarrow ee$ peak.

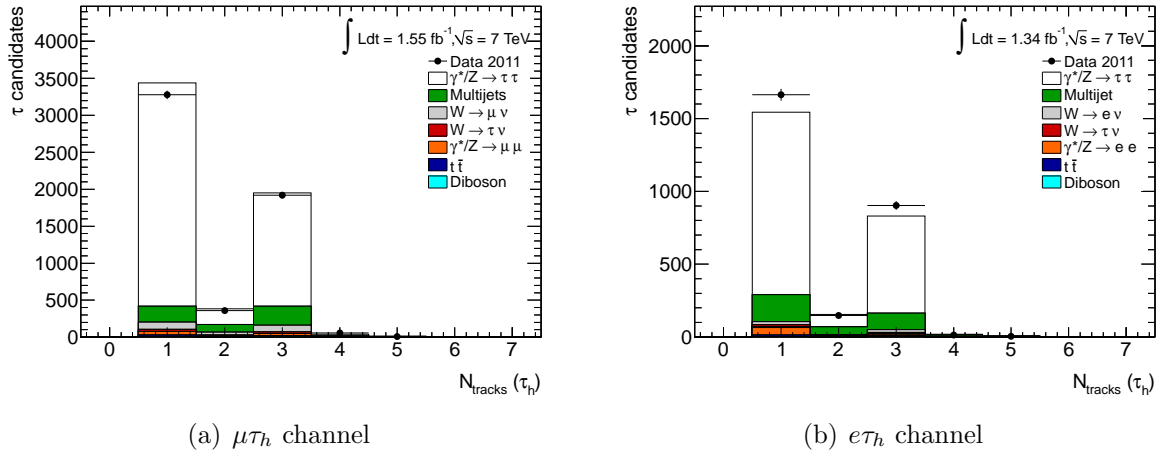


Figure 5.9: The distributions of the number of tracks of the hadronic tau candidate are shown for the (a) $\mu\tau_h$ and (b) $e\tau_h$ final states. The distributions are shown for events which have passed all event selection cuts except the cuts on the number of tracks and the opposite charge requirement. Backgrounds are estimated as described in Section 5.7.

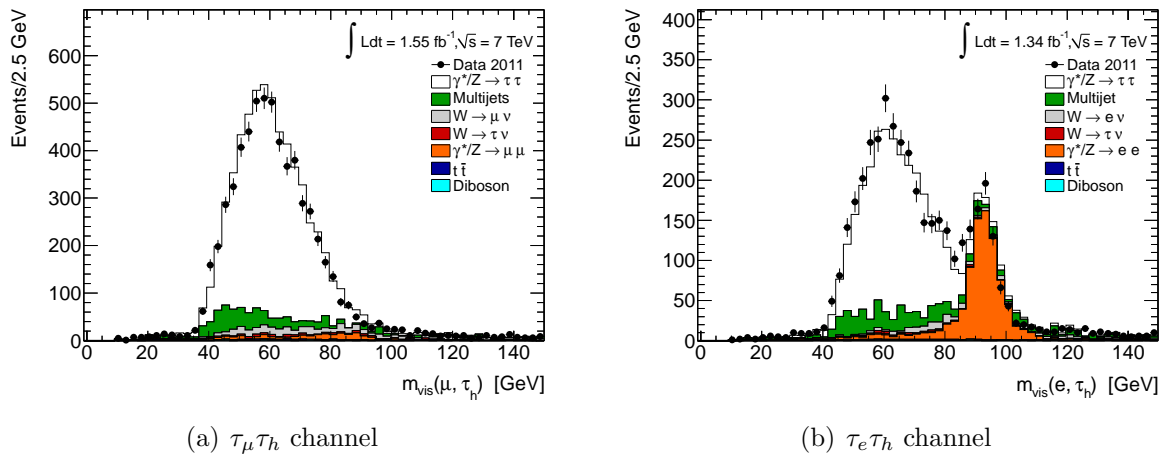


Figure 5.10: The distributions of the m_{vis} are shown for the (a) $\tau_\mu\tau_h$ and (b) $\tau_e\tau_h$ final states. The distributions are shown for events which have passed all event selection cuts except the cut on the m_{vis} window. Backgrounds are estimated as described in Section 5.7.

5.5.6 Summary of the Event Selection

After applying all cuts of the event selection, the final data set for the cross section measurement is obtained. A summary of the cut flow with the number of remaining events after each cut for data and the various Monte Carlo samples is given in Table 5.6 for the $\mu\tau_h$ channel and in Table 5.7 for the $e\tau_h$ channel.

Table 5.6: Cutflow table for the $\mu\tau_h$ channel starting after the full object selection. The multijet background is estimated as described in Section 5.7. This method can only be applied after requiring the opposite sign (OS) cut. The MC simulation event numbers are normalized to an integrated luminosity of $\mathcal{L} = 1.55 \text{ fb}^{-1}$. Uncertainties are described in Section 5.9 and the number of initial MC events is given in Tables 5.16 - 5.19.

	Data	$Z \rightarrow \tau\tau$	Diboson	$t\bar{t}$	$Z \rightarrow \mu\mu$	$W \rightarrow \tau\nu$	$W \rightarrow \mu\nu$	Multijet
Object selection	35020	7857	352	950	4205	1862	28341	-
OS	17550	7059	198	577	1612	461	6886	1363
Dilepton veto	16470	7027	181	458	921	459	6859	1265
W suppression cuts	7397	5788	32	102	408	129	582	764
$N_{\text{tracks}}(\tau_h) = 1$ or 3	6445	5208	27	87	187	103	444	564
$ \text{charge}(\tau_h) = 1$	6422	5200	27	87	186	102	442	555
$35 < m_{\text{vis}}[\text{GeV}] < 75$	5184	4544	15	31	81	49	186	432

Table 5.7: Cutflow table for the $e\tau_h$ channel starting after the full object selection. The multijet background is estimated as described in Section 5.7. The MC simulation event numbers are normalized to an integrated luminosity of $\mathcal{L} = 1.34 \text{ fb}^{-1}$. Uncertainties are described in Section 5.9 and the number of initial MC events is given in Tables 5.16 - 5.19.

	Data	$Z \rightarrow \tau\tau$	Diboson	$t\bar{t}$	$Z \rightarrow ee$	$W \rightarrow \tau\nu$	$W \rightarrow e\nu$	Multijet
Object selection	15200	3393	174	534	2362	291	4660	-
OS	8675	3087	103	340	1575	127	2158	1156
Dilepton veto	8441	3067	97	271	1450	127	2149	1154
W suppression cuts	4649	2570	18	59	900	50	210	726
$N_{\text{tracks}}(\tau_h) = 1$ or 3	4358	2456	16	54	879	41	180	593
$ \text{charge}(\tau_h) = 1$	4351	2453	16	53	878	41	179	584
$35 < m_{\text{vis}}[\text{GeV}] < 75$	2600	2029	6	17	64	18	45	300

To confirm that the kinematics of the physics objects is described correctly by the Monte Carlo simulations, the distributions of the p_T (E_T) of the selected muon (electron) and the (E_T) of the tau candidate are shown in Figures 5.11 and 5.12. Also the missing transverse energy after the full selection is shown in Figure 5.13. An ATLAS event display of a $Z \rightarrow \tau\tau \rightarrow \mu\tau_h$ candidate can be seen in Figure 5.14.

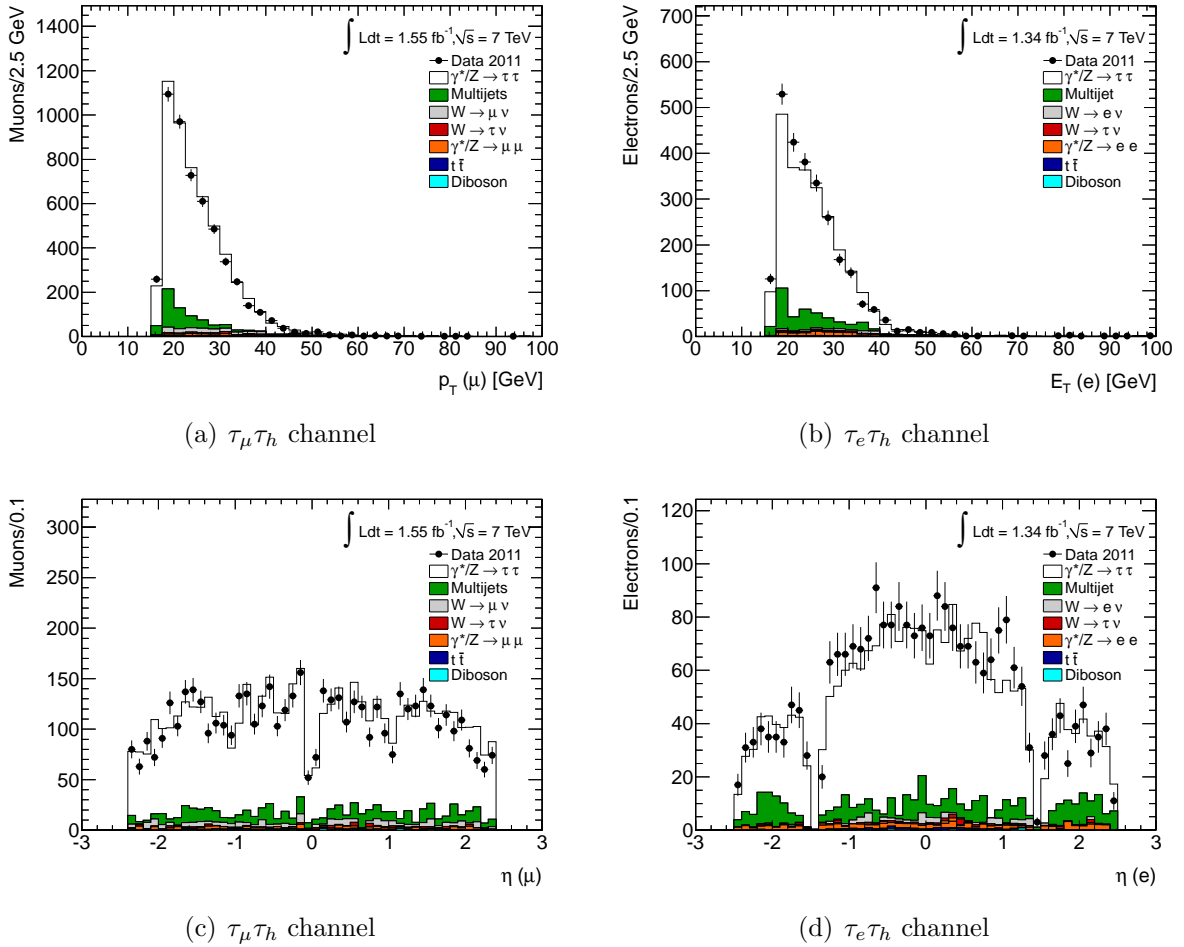


Figure 5.11: The distributions of muon p_T (a) and electron E_T (b) as well as η distributions of the leptons (c) and (d) in the $\tau_\mu\tau_h$ (left) and $\tau_e\tau_h$ (right) final states. The distributions are shown for events which have passed all event selection cuts. Backgrounds are estimated as described in Section 5.7.

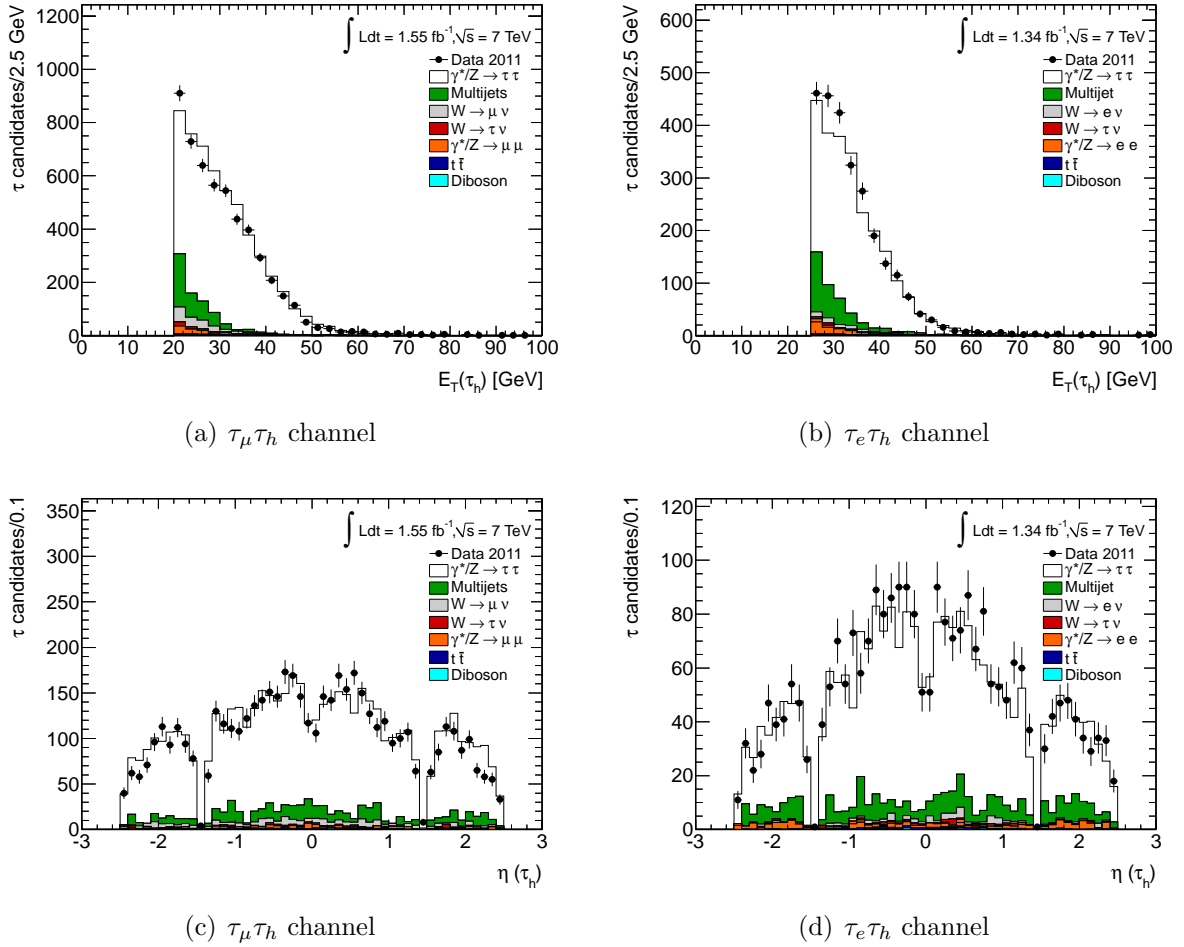


Figure 5.12: The distributions of tau p_T (a) and (b) as well as eta distributions of the tau candidates (c) and (d) in the $\tau_\mu\tau_h$ (left) and $\tau_e\tau_h$ (right) final states. All distributions are shown for events which have passed all event selection cuts.

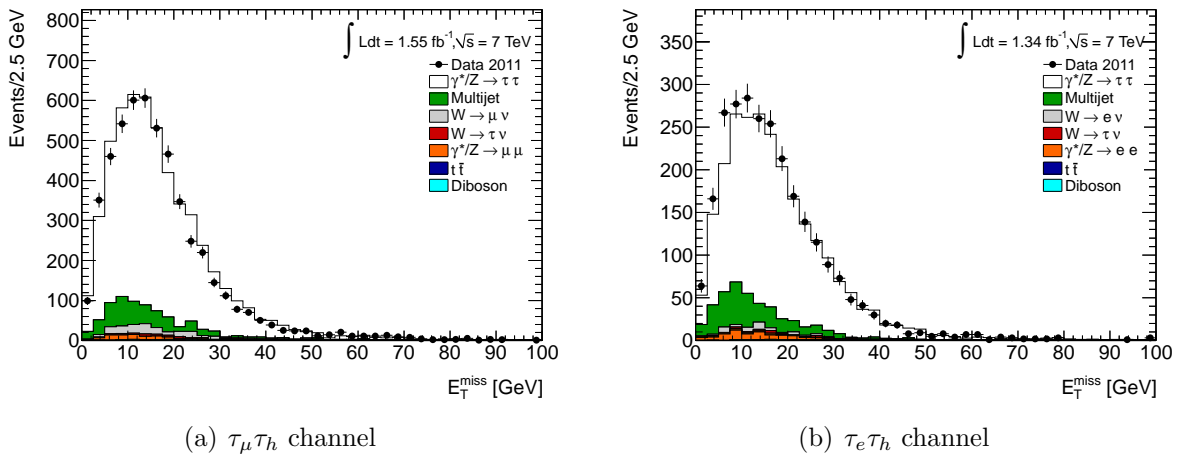


Figure 5.13: The distributions of the E_T^{miss} are shown for the (a) $\tau_\mu\tau_h$ and (b) $\tau_e\tau_h$ final states. The distributions are shown for events which have passed all event selection cuts. Backgrounds are estimated as described in Section 5.7.

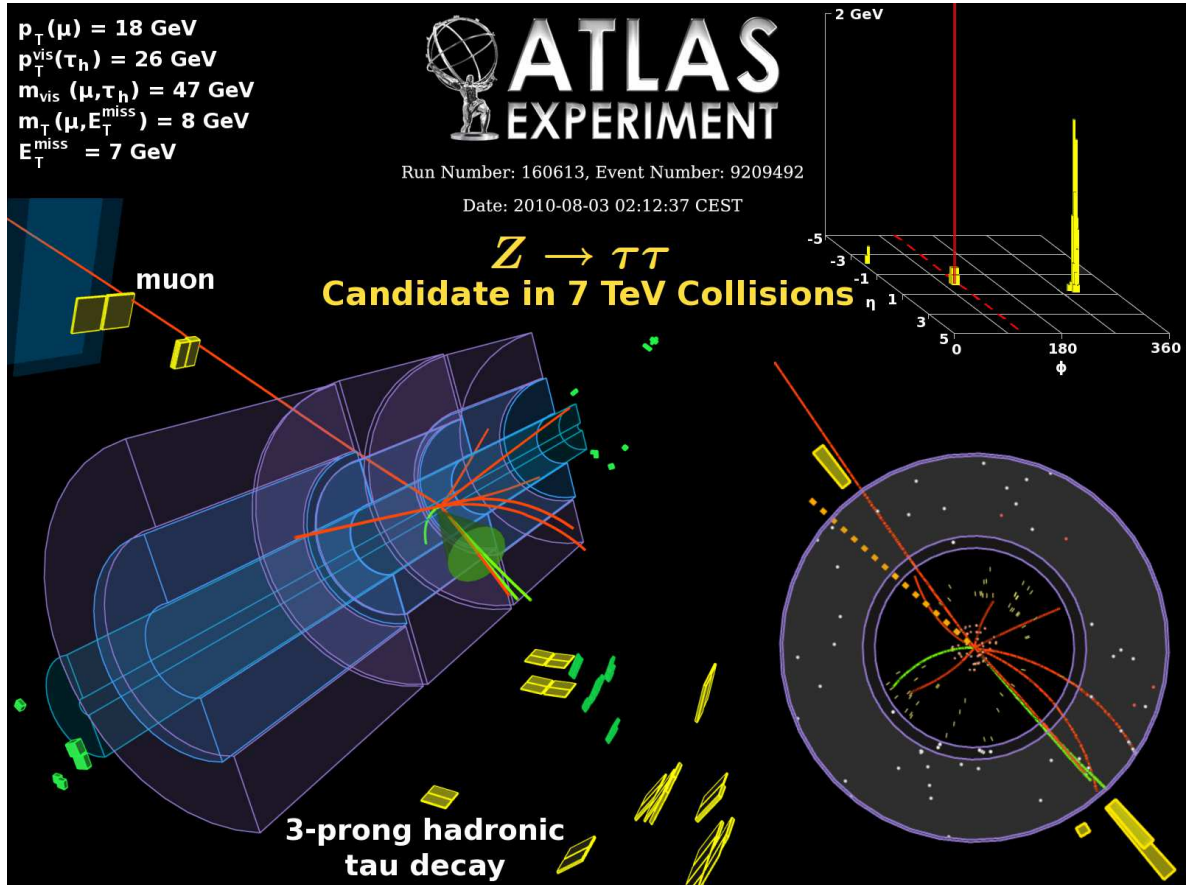


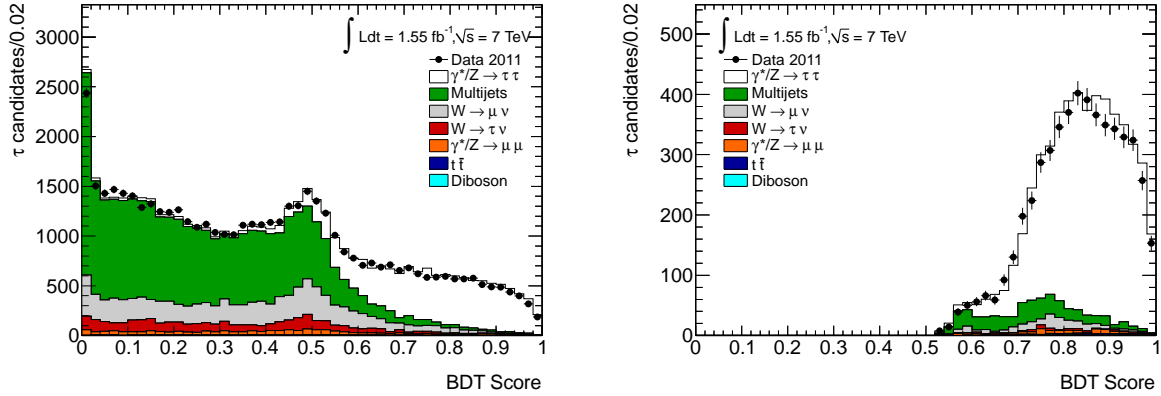
Figure 5.14: Event display of an ATLAS collision data event candidate of a produced Z boson and its decay in the channel $Z \rightarrow \tau\tau \rightarrow \mu\tau_h$ [80]. The visible mass of the muon and the hadronic tau decay products is at 47 GeV.

5.6 Tau Identification Variables

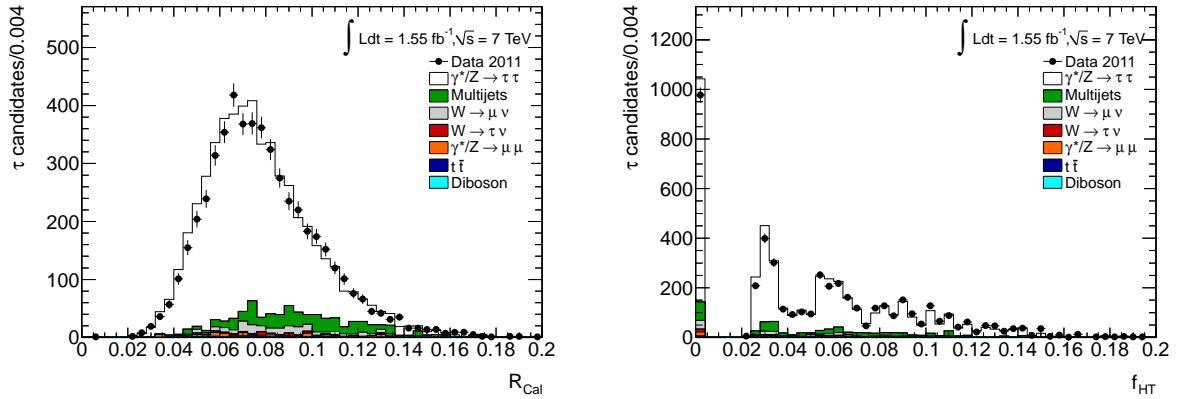
The BDT medium tau identification is applied for the full event selection. The data and Monte Carlo collection obtained after the full selection described in the previous section have a high purity of hadronically decaying tau leptons. This is used to study the variables which are relevant for the BDT score applied in more detail. The hadronic tau part of the trigger in the $\tau_e\tau_h$ channel is applied as a p_T dependent weight on the MC, as described in Section 5.2.4 and Appendix C. This affects these distributions differently compared to data and therefore, the distributions of the tau related variables are analysed in the $\tau_\mu\tau_h$ channel only.

The BDT score before applying the tau identification BDT medium and the cuts on the number of tracks and unit charge of the tau candidate and after applying those is shown in Figure 5.15. This is relevant, because the optimal cut on the BDT score is dependent on the p_T of the tau candidate. The following variables used by the BDT to distinguish tau candidates from multijet background events are also shown in Figure 5.15: The calorimetric radius, R_{Cal} , and the ratio of Transition Radiation Tracker (TRT) hits of the leading track with high threshold to those with low threshold, f_{HT} . Furthermore, Figure 5.16 shows

the invariant mass of the constituent clusters of the seed jet, m_{cluster} , the impact parameter significance of the leading track of the tau candidate, $S_{\text{leadtrack}}$, the core energy fraction, f_{core} , the invariant mass of the track system, m_{tracks} , the track radius, R_{track} , and the transverse flight path significance, $S_{\text{T}}^{\text{flight}}$. These variables have been defined in Table 5.4. Overall, a good agreement of the data and the Monte Carlo description is observed. This is important to get robust and unbiased output results of the BDT identification algorithm.



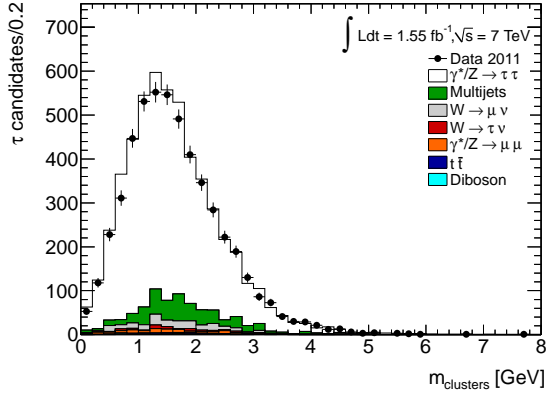
(a) The BDT score before applying the p_{T} dependent BDT medium identification cut. (b) The BDT score after applying the p_{T} dependent BDT medium identification cut.



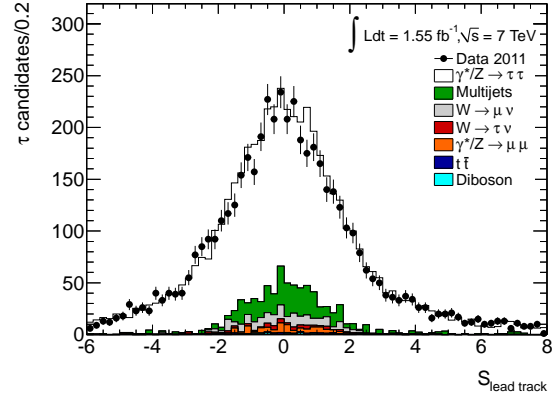
(c) The calorimetric radius.

(d) The TRT HT fraction.

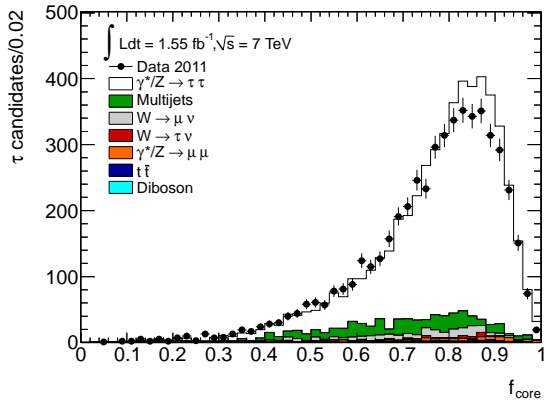
Figure 5.15: The final tau BDT score is shown before applying the tau identification BDT medium (and the cuts on the number of tracks and unit charge of the tau candidate) on the top left and after applying it on the top right plot. Furthermore, the distributions of the following variables relevant for tau identification are shown for events passing the full event selection of the $\tau_{\mu}\tau_h$ channel: The calorimetric radius and the ratio of TRT hits of the leading track with high threshold to those with low threshold.



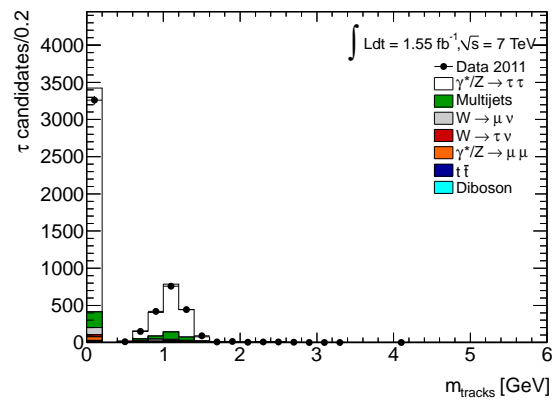
(a) The cluster mass.



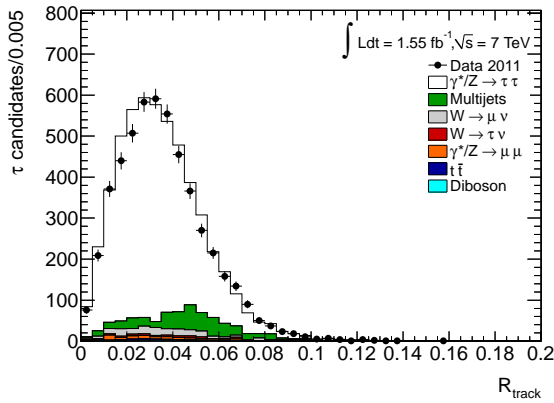
(b) The leading track impact parameter significance.



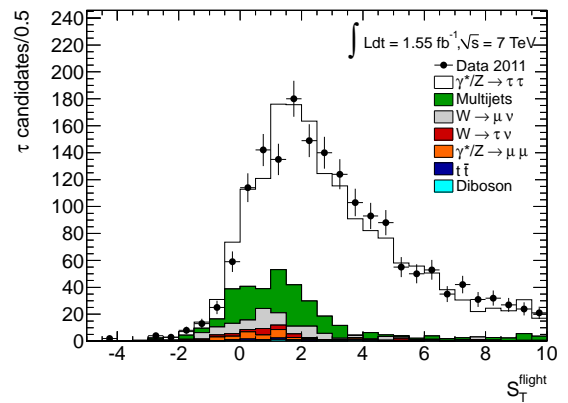
(c) The core energy fraction.



(d) The track mass.



(e) The track radius.



(f) The transverse flight path significance.

Figure 5.16: The distributions of the following variables relevant for tau identification are shown for events passing the full event selection of the $\tau_\mu\tau_h$ channel: The invariant mass of the topological clusters, the impact parameter significance of the leading track, the core energy fraction, the invariant mass of the track system, the average distance of the tracks and the transverse flight path significance.

5.7 Background Estimation

The electroweak background processes, such as $W \rightarrow \ell\nu$, $W \rightarrow \tau\nu$ and $Z \rightarrow \ell\ell$ with additional jets, are estimated using Monte Carlo simulations. Their contribution is small compared to the estimated multijet background as shown in the previous section. But nevertheless, it is important to test the Monte Carlo description of these processes in electroweak-rich control regions. Improper modelling is found after applying the tau identification requirement in case a jet is faking the tau candidate. In this case, these Monte Carlo samples are corrected by scaling factors from sideband regions of the data, as described in sections 5.7.1 and 5.7.2.

The largest background contribution is coming from multijet events as expected at a hadron collider. Due to limited Monte Carlo precision and statistics, the multijet contribution is estimated with a data driven method using three sideband regions as described in section 5.7.3. The $t\bar{t}$ and diboson backgrounds are of minor relevance and their contribution is estimated from Monte Carlo simulations.

5.7.1 W +jets

For the $W \rightarrow \ell\nu$ and $W \rightarrow \tau\nu$ Monte Carlo samples (hence labelled as W +jets) it is found that the tau fake rate of jets is overestimated compared to the measured data. This is mainly due to inaccurately simulated quark-gluon composition of the extra jets. The amount of overestimation is measured by using a W +jets pure sideband region. This region is defined by applying the dilepton veto and the requirements on the tau charge and number of tracks, described in section 5.5, but having the cuts on m_T and $\sum \cos \Delta\phi$ inverted: $m_T > 50$ GeV, $\sum \cos \Delta\phi < -0.15$.

The correction factors are obtained by comparing the yields in the control regions, separately for events with oppositely charged tau candidate and lepton, also called opposite-sign events (OS), and similar charged ones, also called same-sign events (SS). Those factors are hence labelled k_W factors and applied to the W +jets Monte Carlo samples, depending on the charge product requirement applied. The measured values with their statistical uncertainties are given in Table 5.8. The correction factors are slightly different so that the applied correction in the $\tau_e\tau_h$ channel is larger than in the $\tau_\mu\tau_h$ channel. This difference is assigned to the tau trigger issue in the $\tau_e\tau_h$ channel described previously, which biases the misidentified tau candidates in that channel, and also to possible electrons faking tau candidates which is more likely than for muons. The p_T distributions of the hadronic tau candidates in the W enriched control region can be seen in Figure 5.17.

Table 5.8: Correction factors k_W for the W +jets Monte Carlo samples as measured with regard to data. The factors are given with their statistical uncertainties and for events with oppositely charged hadronic tau and lepton (OS) and similar charged ones (SS).

Channel	$k_W(\text{OS})$	$k_W(\text{SS})$
$\tau_\mu\tau_h$	0.54 ± 0.01	0.74 ± 0.03
$\tau_e\tau_h$	0.44 ± 0.02	0.56 ± 0.04

They are shown before the k_W correction factors are applied and the constant offset, nearly independent of the p_T , is visible.

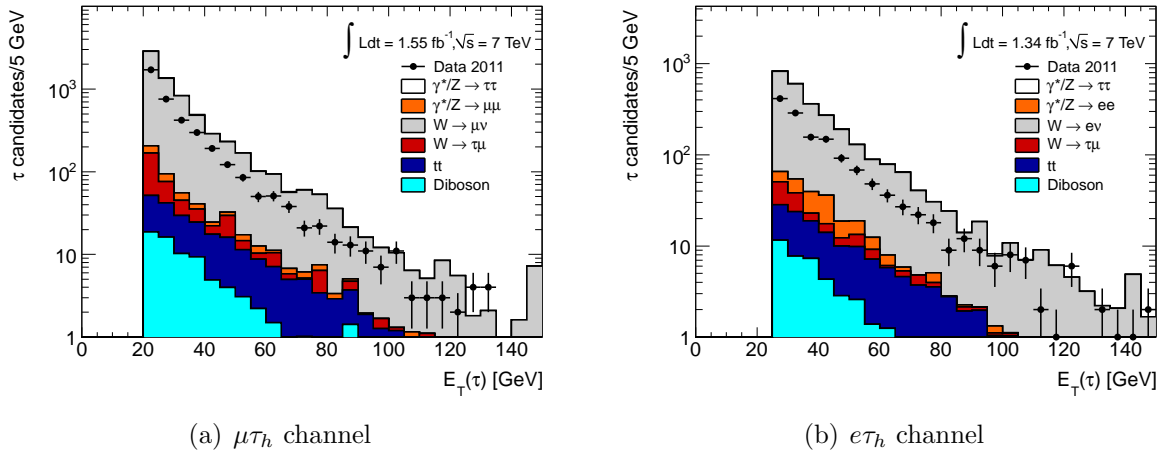


Figure 5.17: The distributions of the E_T of the tau candidate in the W enriched control region are shown for the (a) $\mu\tau_h$ and (b) $e\tau_h$ final states before applying the correction factors.

5.7.2 Z +jets

Similar as for the W +jets background, the estimation of the Z +jets background is based on Monte Carlo samples and correction factors have been applied to account for the overestimated tau fake rate of quark and gluon jets here as well. But two different sources of fake signal events have to be considered. On the one hand, one of the electrons or the muons can be misidentified as hadronic tau candidate while the other lepton is identified correctly (case 1). This case is only relevant for the $\tau_e\tau_h$ channel since the muon-to-tau fake rate is very small.

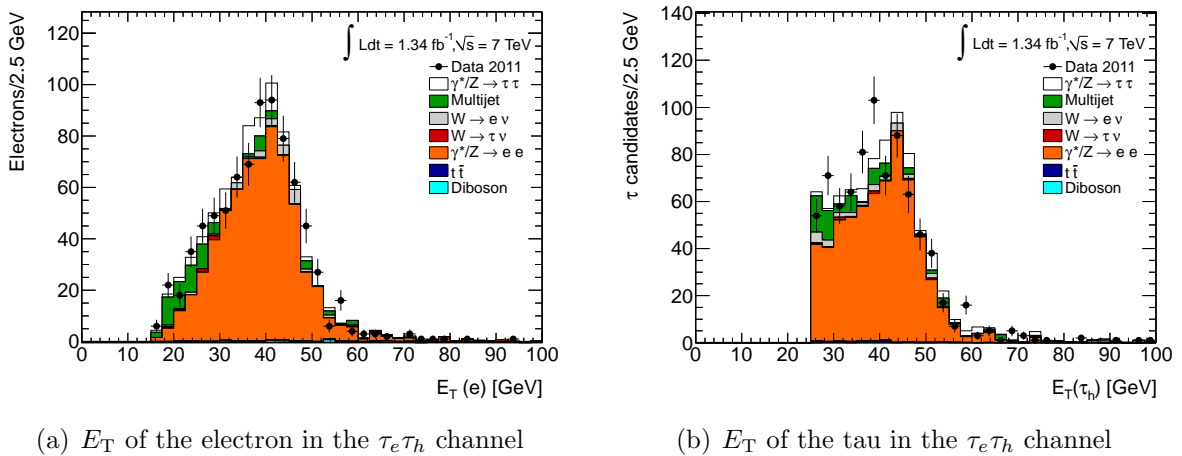


Figure 5.18: The distributions of E_T of the electron (a) and the tau candidate (b) in the Z -enriched control region, where an electron is faking the hadronic tau candidate. Here, a cut on the visible mass of $85 \text{ GeV} < m_{\text{vis}} < 105 \text{ GeV}$ is applied.

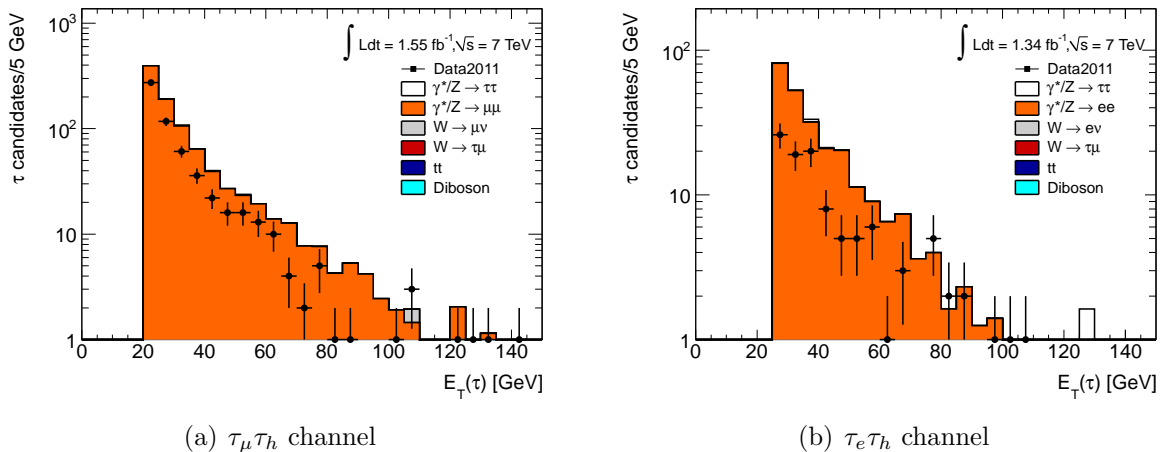


Figure 5.19: The distributions of the E_T of the tau candidate in the Z enriched control region, where an extra jet is faking the hadronic tau candidate, are shown for the (a) $\tau_\mu\tau_h$ and (b) $\tau_e\tau_h$ final states before applying the correction factors.

Secondly, one of the leptons can be missed and an additional jet can be identified as the hadronical decaying tau (case 2). Control regions have to be found to cover both cases separately. This is done as follows: For case 1, the event selection described in section 5.5 is applied, except the cut on the visible mass. Instead, the events are required to be within $85 \text{ GeV} < m_{\text{vis}} < 105 \text{ GeV}$. Here, the electron(muon)-to-tau fake rate is relevant. This is negligible in the $\tau_\mu\tau_h$ channel described correctly by the Monte Carlo in the $\tau_e\tau_h$ channel as can be seen in Figure 5.10 and in Figure 5.18, showing E_T of the electron and the tau candidate in this control region.

In case 2, also the full event selection is applied, except for the cut on the visible mass, and in addition a second preselected electron or muon is required to construct the appropriate control region. This, together with the already selected electron or muon, is then asked to be within an invariant mass window of $66 \text{ GeV} < m_{\text{inv}} < 116 \text{ GeV}$. This selection leads to a very pure sample of $Z \rightarrow \mu\mu$ or $Z \rightarrow ee$ events with one additional jet, which is identified as hadronic tau candidate. This can be seen in Figure 5.19 where the p_T distribution of the tau candidate in this control region is shown.

The k_Z factors are obtained from this region for opposite sign events and are summarized in Table 5.9. They are applied to the Z +jets Monte Carlo samples only, if no Monte Carlo generator level muon or electron is found within a cone of $\Delta R = 0.4$ around the identified hadronic tau candidate. The reason is that in this case the tau candidate has its origin in an additional jet and the correction needs to be applied.

Table 5.9: Correction factors k_Z for the Z +jets Monte Carlo samples as measured with regard to data. The factors are given with their statistical uncertainties and for events with oppositely charged hadronic tau and lepton (OS).

Channel	$k_Z(\text{OS})$
$\tau_\mu\tau_h$	0.57 ± 0.04
$\tau_e\tau_h$	0.39 ± 0.05

5.7.3 QCD Multijet Events

The multijet background is the dominant one and has, compared to the electroweak backgrounds, the largest uncertainties when simulating it with Monte Carlo techniques. Therefore, the multijet background is exclusively estimated using sideband regions from data.

Four control regions (A,B,C,D) are constructed as follows and therefore the method is also labelled: ABCD method. Region A is the signal region after the full selection as describes in Section 5.5, where the multijet background needs to be estimated. Region B requires, instead of opposite charge of the lepton and the tau candidate (OS), the same sign (SS) between them. Region C is constructed by keeping the opposite sign requirement, but inverting the isolation cuts (described in Sections 5.4.1 and 5.4.2) on the leptons, so that events failing these cuts are taken while those passing the isolation cuts are rejected. This includes both, the track-isolation as well as the calorimeter-isolation criteria. Using that requirement, mainly leptons produced from jets are selected and therefore events from multijet background are enriched. Region D has also the inverted isolation criteria, but the same sign requirement on the lepton and the tau candidate. The multijet control regions are illustrated in Figure 5.20.

The amount of multijet events in the signal region A is then estimated as:

$$N_{\text{Multijet}}^A = \frac{N_{\text{Multijet}}^C}{N_{\text{Multijet}}^D} N_{\text{Multijet}}^B = R_{\text{OS/SS}} N_{\text{Multijet}}^B. \quad (5.6)$$

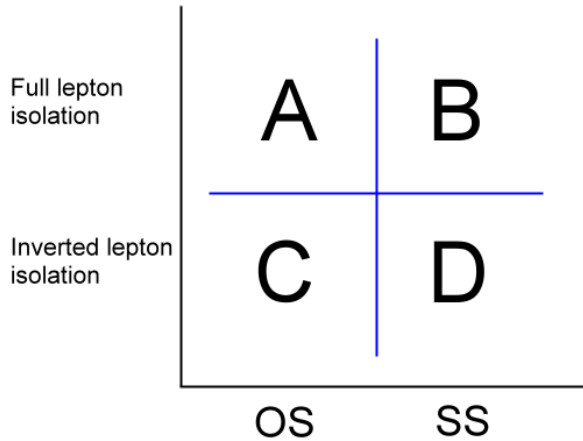


Figure 5.20: Scheme of sideband control regions for multijet estimation. On the horizontal axis, the charge product of the hadronically decaying tau candidate and the electron or muon is drawn, where OS means opposite charge (negative charge product) and SS stands for same sign (positive charge product). The vertical axis indicates the lepton isolation as labelled. Region A is the $Z \rightarrow \tau\tau$ signal region, while the regions B, C and D are multijet enriched control regions which are used to estimate the multijet contribution in region A.

Table 5.10: Number of events in the ABCD control regions used for the multijet background estimation. Signal and other background processes are estimated from Monte Carlo, while the number of Multijet events is estimated from data after subtracting the EW processes. The highlighted number of multijet events in signal region A is obtained from the ABCD method as described in the text. The total background is relevant and given for the signal region A only by summing up all backgrounds from Monte Carlo including the applied corrections and the estimated multijet background.

Control region	$\tau_\mu\tau_{had}$ channel				$\tau_e\tau_{had}$ channel			
	A	B	C	D	A	B	C	D
data	5184	577	1728	1352	2600	353	2626	2403
$Z \rightarrow \tau\tau$	4544	44	196	1	2029	19	71	4
$Z \rightarrow \ell\ell$	81	57	2	4	64	29	3	-
$W \rightarrow \ell\nu$	186	64	12	1	45	15	2	-
$W \rightarrow \tau\nu$	49	22	2	-	18	5	1	-
$t\bar{t}$	31	5	2	-	17	2	3	1
Di-Boson	15	1	-	-	6	1	-	-
Multijet	432	384	1514	1345	300	282	2546	2397
Total background	793	-	-	-	449	-	-	-

$R_{OS/SS}$ is the ratio of OS events to SS ones, which is obtained from control regions C and D. Contributions from $Z \rightarrow \ell\ell + jets$, $W + jets$, $t\bar{t}$ and diboson events as well as $Z \rightarrow \tau\tau + jets$ signal events, are obtained from Monte Carlo and subtracted from the data in the regions B,C and D. The measured opposite sign to same sign ratios for multijet events are:

$$R_{OS/SS} = \begin{cases} 1.13 \pm 0.04 \text{ (stat.)} & \tau_\mu\tau_{hchannel}, \\ 1.06 \pm 0.03 \text{ (stat.)} & \tau_e\tau_{hchannel}. \end{cases} \quad (5.7)$$

Therefore, the ratios are close to unity, as expected for multijet events. For including the estimated multijet background into the Figures, this ratio serves hence as normalization while the shape is taken from the isolated control region B. The corresponding numbers of data and Monte Carlo events in the four regions are summarized in Table 5.10. As can be seen, the contribution from $Z \rightarrow \tau\tau$ signal events in the control regions B, C and D is comparably small so that the effect of its theoretically assumed cross section can be neglected in the final cross section measurement.

5.8 Cross Section Measurement

After measuring the number of data and background events in the $Z \rightarrow \tau\tau$ signal region, the cross section times branching ratio can be calculated using the following equation:

$$\sigma(Z \rightarrow \tau\tau) \times BR(\tau \rightarrow \ell\nu\nu, \tau \rightarrow \tau_{had}\nu) = \frac{N_{obs} - N_{bkg}}{A_Z \cdot C_Z \cdot \mathcal{L}}, \quad (5.8)$$

with N_{obs} being the number of data events and N_{bkg} the number of background events. A_Z is the geometrical and kinematical acceptance for the $Z \rightarrow \tau\tau$ signal process. It accounts for the fact that not all signal events can be measured, if the decay products are located for

example at high rapidities outside the detector acceptance or have low p_T below the trigger threshold or the offline p_T cut. A_Z is calculated from Monte Carlo at generator level by

$$A_Z = \frac{N_{acceptance}^{gen\ kin}}{N_{born}^{gen\ m_{inv}}}, \quad (5.9)$$

where $N_{acceptance}^{gen\ kin}$ is the number of generated $Z \rightarrow \tau\tau$ signal events which are within the geometrical and kinematical acceptance (fiducial region) of the analysis. $N_{born}^{gen\ m_{inv}}$ is the total generated number of events with an invariant mass of the two taus at born level, e.g. excluding FSR, within $66 \text{ GeV} < m_{inv} < 116 \text{ GeV}$. The kinematical and geometrical acceptance is defined by the following cuts, which are applied at generator level to obtain $N_{acceptance}^{gen\ kin}$.

$\tau_\mu\tau_h$ channel:

- Muon: $p_T > 17 \text{ GeV}$, $|\eta| < 2.4$
- Tau: $E_T > 20 \text{ GeV}$, $|\eta| < 2.47$, excluding $1.37 < |\eta| < 1.52$
- Event: $\Sigma \cos \Delta\phi > -0.15$, $m_T < 50 \text{ GeV}$, m_{vis} within $[35, 75] \text{ GeV}$

$\tau_e\tau_h$ channel:

- Electron: $E_T > 17 \text{ GeV}$, $|\eta| < 2.47$, excluding $1.37 < |\eta| < 1.52$
- Tau: $E_T > 25 \text{ GeV}$, $|\eta| < 2.47$, excluding $1.37 < |\eta| < 1.52$
- Event: $\Sigma \cos \Delta\phi > -0.15$, $m_T < 50 \text{ GeV}$, m_{vis} within $[35, 75] \text{ GeV}$

For these requirements at generator level, the E_T^{miss} for the calculation of $\Sigma \cos \Delta\phi$, m_T and m_{vis} is obtained by the sum of the transverse components of the neutrino momenta. Also, the decay products of the Monte Carlo generator level tau leptons are considered together with photons radiated from the decay products or the tau leptons themselves within a ΔR cone. This cone is $\Delta R < 0.1$ in case of leptonic tau decay products (muons or electrons) and $\Delta R < 0.4$ in case of hadronic tau decays. This leads to a correction of the final state radiation (FSR) back to the born level for radiation angles within the ΔR cone. Also events are included which migrate from outside the invariant mass window into the fiducial region by FSR.

The acceptances A_Z for both analysis channels are obtained using the PYTHIA Monte Carlo generator with modified leading order (LO) parton distribution function (PDF) MRSTLO* [81] and the corresponding ATLAS MC10 tune [82]. This Monte Carlo sample includes events with invariant masses down to 10 GeV. Those can migrate from outside the invariant mass window into the fiducial region. The PYTHIA instead of the Alpgen generator is used here, because of an inaccurate description of the Z rapidity when using ALPGEN with the CTEQ6L1 PDF set. This does not affect the reconstruction-level event kinematics, but the extrapolation to the total cross section.

Further, C_Z is the efficiency of the used triggers, reconstruction and identification methods within the fiducial region of the $Z \rightarrow \tau\tau$ events. It is calculated as

$$C_Z = \frac{N^{reco\,pass}}{N_{acceptance}^{gen\,kin}}, \quad (5.10)$$

with $N^{reco\,pass}$ being the number of signal events which have passed all analysis cuts after the full simulation and $N_{acceptance}^{gen\,kin}$ being all signal events generated within the fiducial region as defined above. C_Z is obtained using the Alpgen Monte Carlo generator with the CTEQ6L1 PDF configuration [34].

Finally, \mathcal{L} in Equation 5.8 is the total integrated luminosity of the corresponding channel. Its uncertainty is evaluated to 3.7% [55] where the dominant effect is due to the uncertainty on the measured bunch charges during calibration runs of the luminosity detectors [55]. The factors A_Z , C_Z and the luminosity for both channels are summarised in Table 5.11.

Table 5.11: Summary of the factors A_Z , C_Z and the luminosity for the $\tau_\mu\tau_h$ and the $\tau_e\tau_h$ channel. The given uncertainties on A_Z and C_Z are statistical ones due to the limited number of MC events. The luminosity uncertainty is of 3.7% as evaluated in [55].

Channel	A_Z	C_Z	$\mathcal{L}[\text{fb}^{-1}]$
$\tau_\mu\tau_h$	0.0976 ± 0.0002	0.1417 ± 0.0016	1.55 ± 0.06
$\tau_e\tau_h$	0.0687 ± 0.0002	0.0955 ± 0.0015	1.34 ± 0.05

If the geometrical acceptance, A_Z , is excluded from the cross section formula 5.8, the fiducial cross section is defined:

$$\sigma^{fid}(Z \rightarrow \tau\tau) \times BR(\tau \rightarrow \ell\nu\nu, \tau \rightarrow \tau_h\nu) = \frac{N_{obs} - N_{bkg}}{C_Z \cdot \mathcal{L}}. \quad (5.11)$$

The fiducial cross section is independent of the method used for extrapolating to the full phase space with the Monte Carlo, and is therefore less affected by theoretical uncertainties of the Monte Carlo model.

Table 5.12: The production cross section times branching ratio for the $Z \rightarrow \tau\tau$ process as measured in both channels. The fiducial cross sections also include the branching fraction of the τ to its decay products.

Final State	Fiducial cross section
$\tau_\mu\tau_h$	$20.0 \pm 0.3(\text{stat}) \pm 2.0(\text{syst}) \pm 0.7(\text{lumi})$ pb
$\tau_e\tau_h$	$15.9 \pm 0.4(\text{stat}) \pm 2.0(\text{syst}) \pm 0.6(\text{lumi})$ pb
Final State	Total cross section ($66 \text{ GeV} < m_{inv} < 116 \text{ GeV}$)
$\tau_\mu\tau_h$	$912.4 \pm 15.0(\text{stat}) \pm 94.0(\text{syst}) \pm 33.7(\text{lumi})$ pb
$\tau_e\tau_h$	$998.1 \pm 23.7(\text{stat}) \pm 130.8(\text{syst}) \pm 38.4(\text{lumi})$ pb

The measured number of data and Monte Carlo events is summarized in Table 5.10. Together with the numbers given in Table 5.11 and the branching ratios $BR(\tau \rightarrow \mu\nu\nu, \tau \rightarrow \tau_{had}\nu) = 0.225$ [20] and $BR(\tau \rightarrow e\nu\nu, \tau \rightarrow \tau_{had}\nu) = 0.231$ [20], the resulting fiducial cross sections and total cross sections times branching ratio are calculated

and summarized in Table 5.12. The systematic uncertainties and their detailed contributions are discussed in the following section.

5.9 Systematic Uncertainties

The evaluation of the systematic uncertainties is a relevant part of the measurements as the precision of the cross section measurements is limited mainly by those systematics. The BR of the tau lepton are measured very precisely to be in the order of 0.3% [20]. While the number of measured data events includes statistical uncertainties only, the factors C_Z , A_Z and also the background estimation is dominated by systematic uncertainties. The different sources of uncertainties and the methods of their evaluation are described in the following sections.

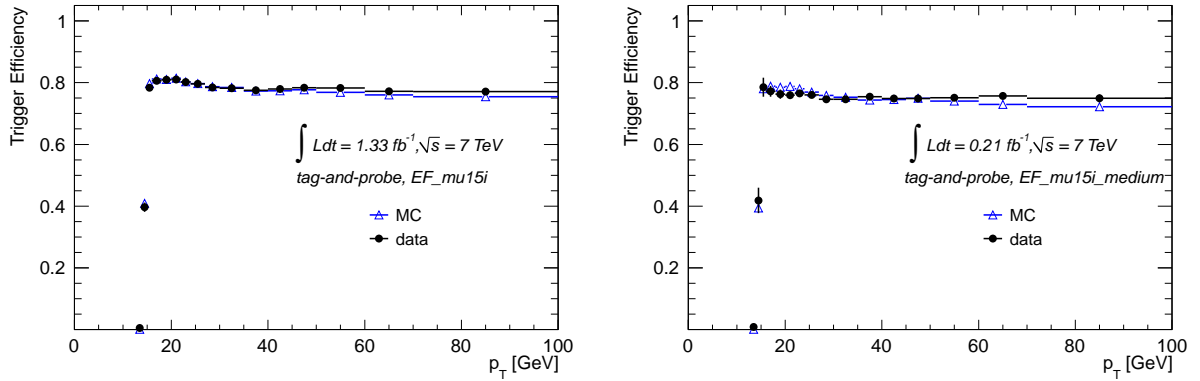
5.9.1 Trigger Efficiencies and Scale Factors

The trigger efficiencies of the isolated muon triggers, used in the $\mu\tau_h$ channel, are measured in $Z \rightarrow \mu\mu$ events with regard to offline reconstructed and isolated muons as a function of η and ϕ . This is performed by selecting one tag muon identified with the offline isolation criteria of the analysis and measuring the trigger efficiency of the second probe muon. Differences between Monte Carlo samples and data are corrected by scale factors. Systematic uncertainties on the efficiencies and the correction factors are evaluated considering the statistical uncertainties of the data and MC samples used. The obtained relative uncertainty is 0.01 and the effect on the finally measured cross section is evaluated [83]. The trigger efficiencies of the isolated muon triggers, applied in this analysis, are shown in Figure 5.21 in dependence of p_T of the muon for data compared to MC.

For the combined electron-tau trigger in the $e\tau_h$ channel, the efficiencies of the two parts are evaluated independently of each other since they are assumed to be uncorrelated. The electron trigger efficiency is evaluated in dependence of E_T and η of the electron, using a tag-and-probe method on $W \rightarrow e\nu$ events. This is done by using missing energy triggers and with respect to tight identified isolated electrons. From the differences between data and MC, scale factors in dependence of E_T and η of the electron are calculated and applied to the MC samples. They are shown in Figure 5.22(a). Systematic uncertainties are evaluated by varying the isolation cone and the isolation threshold of the probe electron and obtaining the RMS of the various resulting scale factors.

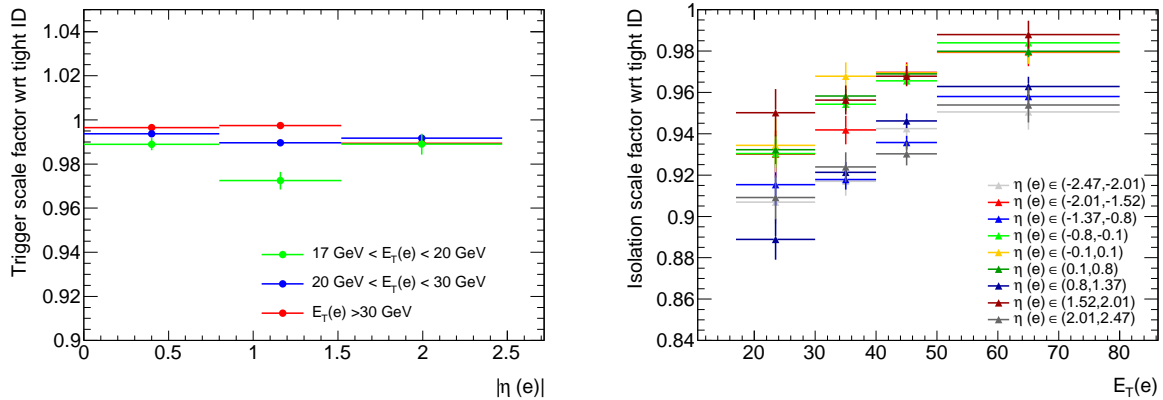
For the tau part, the tau trigger efficiency in dependence of p_T is measured with respect to offline tau candidates passing all identification criteria and directly applied as a p_T dependent weight on the Monte Carlo. The efficiencies are measured using a data selection obtained by triggering on one lepton and applying a similar selection as described in Section 5.5.

The exact procedure of evaluating the tau trigger scale factors and their systematic uncertainties is described in detail in Appendix C. The electron and tau part are assumed to be uncorrelated and hence the effect of the systematic uncertainties on the measured cross sections are also evaluated independently of each other and summarized in Table 5.15.



(a) Muon trigger efficiencies for EF_mu15i trigger. (b) Muon trigger efficiencies for EF_mu15i_med trigger.

Figure 5.21: Muon trigger efficiencies for the isolated muon triggers in dependence of p_T of the muon for data compared to MC [83]. The differences are applied as scale factors (SF) to the MC samples and systematic uncertainties are propagated to the cross section measurement.



(a) Electron trigger SF for EF_e15_medium trigger. (b) Electron isolation scale factors with regard to tight identified electrons.

Figure 5.22: Electron trigger scale factors (a) in dependence of E_T and η of the electron [83]. Isolation scale factors (b) for the offline electron isolation in dependence of E_T and η of the electron [83]. Systematic uncertainties on these scale factors are propagated to the cross section measurement.

5.9.2 Reconstruction, Identification and Isolation Efficiencies of the Muons and Electrons

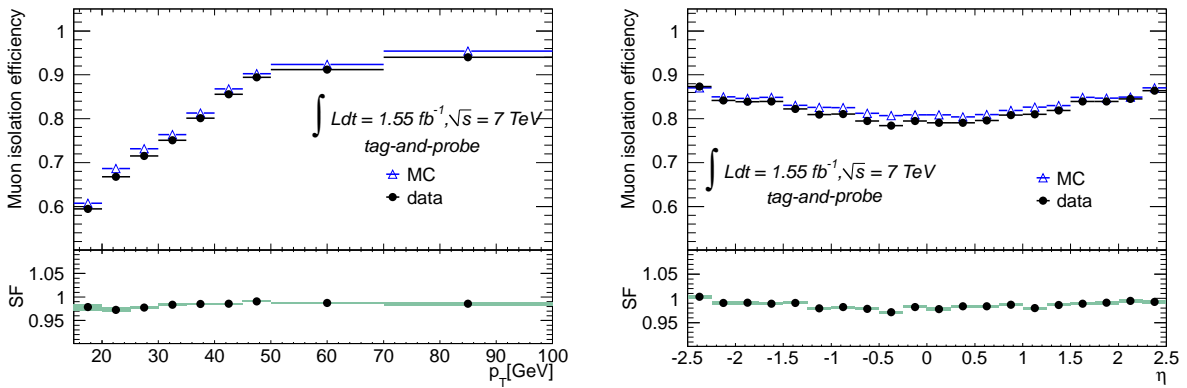
The reconstruction, identification and isolation cuts on the muons and electrons also have a certain efficiency which is measured in data using tag-and-probe methods. The Monte Carlo is corrected for differences from data using p_T and η dependent correction factors. For the muons, the reconstruction and identification efficiencies are measured using $Z \rightarrow \mu\mu$ events. The main contribution to the systematic uncertainty here is due to background fluctuation in the tag-and-probe method and is assigned to be 0.002 [73]. $W \rightarrow e\nu$, $Z \rightarrow ee$ and $J/\psi \rightarrow ee$ events [74] are used to obtain the electron reconstruction

and identification efficiencies. The systematic uncertainties mainly come from limited statistics of the tag-and-probe data sample and the background estimation. They depend on the method and E_T of the electron and vary between 0.005 and 0.165 [74].

The isolation efficiencies are evaluated for the special dedicated isolation requirements of this analysis, using $Z \rightarrow ee$ events for the electron isolation and $Z \rightarrow \mu\mu$ events for the muon isolation. The electron isolation scale factors with their statistical uncertainties in dependence of E_T and η of the electron are shown in Figure 5.22(b). The systematic uncertainty is obtained by varying the isolation requirement of the probe electron.

The muon isolation efficiencies and scale factors dependent on p_T and η can be seen in Figure 5.23. The systematic uncertainties are evaluated by varying the isolation cut on the selected probe muon and is found to be 0.013, independent of p_T and η of the muon. The trigger, reconstruction, identification and isolation efficiencies of the muons and electrons are factorized to a overall muon and electron efficiency.

The systematic uncertainties on these efficiencies are obtained by calculating the squared sum of each contribution including the statistical uncertainty. The influence on the finally measured cross section is evaluated by varying up and down one standard deviation of these uncertainties and recalculating the cross section. The obtained values are given in Table 5.15.



(a) Muon isolation efficiency and SF in dependence of p_T .

(b) Muon isolation efficiency and SF in dependence of η .

Figure 5.23: Muon isolation efficiency and scale factors in dependence of p_T (a) and η (b) of the muon [83].

5.9.3 Identification Efficiency of the Hadronically Decaying Tau

The hadronic tau identification efficiency for various identification criteria is measured in data collected in 2011, as described in [77]. This is done by using a $Z \rightarrow \tau\tau$ event selection on the one hand and also a $W \rightarrow \tau\nu$ selection on the other hand. The latter one is an orthogonal selection to the one described here and therefore those results are used to obtain the tau identification efficiency and its uncertainty. The identification efficiency for the applied BDT tau identification is measured to be 0.63. The main contributions to

the systematic uncertainty is due to event generation, kinematics, underlying event model and pileup simulation of the MC samples. For the applied BDT identification a relative uncertainty of 0.05 is found [77], which is propagated to the finally measured cross section. The result can be found in Table 5.15.

Also relevant in the $e\tau_h$ channel is the probability that electrons are misidentified as hadronic taus. This was also measured in [77] using a tag and probe method on a $Z \rightarrow ee$ selection. Correction factors in dependence of η are calculated and applied to Monte Carlo events in case a generator level match of the identified tau to an electron is found. The main contribution to the systematic uncertainty here is due to variations in the electron identification method and is found to be in the order of 10% [77]. The influence on the measured cross section is, however, found to be negligible because of the low number of $Z \rightarrow ee$ background events in the signal region (compare last row of Table 5.7).

5.9.4 Background Estimation

The main contribution to the background are multijet events, as can be seen in Table 5.10. Uncertainties on the multijet estimation arise from the statistical uncertainty of data and subtracted Monte Carlo events in the control regions, as well as a variation of the OS/SS ratio with the cutflow and with the applied lepton isolation. The latter one is obtained by studying the ratio as a function of the lepton isolation and taking the maximum deviation from the average as systematic uncertainty. This is found to be 3% relative on the estimated multijet background. The OS/SS ratio in dependence of different cutflow steps is shown in Figure 5.24. In the $\mu\tau_h$ channel no significant variation is observed, while in the $e\tau_h$ channel a maximum variation of 4% is observed and considered as systematic contribution. Those effects are added in quadrature to get the total systematics on the multijet estimation.

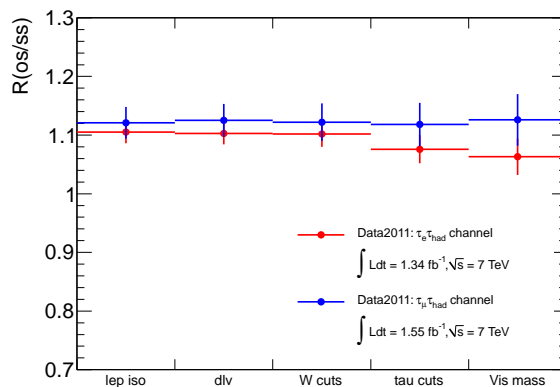


Figure 5.24: The ratio of events with oppositely charged lepton and tau candidate and similarly charged ones, $R_{OS/SS}$, as a function of the cutflow steps: lepton isolation (iso lep), dilepton veto (dlv), W cuts, tau cuts and visible mass window (Vis mass) for the $e\tau_h$ channel and the $\mu\tau_h$ channel [83].

Systematic effects on the MC samples subtracted in the control regions like the corrections, discussed previously, and cross section uncertainties are investigated and found to be small

in the order of 1%. These contributions are included in the resulting effect on the measured cross section given in Table 5.15.

A smaller background contribution comes from the W and $Z \rightarrow \mu\mu/ee$ backgrounds. Here the statistical uncertainties on the evaluation of the correction factors is used to obtain the systematics. Other contributions on the systematics of Monte Carlo samples are found to be negligible in comparison.

5.9.5 Geometrical and Kinematical Acceptance A_Z

The uncertainty on the geometrical and kinematical acceptance, A_Z as defined in Equation 5.9, is of theoretical nature due to the imprecise knowledge of the parton distribution functions (PDF) and the modeling of Z -boson production and parton showering at the LHC. The uncertainty originating from the PDF set is evaluated by considering the uncertainty of one PDF set and the deviations between different PDF sets. The latter one is obtained from the maximum deviation between the acceptance obtained from the default sample, described in Section 5.8, and the values obtained by reweighting this sample to the CTEQ6.6 and HERAPDF1.0 [84] PDF sets.

The uncertainty within one PDF set is evaluated by using the 44 PDF eigenvalues available for the CTEQ6.6 PDF set [34]. The variations are obtained by reweighting the default Pythia sample to the relevant CTEQ6.6 error eigenvector and comparing the result to the CTEQ6.6 central value applying the same reweighting procedure. The uncertainty is then calculated as:

$$\Delta A_Z = \frac{1}{2} \sqrt{\sum_i (A_Z^{i+} - A_Z^{i-})^2}, \quad (5.12)$$

with A_Z^{i+} and A_Z^{i-} being the up and down acceptance variations of the eigenvector, i . The uncertainties due to the modeling of W and Z boson production are estimated using MC@NLO interfaced with HERWIG for the parton shower, with the CTEQ6.6 PDF set and a lower bound on the invariant mass of 60 GeV. This is done by using the variation with respect to A_Z obtained using the default Pythia sample reweighted to the CTEQ6.6 PDF set central value and with an applied lower bound on the invariant mass of 60 GeV. The different contributions are summed up in quadrature to obtain the total theoretical uncertainty contribution from A_Z . The individual and total relative uncertainties on A_Z are summarized in Table 5.13.

Table 5.13: Relative systematic uncertainties of the different contributions to A_Z and total ones for the $e\tau_h$ channel and the $\mu\tau_h$ channel [83].

Source of uncertainty	$\mu\tau_h$ channel	$e\tau_h$ channel
CTEQ6.6 PDF eigenvector set	0.9%	1.2%
Different PDF sets	2.2%	1.7%
Model dependence	2.1%	2.7%
Total uncertainty	3.1%	3.4%

In the default sample, PHOTOS is used to model the QED radiation. Here, the accuracy of simulations in complete multi-photon final states is found to be in the order of 0.1% [67] and therefore has a negligible contribution compared to the uncertainties arising from the PDF sets.

5.9.6 Energy Scale Uncertainty

The uncertainties on the energy scales of the electrons, tau candidates and E_T^{miss} , have an important influence on the measured cross section. This arises in the factor C_Z as the amount of events rejected mainly by the p_T and E_T cuts on those objects can vary significantly with varying energy scales.

The main contributions to the tau energy scale uncertainty are due to variations in the hadronic shower model and to deviations between the reconstructed tau kinematics and the true tau kinematics, which is obtained from MC simulations [77]. The uncertainties depend on E_T and η of the tau candidate and are evaluated separately for one-prong taus and multi-prong taus. The obtained uncertainties are summarized in Table 5.14.

Table 5.14: Tau energy scale uncertainties in dependence of E_T and η of the tau candidate [77]. They are used to scale the tau energy both up and down in MC.

Relative uncertainty Detector Region $ \eta $	One-prong tau candidates			Multi-prong tau candidates		
	< 1.3	$[1.3, 1.6]$	> 1.6	< 1.3	$[1.3, 1.6]$	> 1.6
$15 < E_T < 20$ GeV	5.5%	5.0%	4.5%	6.5%	9.5%	6.5%
$20 < E_T < 30$ GeV	4.5%	5.0%	4.5%	6.5%	5.5%	5.5%
$E_T > 30$ GeV	3.5%	5.0%	4.5%	–	–	–
$30 < E_T < 40$ GeV	–	–	–	5.5%	5.5%	5.5%
$E_T > 40$ GeV	–	–	–	4.5%	5.0%	5.0%

The electron energy scale uncertainty is evaluated to be within 1% - 2% with a slight dependence in E_T and η of the electron. Here the main contribution comes from imperfect knowledge of the amount of detector material in front of the electromagnetic calorimeter [74]. The jet energy scale in ATLAS is measured to be in the order of 3% [85], also dependent on E_T and η of the jet.

The effect on the measured cross section is studied by varying up and down the energy scale of these objects simultaneously by one standard deviation. The resulting shift of C_Z as well as of the number of background events is obtained, whereas the latter one has a minor effect. The energy scale on E_T^{miss} is varied by shifting up or down the reconstructed energy of all calorimeter clusters and recalculating E_T^{miss} afterwards. As the same clusters are partly also responsible for reconstructing the electrons and hadronic tau candidates, a certain correlation appears in the energy scale systematics between them. Therefore, the simultaneous energy scaling of these objects is not propagated to the E_T^{miss} variations in order to avoid double counting.

The reconstructed momentum of the muons is mainly based on the inner detector and the muon spectrometer measurements and relies on the calorimeter clusters only weakly.

Hence, it can be varied independently of the energy scale of E_T^{miss} and the correlation can be neglected. The energy scale uncertainties due to muons are negligible compared to those originating from the hadronic tau candidates. The values are summarized in Table 5.15.

5.9.7 Further Systematic Uncertainties

Several additional systematic sources are also studied, but are found to have a minor effect on the finally measured cross section. Those are uncertainties due to object quality requirements and effects of local readout problems of the calorimeter [83]. The energy resolution of the muons and electrons has only effects of less than one percent on C_Z and the background estimations. Uncertainties originating from misidentification of the charge of the electrons are in the low percentage region and are described correctly by the MC simulations [74]. Also the effect of theoretical uncertainties on the cross section of the Monte Carlo background processes is evaluated. An uncertainty of 5% is assigned to the NNLO cross sections of the W , Z and Diboson samples [86], while the $t\bar{t}$ cross section is varied +7.0%/-9.6% [87]. The relative effect on the measured cross section is found to be only 0.1% in the $\mu\tau_h$ channel and 0.2% in the $e\tau_h$ channel. The uncertainty on the total integrated luminosity, measured by the luminosity group of ATLAS, amounts to 3.7 % as described in [55].

5.9.8 Summary of Systematic Uncertainties

The major uncertainty on the measured cross section, defined in 5.8, arises from the factor C_Z where the effects on the $Z \rightarrow \tau\tau$ signal Monte Carlo, previously described, are relevant. Theoretical uncertainties on C_Z , like the theoretical cross section on the signal Monte Carlo process, do cancel out here as they appear in the numerator and in the denominator. As the electroweak and $t\bar{t}$ processes are subtracted in the multijet control regions as previously described, correlations between uncertainties on them and the multijet estimations arise and are taken into account.

The main contributions come from the energy scale uncertainties (where the uncertainty on the hadronic tau energy scale is the dominant one), the identification efficiencies of the electrons and tau candidates, and the tau trigger efficiency in the $e\tau_h$ channel. The different sources of systematic uncertainties and their relative contribution to the measured cross section in the two analysis channels are summarized in Table 5.15.

5.10 Combination of the Channels and Results

After obtaining the final results of the two analysis channels summarized in Table 5.12, the aim is to combine these results to one measured cross section for $Z \rightarrow \tau\tau$ considering the uncertainties on the measurements and their correlations.

The combination was performed using the Best Linear Unbiased Estimate (BLUE) method, as described in [88, 89]. The covariance matrix of the statistical and systematic uncertainties of the individual analysis channels is constructed, where correlations between the uncertainties of the channels are considered. The best estimate of the combined cross section is obtained by a linear combination of the individual measurements. The last

Table 5.15: Statistical and systematic uncertainties in % relative to the total cross section measurement. The muon (electron) efficiency term includes the muon (electron) trigger, reconstruction, identification and isolation uncertainties, as described in the text. The last column indicates whether a given systematic uncertainty is treated as correlated (\checkmark) or uncorrelated ($-$) among the two analysis channels when combining the results, as described in Section 5.10.

Systematic uncertainty	$\delta\sigma/\sigma$ (%) $\mu\tau_h$	$\delta\sigma/\sigma$ (%) $e\tau_h$	Correlation
Muon efficiency	1.7	-	-
Electron efficiency	-	5.0	-
Muon resolution	< 0.05	-	-
Electron resolution	-	0.1	-
τ ID efficiency	5.2	5.2	\checkmark
$e \rightarrow \tau$ misidentification rate	-	0.2	-
Energy scale	8.2	9.3	\checkmark
τ trigger efficiency	-	4.7	-
k_W normalization factor	<0.05	<0.05	-
k_Z normalization factor	<0.05	<0.05	-
Multijet estimation	0.8	1.3	\checkmark
Theoretical cross section background	0.1	0.2	\checkmark
Monte Carlo statistics	1.2	1.4	-
A_Z uncertainties	3.1	3.4	\checkmark
Total systematic unc.	10.4	13.2	
Luminosity uncertainty	3.7	3.7	\checkmark
Statistical uncertainty	1.6	2.4	-

column of Table 5.15 indicates if one source of uncertainty is correlated between the two analysis channels or not. Uncertainty sources due to objects used in both analysis channels, like the tau candidates, are assumed to be fully correlated, while those affecting only one channel are assumed not to be correlated.

The largest systematic uncertainties are also treated as correlated (energy scale, tau identification efficiency, acceptance A_Z , luminosity) between the channels. In case of large positive correlations between the inputs, large negative weights for the input data can occur in the BLUE method. In this case, the resulting combination can be very sensitive to the correlation assumed [88]. It cannot be excluded that the correlation between the large uncertainties, like the energy scale, is less than the assumed 100% correlation. The reason is that for example the energy scale on the electrons has a small contribution there, but appears in the $e\tau_h$ channel only. Due to the definition of the E_T^{miss} , the energy scale uncertainty can not be evaluated individually for the objects, but only simultaneously as described in Section 5.9.6.

To avoid the sensitivity of the combination on the exact correlations, the energy scale systematic uncertainties is excluded from the combination with the BLUE method. Instead it

is added to the final combined uncertainty using gaussian error propagation and considering the weights, obtained by BLUE without the energy scale uncertainty. With this procedure the resulting total systematic uncertainty is slightly larger, as the energy scale contribution is not included in the minimization of BLUE. The resulting value obtained is

$$\sigma(Z \rightarrow \tau\tau, 66 < m_{\text{inv}} < 116 \text{ GeV}) = 914.4 \pm 14.6(\text{stat}) \pm 95.1(\text{syst}) \pm 33.8(\text{lumi}) \text{ pb.} \quad (5.13)$$

The corresponding weights of the two channels are 0.976 for the $\mu\tau_h$ channel and 0.024 for the $e\tau_h$ channel.

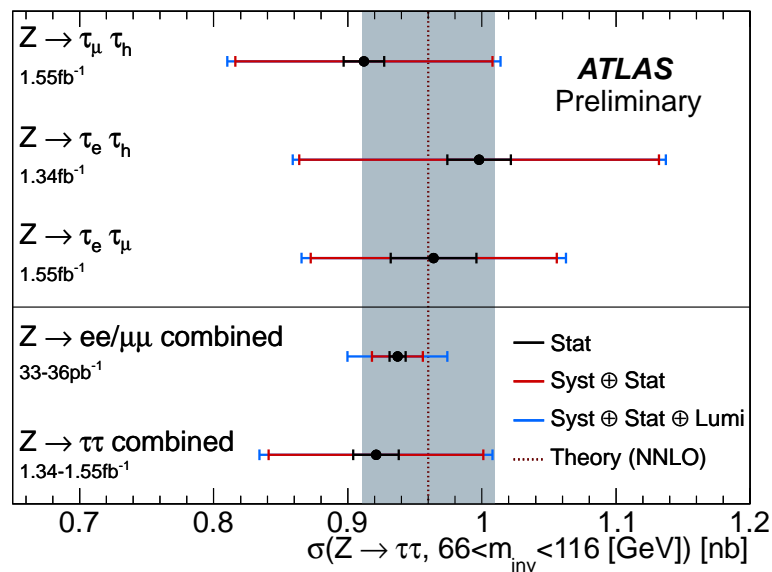


Figure 5.25: The figure shows the cross sections as measured in the individual channels and the combined value [65]. Also the combined measurements of the $Z \rightarrow \tau\tau \rightarrow ee + 4\nu$ and $Z \rightarrow \tau\tau \rightarrow \mu\mu + 4\nu$ final states are shown. The blue band represents the uncertainty on the NNLO cross section prediction [7].

This result is in agreement with theoretical predictions of the $Z \rightarrow \tau\tau$ cross section of 964 ± 48 pb [7, 68–70] within one standard deviation. Also it agrees with previous measurements of the ATLAS and CMS experiment [5, 6].

The corresponding analysis done for the ATLAS collaboration includes also the channel, where one tau decays into an electron and the other into a muon ($e\mu$ channel), as described in [65]. The measured cross section for the $e\mu$ channel is

$$\sigma(Z \rightarrow \tau\tau \rightarrow e\nu\nu, \mu\nu\nu) = 964.4 \pm 51.1(\text{stat}) \pm 81.0(\text{syst}) \pm 37.7(\text{lumi}) \text{ pb.} \quad (5.14)$$

In case the result of this channel is also included in the combination done with the BLUE method, the final cross section combines to

$$\sigma(Z \rightarrow \tau\tau, 66 < m_{\text{inv}} < 116 \text{ GeV}) = 920.6 \pm 16.7(\text{stat}) \pm 78.1(\text{syst}) \pm 34.0(\text{lumi}) \text{ pb.} \quad (5.15)$$

The same procedure for the uncertainty evaluation is applied as here. The corresponding weights are 0.753 for the $\mu\tau_h$ channel and -0.120 for the $e\tau_h$ channel and 0.370 for the $e\mu$ channel [65]. This value combined from the three decay channels is also given in [65] and Figure 5.25 shows it together with the results of the individual channels and combined measurements of the $Z \rightarrow \tau\tau \rightarrow ee + 4\nu$ and $Z \rightarrow \tau\tau \rightarrow \mu\mu + 4\nu$ cross section, as well as the theoretical prediction as blue band.

5.11 The $Z \rightarrow \tau\tau$ Cross Section Measurement in the LHC Physics Context

The LHC and its detectors are designed to cover a wide physics program in the scope of new discoveries as well as precision measurements at $\sqrt{s} = 7\text{--}14$ TeV. In 2012 a new resonance at 126 GeV has been discovered by both experiments, ATLAS and CMS, in the decay channels $X \rightarrow \gamma\gamma$, $X \rightarrow WW$ and $X \rightarrow ZZ$ [1, 2]. At the time of writing it is compatible with the Higgs boson, but more detailed measurements are needed for a confirmation. Therefore, also the decay channel $X \rightarrow \tau\tau \rightarrow \tau_\ell\tau_h$ needs to be studied to confirm the agreement with the expected branching ratios of Higgs decays, either in the Standard Model or its extensions. The process $Z \rightarrow \tau\tau \rightarrow \tau_\ell\tau_h$ is the most important background in this channel and therefore a precise measurement of this process, as presented here, is crucial.

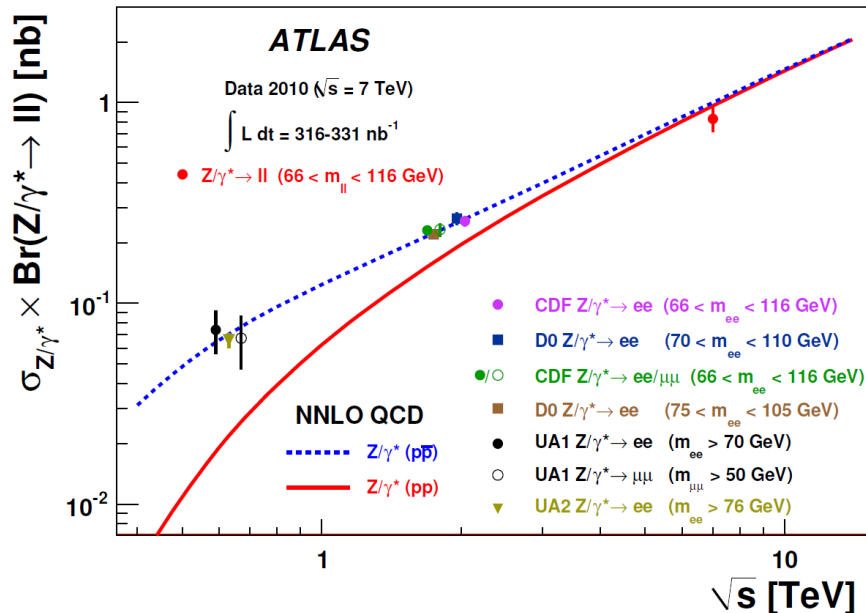


Figure 5.26: Z production cross section in dependence of the center of mass energy [90]. Measurements of $p\text{-}\bar{p}$ experiments as well as the ATLAS measurement are shown and compared to theoretical predictions from NNLO calculations.

Furthermore, the LHC runs at the highest center-of-mass energies which have been reached at a collider so far. The confirmation of the Standard Model at this energies like the measurement of the $Z \rightarrow \tau\tau$ cross section and also confirmation of lepton universality is relevant.

Figure 5.26 shows the measured Z/γ^* production cross section for various p- \bar{p} experiments and the $Z/\gamma^* \rightarrow \ell\ell$ (where ℓ stands for muon or electron) measurement in p-p collisions from ATLAS [90]. They are overlayed with predictions from NNLO calculations, which agree with the experimental measurements up to the $\sqrt{s} = 7$ TeV of ATLAS. Remarkable are the strong dependence of the cross sections on the center of mass energy and that the difference between p-p and p- \bar{p} collisions has already nearly disappeared at $\sqrt{s} = 7$ TeV. A good agreement between the measured $Z/\gamma^* \rightarrow \ell\ell$ and $Z/\gamma^* \rightarrow \tau\tau$ cross sections has also been confirmed and is visible in Figure 5.25.

Table 5.16: List of Monte Carlo samples for Z +jets production. The generated mass of the Z boson is $M_Z > 40$ GeV. The samples are generated with ALPGEN [35] and split per number of initial extra partons (NpX, X=0, ..., 5). A minimum parton p_T cut at 20 GeV is applied.

Process	Dataset Number	LO Cross Section \times NNLO-factor in pb [7]	Events
$Z \rightarrow \tau\tau (m_{\ell\ell} > 40 \text{ GeV}) + \text{Np0}$	107670	668.40×1.25	6608784
$Z \rightarrow \tau\tau (m_{\ell\ell} > 40 \text{ GeV}) + \text{Np1}$	107671	134.81×1.25	1327672
$Z \rightarrow \tau\tau (m_{\ell\ell} > 40 \text{ GeV}) + \text{Np2}$	107672	40.36×1.25	403864
$Z \rightarrow \tau\tau (m_{\ell\ell} > 40 \text{ GeV}) + \text{Np3}$	107673	11.25×1.25	109947
$Z \rightarrow \tau\tau (m_{\ell\ell} > 40 \text{ GeV}) + \text{Np4}$	107674	2.79×1.25	29977
$Z \rightarrow \tau\tau (m_{\ell\ell} > 40 \text{ GeV}) + \text{Np5}$	107675	0.77×1.25	9990
$Z \rightarrow ee (m_{\ell\ell} > 40 \text{ GeV}) + \text{Np0}$	107650	668.32×1.25	6612265
$Z \rightarrow ee (m_{\ell\ell} > 40 \text{ GeV}) + \text{Np1}$	107651	134.36×1.25	1333745
$Z \rightarrow ee (m_{\ell\ell} > 40 \text{ GeV}) + \text{Np2}$	107652	40.54×1.25	404873
$Z \rightarrow ee (m_{\ell\ell} > 40 \text{ GeV}) + \text{Np3}$	107653	11.16×1.25	109942
$Z \rightarrow ee (m_{\ell\ell} > 40 \text{ GeV}) + \text{Np4}$	107654	2.88×1.25	29992
$Z \rightarrow ee (m_{\ell\ell} > 40 \text{ GeV}) + \text{Np5}$	107655	0.83×1.25	8992
$Z \rightarrow \mu\mu (m_{\ell\ell} > 40 \text{ GeV}) + \text{Np0}$	107660	668.68×1.25	6619010
$Z \rightarrow \mu\mu (m_{\ell\ell} > 40 \text{ GeV}) + \text{Np1}$	107661	134.14×1.25	1334723
$Z \rightarrow \mu\mu (m_{\ell\ell} > 40 \text{ GeV}) + \text{Np2}$	107662	40.33×1.25	403886
$Z \rightarrow \mu\mu (m_{\ell\ell} > 40 \text{ GeV}) + \text{Np3}$	107663	11.19×1.25	109954
$Z \rightarrow \mu\mu (m_{\ell\ell} > 40 \text{ GeV}) + \text{Np4}$	107664	2.75×1.25	29978
$Z \rightarrow \mu\mu (m_{\ell\ell} > 40 \text{ GeV}) + \text{Np5}$	107665	0.77×1.25	9993

Table 5.17: List of Monte Carlo samples for W +jets production. The samples are generated with ALPGEN and split per number of initial extra partons (NpX, X=0, ..., 5). A minimum parton p_T cut at 20 GeV is applied.

Process	Dataset Number	LO Cross Section \times NNLO-factor in pb [7]	Events
$W \rightarrow \tau\nu + \text{Np0}$	107700	6918.60×1.20	3259564
$W \rightarrow \tau\nu + \text{Np1}$	107701	1303.20×1.20	2496467
$W \rightarrow \tau\nu + \text{Np2}$	107702	378.18×1.20	3764804
$W \rightarrow \tau\nu + \text{Np3}$	107703	101.51×1.20	1008514
$W \rightarrow \tau\nu + \text{Np4}$	107704	25.64×1.20	248864
$W \rightarrow \tau\nu + \text{Np5}$	107705	7.04×1.20	64950
$W \rightarrow e\nu + \text{Np0}$	107680	6921.60×1.20	3455037
$W \rightarrow e\nu + \text{Np1}$	107681	1304.30×1.20	2499513
$W \rightarrow e\nu + \text{Np2}$	107682	378.29×1.20	3768265
$W \rightarrow e\nu + \text{Np3}$	107683	101.43×1.20	1009641
$W \rightarrow e\nu + \text{Np4}$	107684	25.87×1.20	249869
$W \rightarrow e\nu + \text{Np5}$	107685	7.00×1.20	69953
$W \rightarrow \mu\nu + \text{Np0}$	107690	6919.60×1.20	3466523
$W \rightarrow \mu\nu + \text{Np1}$	107691	1304.20×1.20	2499513
$W \rightarrow \mu\nu + \text{Np2}$	107692	377.83×1.20	3768893
$W \rightarrow \mu\nu + \text{Np3}$	107693	101.88×1.20	1009589
$W \rightarrow \mu\nu + \text{Np4}$	107694	25.75×1.20	254879
$W \rightarrow \mu\nu + \text{Np5}$	107695	6.92×1.20	69958

Table 5.18: List of Monte Carlo samples for Z +jets production. The generated mass of the Z boson is $10 \text{ GeV} < M_Z < 40 \text{ GeV}$. The samples are generated with ALPGEN and split per number of initial extra partons (NpX, X=0, ..., 5). A minimum parton p_T cut at 20 GeV is applied.

Process	Dataset Number	LO Cross Section \times NNLO-factor pb [7]	Events
$\gamma^*/Z \rightarrow \tau\tau$ ($10 \text{ GeV} < m_{\ell\ell} < 40 \text{ GeV}$) + Np0	116270	3055.1×1.25	959877
$\gamma^*/Z \rightarrow \tau\tau$ ($10 \text{ GeV} < m_{\ell\ell} < 40 \text{ GeV}$) + Np1	116271	84.93×1.25	296945
$\gamma^*/Z \rightarrow \tau\tau$ ($10 \text{ GeV} < m_{\ell\ell} < 40 \text{ GeV}$) + Np2	116272	41.47×1.25	498804
$\gamma^*/Z \rightarrow \tau\tau$ ($10 \text{ GeV} < m_{\ell\ell} < 40 \text{ GeV}$) + Np3	116273	8.36×1.25	149953
$\gamma^*/Z \rightarrow \tau\tau$ ($10 \text{ GeV} < m_{\ell\ell} < 40 \text{ GeV}$) + Np4	116274	1.85×1.25	39980
$\gamma^*/Z \rightarrow \tau\tau$ ($10 \text{ GeV} < m_{\ell\ell} < 40 \text{ GeV}$) + Np5	116275	0.46×1.25	9995
$\gamma^*/Z \rightarrow ee$ ($10 \text{ GeV} < m_{\ell\ell} < 40 \text{ GeV}$) + Np0	116250	3055.2×1.25	999859
$\gamma^*/Z \rightarrow ee$ ($10 \text{ GeV} < m_{\ell\ell} < 40 \text{ GeV}$) + Np1	116251	84.92×1.25	299940
$\gamma^*/Z \rightarrow ee$ ($10 \text{ GeV} < m_{\ell\ell} < 40 \text{ GeV}$) + Np2	116252	41.41×1.25	499880
$\gamma^*/Z \rightarrow ee$ ($10 \text{ GeV} < m_{\ell\ell} < 40 \text{ GeV}$) + Np3	116253	8.38×1.25	149940
$\gamma^*/Z \rightarrow ee$ ($10 \text{ GeV} < m_{\ell\ell} < 40 \text{ GeV}$) + Np4	116254	1.85×1.25	39973
$\gamma^*/Z \rightarrow ee$ ($10 \text{ GeV} < m_{\ell\ell} < 40 \text{ GeV}$) + Np5	116255	0.46×1.25	9995
$\gamma^*/Z \rightarrow \mu\mu$ ($10 \text{ GeV} < m_{\ell\ell} < 40 \text{ GeV}$) + Np0	116260	3054.9×1.25	999869
$\gamma^*/Z \rightarrow \mu\mu$ ($10 \text{ GeV} < m_{\ell\ell} < 40 \text{ GeV}$) + Np1	116261	84.87×1.25	299890
$\gamma^*/Z \rightarrow \mu\mu$ ($10 \text{ GeV} < m_{\ell\ell} < 40 \text{ GeV}$) + Np2	116262	41.45×1.25	499864
$\gamma^*/Z \rightarrow \mu\mu$ ($10 \text{ GeV} < m_{\ell\ell} < 40 \text{ GeV}$) + Np3	116263	8.38×1.25	149939
$\gamma^*/Z \rightarrow \mu\mu$ ($10 \text{ GeV} < m_{\ell\ell} < 40 \text{ GeV}$) + Np4	116264	1.85×1.25	39988
$\gamma^*/Z \rightarrow \mu\mu$ ($10 \text{ GeV} < m_{\ell\ell} < 40 \text{ GeV}$) + Np5	116265	0.46×1.25	9996

Table 5.19: List of Monte Carlo samples for the $t\bar{t}$ production, generated with MC@NLO 3 [38], and for the diboson production, generated with HERWIG 6.5 [36].

Process	Dataset Number	NLO Cross Section in pb [7]	Events
$t\bar{t}$ (no fully hadronic decays)	105200	90.15	14845714
WW	105985	17.02	2495756
ZZ	105986	5.54	249906
WZ	105987	1.26	249923

6 Summary and Outlook

Proton-proton collisions have been taking place at the LHC since March 2010. Data corresponding to more than 5fb^{-1} have been recorded by the ATLAS experiment at a center-of-mass energy of $\sqrt{s} = 7\text{ TeV}$ until 2011 and more than 18fb^{-1} at $\sqrt{s} = 8\text{ TeV}$ in 2012. With the first collision data the known Standard Model processes are measured with high accuracy. It is essential to understand their production and decay properties at LHC conditions for the discovery of new physics as they act as background to new physics signatures.

In this study, the production cross section measurement of the Standard Model Z boson in the decay channel $Z \rightarrow \tau\tau$ is carried out with collision data of 1.34fb^{-1} - 1.55fb^{-1} recorded by the ATLAS experiment at $\sqrt{s} = 7\text{ TeV}$. A selection of data events is applied in order to obtain a sample with high purity of $Z \rightarrow \tau\tau$ events. To describe the data accurately and to estimate several background sources to the $Z \rightarrow \tau\tau$ process, Monte Carlo simulations are used together with data driven background estimation methods.

The analysis is performed in the sub-channels $Z \rightarrow \tau\tau \rightarrow e\tau_h + 3\nu$ and $Z \rightarrow \tau\tau \rightarrow \mu\tau_h + 3\nu$. The measurement is done with a total of 2600 events in the $e\tau_h$ channel and 5184 events in the $\mu\tau_h$ channel after the final event selection. The results of the fiducial cross sections are determined to be:

$$\sigma_{e\tau_h}^{fid}(Z \rightarrow \tau\tau \rightarrow e\tau_h + 3\nu) = 15.9 \pm 0.4(\text{stat}) \pm 2.0(\text{syst}) \pm 0.6(\text{lumi}) \text{ pb} \quad (6.1)$$

in the $e\tau_h$ channel and

$$\sigma_{\mu\tau_h}^{fid}(Z \rightarrow \tau\tau \rightarrow \mu\tau_h + 3\nu) = 20.0 \pm 0.3(\text{stat}) \pm 2.0(\text{syst}) \pm 0.7(\text{lumi}) \text{ pb} \quad (6.2)$$

in the $\mu\tau_h$ channel. From these results, total inclusive cross sections are calculated using the geometrical and kinematical acceptance, A_Z , and the known branching ratios of the tau lepton. This leads to:

$$\sigma_{e\tau_h}^{inc}(Z \rightarrow \tau\tau) = 998.1 \pm 23.7(\text{stat}) \pm 130.8(\text{syst}) \pm 38.4(\text{lumi}) \text{ pb} \quad (6.3)$$

in the $e\tau_h$ channel and

$$\sigma_{\mu\tau_h}^{inc}(Z \rightarrow \tau\tau) = 912.4 \pm 15.0(\text{stat}) \pm 94.0(\text{syst}) \pm 33.7(\text{lumi}) \text{ pb} \quad (6.4)$$

in the $\mu\tau_h$ channel. These results are combined to one final result of the $Z \rightarrow \tau\tau$ inclusive cross section by taking the statistical and systematical uncertainties into account. The total inclusive cross section result obtained is:

$$\sigma_{tot}^{inc}(Z \rightarrow \tau\tau) = 914.4 \pm 14.6(\text{stat}) \pm 95.1(\text{syst}) \pm 33.8(\text{lumi}) \text{ pb.} \quad (6.5)$$

This is in agreement with theoretical predictions from NNLO calculations of $\sigma^{theory}(Z \rightarrow \tau\tau) = 964 \pm 48 \text{ pb}$ [7, 68–70] and also with measurements previously made by the ATLAS and CMS experiments at $\sqrt{s} = 7 \text{ TeV}$ [5, 6]. With the increased amount of data, the statistical uncertainties are reduced significantly compared to the previous measurements.

With the increased dataset of 2012 provided by the LHC, the ATLAS and CMS experiments were able to discover a new resonance at around 126 GeV in the decay channels $H \rightarrow \gamma\gamma$, $H \rightarrow ZZ \rightarrow 4\ell$ and $H \rightarrow WW \rightarrow e\nu\mu\nu$ [1, 2]. To confirm that its nature is the Higgs boson, this resonance is expected to be observed with an increased dataset also in the decay channel $H \rightarrow \tau\tau$. The $Z \rightarrow \tau\tau$ study presented here describes the most important irreducible background of that channel and thus a good understanding of this process at the LHC is crucial.

For the investigation of the properties of the new resonance and possible further new physics discoveries, the LHC is planned to be upgraded in several steps. Especially an increased instantaneous luminosity is challenging for the detector operation due to the increased particle flux and irradiation. Therefore, a careful testing of the operation performance of the ATLAS liquid-argon calorimeters is necessary, especially in the forward region due to the high particle flux there.

A testbeam study is performed to prove the correct operation of the electromagnetic and hadronic endcap calorimeters, EMEC and HEC, and the forward calorimeter, FCal, in the high particle fluxes of the upgraded LHC. The HV return currents of the EMEC module are analysed in dependence of the beam intensity. The results are compared to model predictions and simulations to extract the point of critical operation. Overall, the results are in agreement with the predictions, but the uncertainties are in the order of 50% and therefore rather large. The obtained values of the critical beam intensity are lower than the model predictions and the values measured for the critical HV current are higher than predicted, but within the uncertainties. The general behaviour of the HV current in dependence of the beam intensity above the critical intensity could be confirmed very well. The data of a following testbeam run are expected to provide results with reduced uncertainties and increased precision of the measured operation parameters compared to the predictions. Overall, the EMEC module is found to perform normally at the highest expected LHC luminosities. This will allow ATLAS to further explore new physics scenarios with nominal precision at the upgraded LHC collider.

Appendix A Gauge Invariance in Quantum Electrodynamics

A.1 Local gauge invariance

The modified Dirac lagrangian

$$\mathcal{L}_D = \bar{\psi}(i\gamma_\mu D^\mu - m)\psi. \quad (\text{A.1})$$

is invariant under local gauge transformation when the local phase transformation (2.6) is applied together with the transformation (2.8) of the field A^μ :

$$\begin{aligned} \mathcal{L}_D' &= \bar{\psi}'(i\gamma_\mu D^{\mu'} - m)\psi' = e^{-iQ\chi(\vec{r},t)}\bar{\psi}[i\gamma_\mu(\partial^\mu + ieQA^{\mu'}) - m]e^{iQ\chi(\vec{r},t)}\psi \\ &= e^{-iQ\chi(\vec{r},t)}\bar{\psi}e^{iQ\chi(\vec{r},t)}(i\gamma_\mu\partial^\mu\psi) + e^{-iQ\chi(\vec{r},t)}\bar{\psi}[i\gamma_\mu\partial^\mu e^{iQ\chi(\vec{r},t)}]\psi \\ &\quad - e^{-iQ\chi(\vec{r},t)}\bar{\psi}[\gamma_\mu eQ(A^\mu - \frac{1}{e}\partial^\mu\chi(\vec{r},t)) + m]e^{iQ\chi(\vec{r},t)}\psi. \end{aligned} \quad (\text{A.2})$$

The second term of the last expression (second row) equals to $-e^{-iQ\chi(\vec{r},t)}\bar{\psi}\gamma_\mu Q(\partial^\mu\chi(\vec{r},t))e^{iQ\chi(\vec{r},t)}\psi$ and cancels with the corresponding part of the third term (last row), following:

$$\begin{aligned} \mathcal{L}_D' &= e^{-iQ\chi(\vec{r},t)}\bar{\psi}e^{iQ\chi(\vec{r},t)}(i\gamma_\mu[\partial^\mu + ieQA^\mu] - m)\psi = e^{-iQ\chi(\vec{r},t)}\bar{\psi}e^{iQ\chi(\vec{r},t)}(i\gamma_\mu D^\mu - m)\psi \\ &= \bar{\psi}(i\gamma_\mu D^\mu - m)\psi = \mathcal{L}_D. \end{aligned} \quad (\text{A.3})$$

That means the physical system ψ is identical to the locally transformed ψ' , as the local phase transformation (2.6) is compensated by the gauge transformation (2.8) of the field A^μ .

A.2 Gauge invariance of the Maxwell-Equations

The Maxwell-equations 2.13 do not change under the gauge transformation (2.8), as shown here:

$$\begin{aligned} \square A^{\nu'} - \partial^\nu \partial_\mu A^{\mu'} &= \square(A^\nu - \partial^\nu\chi(\vec{r},t)) - \partial^\nu(\partial_\mu[A^\mu - \partial^\mu\chi(\vec{r},t)]) \\ &= \square A^\nu - \partial^\nu(\partial_\mu A^\mu) - \square\partial^\nu\chi(\vec{r},t) + \partial^\nu(\partial_\mu\partial^\mu\chi(\vec{r},t)) \\ &= \square A^\nu - \partial^\nu(\partial_\mu A^\mu) = j^\nu. \end{aligned} \quad (\text{A.4})$$

Appendix B Testbeam Results

The analysis and results of the calorimeter signal shapes at the testbeam study is not part of the work presented here, but is described here for completeness. The critical intensity and magnitude of the signal degradation are relevant points to study in terms to validate the endcap calorimeters for an operation in the high luminosity (HL) LHC phase. The calorimeter pulse readout and signal degradation are introduced in section 4.4. The ATLAS operation of the calorimeters should be always within the non-critical region of $r < 1$, while r is the relative ionization rate as introduced in Equation 4.1. For example, at an instantaneous ATLAS luminosity of $10^{34} \text{ cm}^{-2}\text{s}^{-1}$, the readout cells of the EMEC work at $r \leq 0.2$ [61]. In case of $r > 1$, the length and height of the pulse depends not only on the deposited energy (and known drift time) but also on r as $\propto r^{-1/4}$ in first order, which would reduce the precision of the energy measurement significantly. To understand the testbeam measurements, simulations for a LAr gap of the EMEC test module have been performed at different beam intensities. Figures B.1 and B.2 show the charge density and electric field over the gap as well as the induced current and signal amplitude over time for four beam intensities. An applied HV of 1.2kV and typical values for the positive ion mobility of $\mu_+ = 10^{-3} \text{ cm}^2/\text{Vs}$ and the recombination rate constant of $k_r = 10^{-5} \text{ cm}^3/\text{s}$ are used. Nevertheless, previous measurement show large uncertainties on this values of about a factor of 5 on μ_+ and a factor of 10 on k_r . The simulations are performed by dividing the 2mm LAr gap into 64 subgaps with all functions kept to be constant within a subgap. The electron and ion densities and therefore also the current density are set to zero as initial starting values and the further evolution in time is simulated in $\Delta t = 1.8 \text{ ns}$ time steps. More details of the simulations can be found in [61].

It can be clearly seen that with increasing beam intensity from $10^8 p/s$ to $10^9 p/s$, the charge density over the gap increases which leads to a strong asymmetric shift of the electric field, which would be completely constant in case $r \ll 1$. Further, the ideal triangular pulse becomes smoothed with a longer tail which finally results in a degraded signal shape with reduced amplitude and distorted tail as shown in Figure B.2. This behaviour could be well confirmed in the testbeam results. Figure B.3 shows normalised pulse shapes averaged over many bunches as measured in different beam intensity regions for the EMEC module as example. It increases from $< 25 p/\text{bunch}$ in the top left plot to a range of $5 \cdot 10^4 - 10 \cdot 10^4 p/\text{bunch}$ in the lower right plot. The deformation of the signal with shorter tails at higher intensities can be seen nicely. Due to the bipolar shaper, the area at the positive part of the pulse is the same as at the negative part. Given this, one can already imagine the reduction of the signal peak amplitude with increased intensity from these diagrams. Each plot also shows the shapes for 1.2kV as well as 0.6kV overlayed. No qualitative dependence of the pulse shapes on the applied voltage is visible. Only the absolute amplitude is reduced as expected from the simulations.

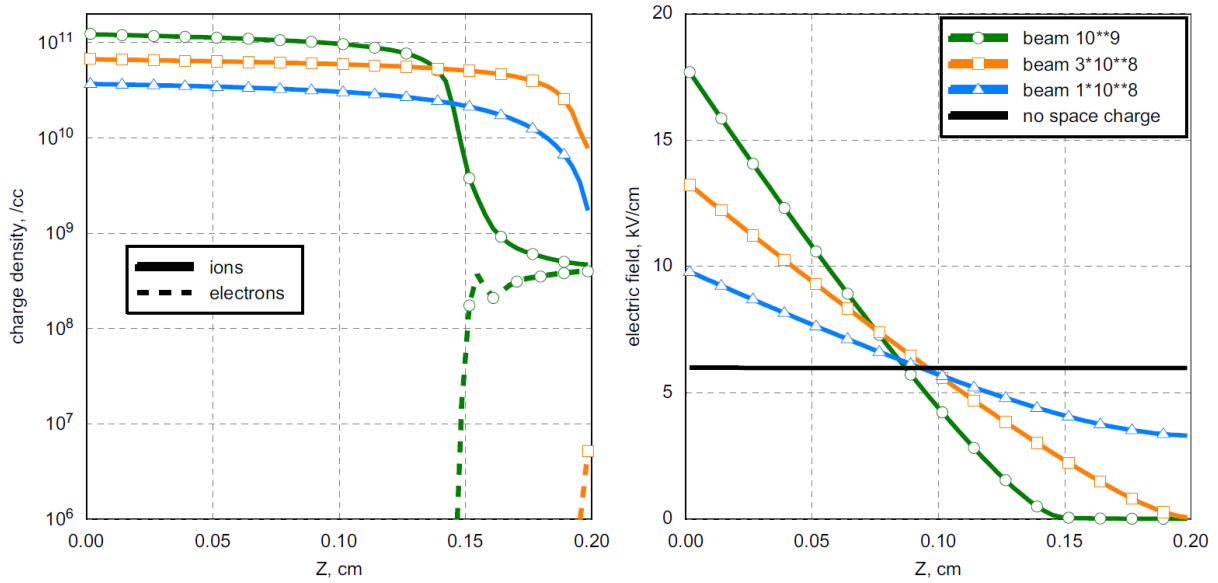


Figure B.1: Simulation of electron and ion density on the left and electric field on the right over the 2 mm LAr gap for different beam intensities. A high voltage of 1.2 kV, positive ion mobility of $\mu_+ = 10^{-3} \text{cm}^2/\text{Vs}$ and a recombination rate constant of $k_r = 10^{-5} \text{cm}^3/\text{s}$ have been assumed.

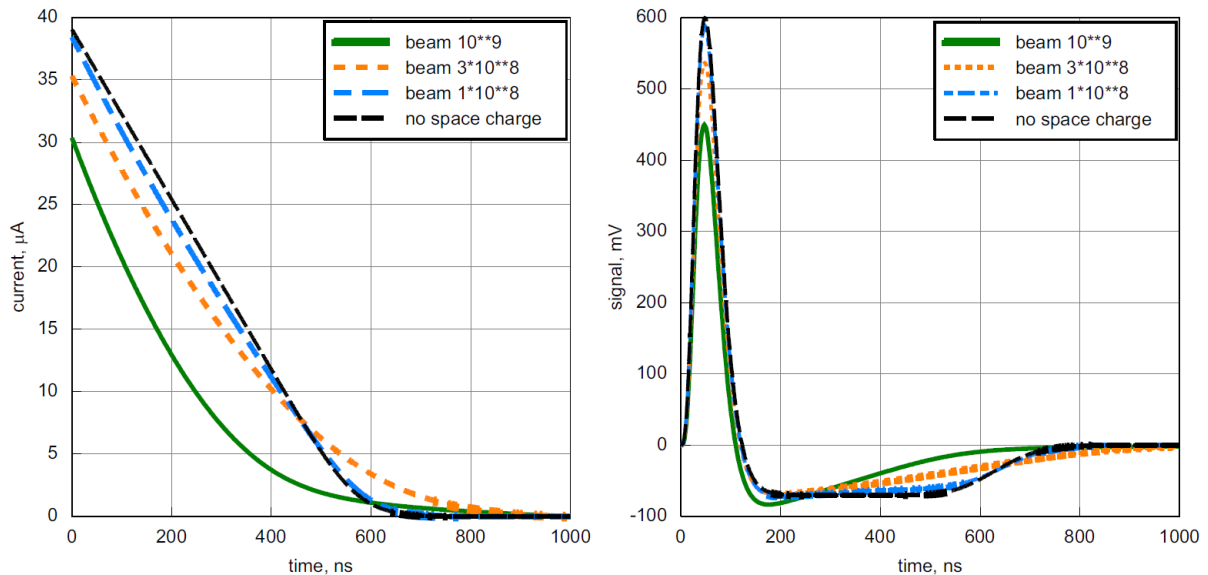


Figure B.2: Induced current on the left and pulse shape shaper on the right over time for different beam intensities as obtained from simulations. A high voltage of 1.2 kV, positive ion mobility of $\mu_+ = 10^{-3} \text{cm}^2/\text{Vs}$ and a recombination rate constant of $k_r = 10^{-5} \text{cm}^3/\text{s}$ have been assumed.

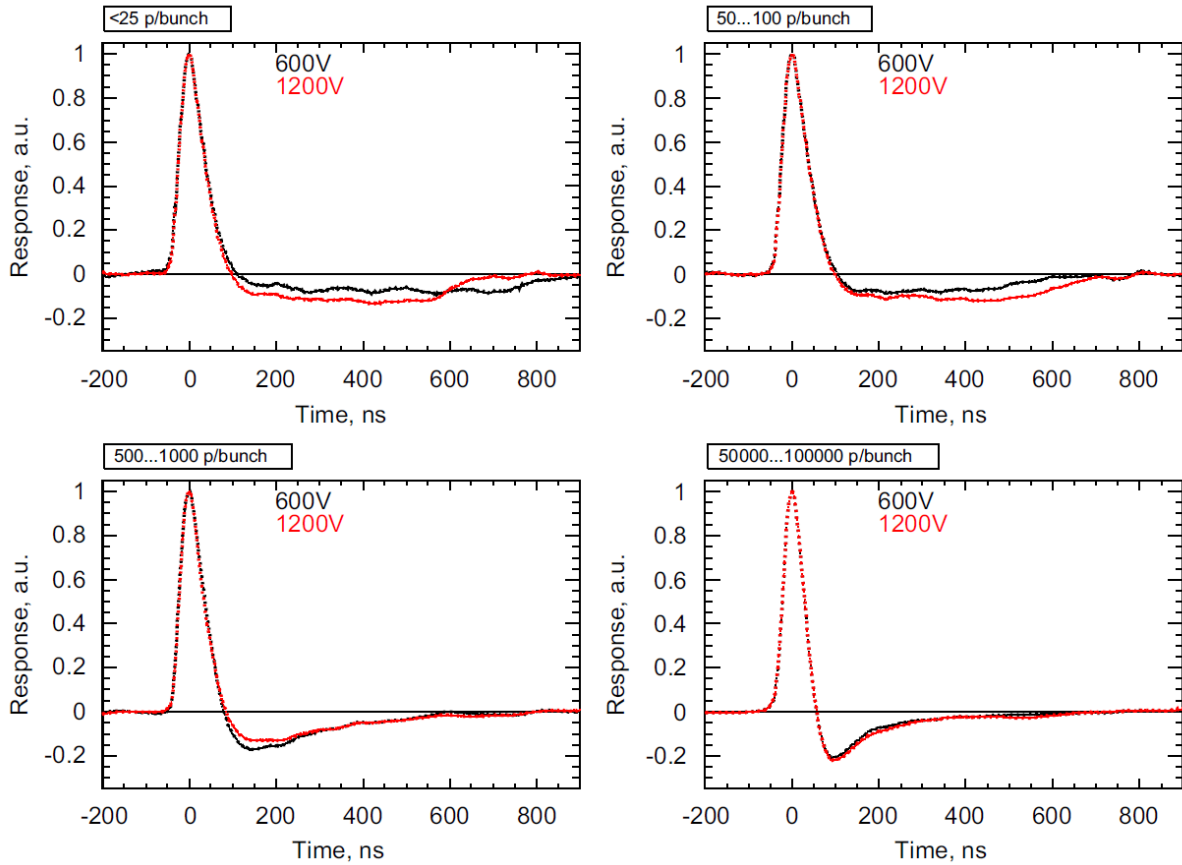


Figure B.3: Pulse shapes of the EMEC test module normalized to the beam intensity and averaged over many bunches for four different beam intensities. Top left: beam intensities of < 25 p/bunch, top right: 50-100 p/bunch, lower right: 500-1000 p/bunch, lower left: $5 \cdot 10^4 - 10 \cdot 10^4$ p/bunch.

To obtain the critical intensities and therefore the operation regime of the calorimeter test modules, the signal amplitude normalized to the bunch based beam intensity in dependence of the average beam intensity is studied. The results are summarized in Figure B.4 for all calorimeter test modules: the EMEC, the HEC, the FCal with the nominal $250 \mu\text{m}$ gaps and the FCal with the $100 \mu\text{m}$ LAr gaps.

The open dots show measured data points and the solid lines are fits to the data assuming a constant behaviour below the critical intensity and a drop like $\propto I^{-1/4}$ above. This holds for a simple model with small recombination rate constant of the ionized argon. At very low intensities, the calorimeter pulses are small, leading to much higher uncertainties in the signal reconstruction, while at very high intensities saturation effects in the readout electronics occur. Therefore, the data available for analysis is limited to the medium intensity range [61].

The obtained critical values are at $I_C = 1.6 \cdot 10^8$ p/s for the EMEC module, while the intensity corresponding to an LHC design luminosity of $10^{34} \text{ cm}^{-2} \text{ s}^{-1}$ is calculated to be $8.9 \cdot 10^7$ p/s. The EMEC of ATLAS is operated at 2 kV which would increase the critical

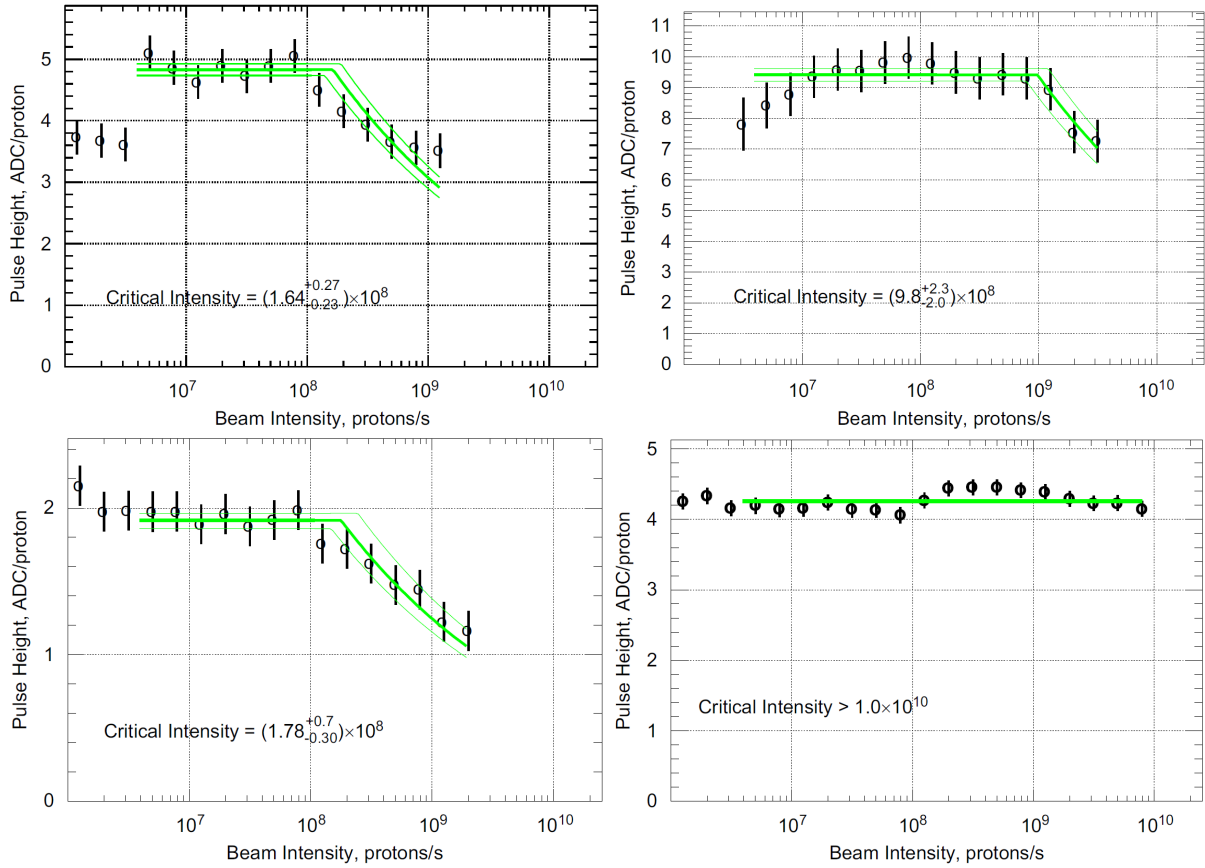


Figure B.4: Response of the calorimeter signal amplitude (ADC counts per proton) in dependence of the beam intensity [61]. Top left: EMEC module, bottom left: HEC module, top right: FCal module, bottom right: sFCal module. More details are given in the text.

intensity to $I_C \approx 4.6 \cdot 10^8 p/s$ [61]. For the HEC module, $I_C = 1.8 \cdot 10^8 p/s$, which would increase to $I_C = 4.0 \cdot 10^8 p/s$ for an operation at 1.8 kV in ATLAS, while the corresponding LHC design intensity is at $I_C = 4.8 \cdot 10^7 p/s$. The FCal test module with the 250 μm gaps operated at the nominal voltage of 250 V and shows $I_C = 9.8 \cdot 10^8 p/s$ with the corresponding LHC design intensity at $I_C = 6.7 \cdot 10^8 p/s$. The FCal test module with the reduced 100 μm gaps, in contrast, does not show a critical behaviour with the decreasing response up to the maximal analysed intensity of $10^{10} p/s$. This is expected for the design with the small gaps and shows that this module would be suited for an operation in the HL-LHC regime.

A summary of the obtained critical intensities of all modules relative to the calculated LHC design luminosity equivalent is given as follows:

- EMEC test module: $I_C \approx 5 \times$ LHC design luminosity equivalent
- HEC test module: $I_C \approx 8 \times$ LHC design luminosity equivalent
- FCal(250 μm gap): $I_C \approx 1.5 \times$ LHC design luminosity equivalent
- FCal(100 μm gap): $I_C > 10 \times$ LHC design luminosity equivalent.

These results show, that some modification of the forward calorimetry in ATLAS has to be performed in order to obtain still a good performance at HL-LHC conditions well above a luminosity of $10^{34} \text{ cm}^{-2} \text{ s}^{-1}$. The two considered options as described in Section 4.1 are a replacement of the current FCal with a new HL-FCal or the installation of an additional mini-FCal in front of the current FCal [58]. The possible design of a new FCal with reduced LAr gaps of $100 \mu\text{m}$ has been confirmed as suitable from the critical operation limit point of view. However, the FCal results have to be taken with care as only the two highest data points define the fitted breakpoint of the critical intensity (compare top right plot of Figure B.4).

The endcap calorimeters EMEC and HEC have shown uncritical operation up to few times the corresponding LHC design luminosity. When comparing the results of the pulse shape analysis of the EMEC with those of the HV current analysis, it can be seen that the obtained critical value is above the theoretical predictions and significantly above that one obtained in the HV current analysis. This discrepancy is not fully understood, but to a large extent covered by the rather big uncertainties assigned to the critical values here. These are in the order of 50% including fit uncertainties and systematics [61]. The analysis of new data of a following testbeam run aims for an increased precision with improved readout electronics. This will probably help to solve the issue with the remaining deviations between the HV current results and those of the pulse shape analysis in terms of the critical regime.

Appendix C Tau Trigger Weighting

In the $e\tau_h$ channel, the combined electron-tau trigger "EF_tau16_loose_e15_medium" is applied on data. For the MC simulations, only the electron part of that trigger could be used and the tau part is included by applying event weights, dependent on E_T of the tau candidate, as the full trigger information is not available in the used MC samples. To apply these weights, the trigger efficiency of the EF_tau16_loose part of the trigger has been measured in data in bins of E_T of the tau candidate. The efficiency is defined with regards to the tau identification BDT medium for each E_T bin as

$$\epsilon_{tr} = \frac{N_{triggered}}{N_{identified}}, \quad (\text{C.1})$$

with $N_{triggered}$ being is the number of tau candidates passed the trigger requirement and $N_{identified}$ the number tau candidates passed the offline tau identification BDT medium.

C.1 Event Selection

The efficiency (C.1) is measured by using a tag-and-probe method on $Z \rightarrow \tau\tau \rightarrow \tau_e\tau_h$ events, where the tau decaying into an electron (and two neutrinos), τ_e , is used as the tag and the hadronically decaying tau, τ_h , is used as the probe [83]. The data events used are from periods F to H and correspond to an integrated luminosity of 1 fb^{-1} . They are selected by applying the single electron trigger, labelled as "EF_e20_medium", and keeping close with the event selection of the $e\tau_h$ channel as described in Sections 5.3 and 5.5:

The events are required to have a primary vertex with at least four tracks, passing the jet cleaning and the LAr hole cleaning. The tag electron has to fulfill the same identification and isolation requirements as described in 5.4.2. To reduce $Z \rightarrow ee$ events, a dilepton veto is applied and the cuts on $\sum \cos \Delta\phi > -0.15$ and $m_T < 50 \text{ GeV}$, as defined in Section 5.5 are used to reduce $W \rightarrow e\nu$ events.

The probe tau candidate has to pass the identification requirement BDT medium and to have exactly one or three tracks and unit charge, as applied for the cross section measurement. In case more than one tau candidate pass that criteria, the one with the highest E_T is chosen as the probe candidate. Further, the reconstructed charge of the tag electron and the probe tau has to be opposite and their visible mass has to be within $40 \text{ GeV} < M_{vis} < 80 \text{ GeV}$. The main remaining background contributions are due to QCD multijet events as well as $Z \rightarrow ee$ and $W \rightarrow e\nu$ events, which are all estimated with the exact same procedure as described in Section 5.7. Other background sources are neglected in this study.

C.2 Tau Trigger Efficiency Measurement

The tau trigger efficiency of the EF_tau16_loose trigger is measured in bins of E_T of the tau candidate as the number of taus passing the trigger requirement out of the probe taus passing the selection as described above. The selected probe tau candidate has to be matched to a tau trigger object passing the EF_tau16_loose trigger chain with in a cone of $\Delta R < 0.02$.

To obtain the tau trigger efficiency ϵ_T on signal events only, the contribution from the remaining background has to be extracted. The amounts of signal and background contributions after the selection described above can be seen in the distributions of visible mass and E_T of the tau candidate in Figure C.1.

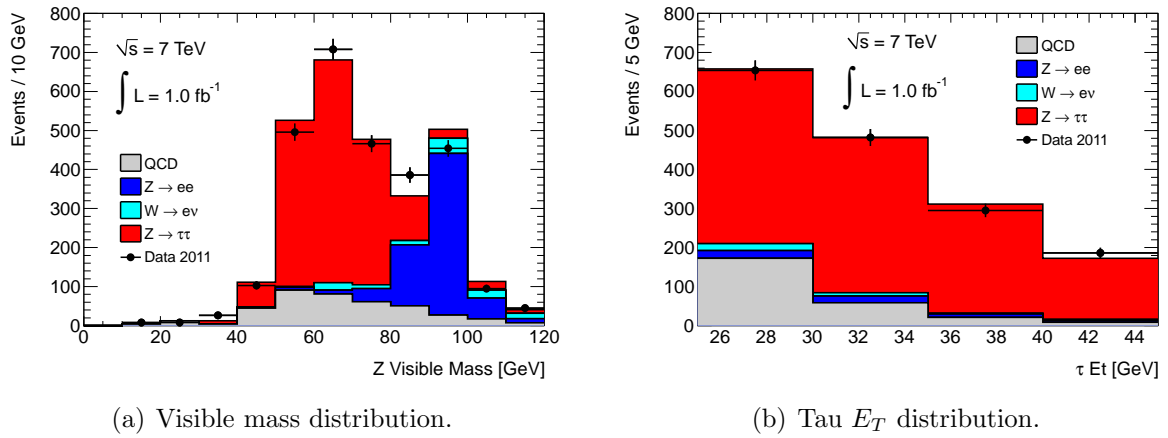
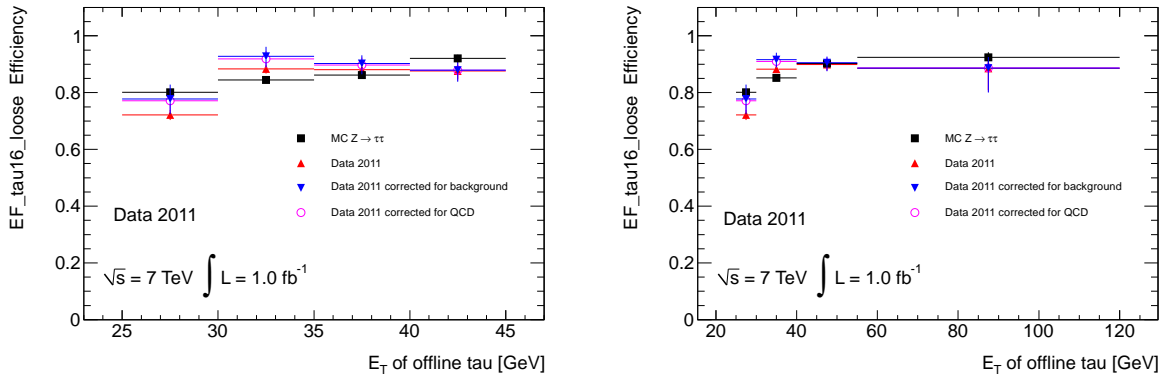


Figure C.1: The distributions of the visible mass (a) and E_T of the tau candidate (b) for the selection applied for the tau trigger efficiency measurement, except the cut on the visible mass [83].

The trigger efficiency for $Z \rightarrow \tau\tau$ signal events is calculated from the trigger efficiency on all selected data events, ϵ_{all} , and a correction term accounting for the background:

$$\epsilon_{tr} = \epsilon_{all} + \sum_i (\epsilon_{all} - \epsilon_{b,i} f_{b,i}), \quad (C.2)$$

where $\epsilon_{b,i}$ is the tau trigger efficiency on the i^{th} background component and $f_{b,i}$ is the fraction of background events in relation to signal events in the corresponding E_T bin. The index, i , stands for one of the background contributions, $Z \rightarrow ee$, $W \rightarrow e\nu$ and QCD multijet events. The fractions of the individual background contributions $f_{b,i}$ are obtained from MC simulations, while $\epsilon_{b,i}$ are evaluated from data by constructing background enriched control regions. This is done similar as for the cross section measurement. For the $Z \rightarrow ee$ control region, a cut on $M_{vis} > 80$ GeV is applied instead of the visible mass window $40 \text{ GeV} < M_{vis} < 80 \text{ GeV}$. For the $W \rightarrow e\nu$ region, the cuts on $\sum \cos \Delta\phi$ and m_T are inverted: $\sum \cos \Delta\phi > -0.15$, $m_T < 50$ GeV and the QCD multijet control region is defined by requiring the tag electron and probe tau to have same charge instead of opposite. The obtained trigger efficiencies are summarized in Figure C.2 for $Z \rightarrow \tau\tau$ MC only, uncorrected data in the signal region, data corrected for QCD multijet events and data corrected for all



(a) Tau trigger efficiency in the range of $25 \text{ GeV} < E_T < 45 \text{ GeV}$.
 (b) Tau trigger efficiency in the range of $25 \text{ GeV} < E_T < 120 \text{ GeV}$.

Figure C.2: The distributions of the tau trigger efficiency in dependence of E_T of the tau candidate and for MC and data with different background correction methods. The region most relevant for the cross section analysis (a) and a wide region up to 120 GeV (b) are shown [83].

backgrounds as described above. Those efficiencies are in agreement within their statistical uncertainties. The total number of data events in the signal region is 654 and the efficiencies from data corrected for all backgrounds is used for the tau trigger weighting in the cross section analysis.

C.3 Systematic Uncertainties

To evaluate the systematic uncertainty on the tau trigger weighting, three sources are considered: the uncertainty on the efficiency of the total number of data events in the signal region, $\delta\epsilon_{all}$, the uncertainty on the efficiency of the background efficiencies, $\delta\epsilon_{b,i}$, and the uncertainty on the background fraction, $\delta f_{b,i}$. The final uncertainty on the total trigger efficiency is calculated as:

$$\delta\epsilon_{tr} = \delta\epsilon_{all}\left(1 + \sum_i f_{b,i}\right) + \sum_i (\delta f_{b,i}(\epsilon_{all} - \epsilon_{b,i}) + \delta\epsilon_{b,i}f_{b,i}). \quad (\text{C.3})$$

Here, only the systematic uncertainties of the QCD multijet correction are included as the backgrounds of $Z \rightarrow ee$ and $W \rightarrow e\nu$ events are much smaller and thus their uncertainty contribution can be neglected [83]. For $\delta f_{b,i}$, the uncertainty on the opposite-sign to same-sign ratio of 5% is included [83]. The uncertainty on the trigger efficiency in the QCD multijet region, $\delta\epsilon_{b,i}$, is obtained from the variation of the efficiency in the region with opposite-sign and anti-isolated electrons and the region with same-sign and isolated electrons. The relative uncertainty of the tau trigger efficiency, propagated to the cross section measurement, is found to be 4.7% [83] as given in Table 5.15.

Bibliography

- [1] The ATLAS Collaboration, *Observation of a new particle in the search for the Standard Model Higgs boson with the ATLAS detector at the LHC*, Phys. Lett. B **716** (2012) 1–29, [arXiv:1207.7214](#).
- [2] The CMS Collaboration, *Observation of a new boson at a mass of 125 GeV with the CMS experiment at the LHC*, Phys. Lett. B **716** (2012) 30–61, [arXiv:1207.7235](#).
- [3] The ATLAS Collaboration, *The ATLAS Experiment at the CERN Large Hadron Collider*, JINST 3 S08003 (2008) .
- [4] The CMS Collaboration, *The CMS experiment at the CERN LHC*, JINST 3 S08004 (2008) .
- [5] The ATLAS Collaboration, *Measurement of the Z to tau tau Cross Section with the ATLAS Detector*, [arXiv:1108.2016 \[hep-ex\]](#).
- [6] The CMS Collaboration, *Measurements of Inclusive W and Z Cross Sections in pp Collisions at $\sqrt{s}=7$ TeV*, JHEP **08** (2011) 117.
- [7] J. Butterworth et al., *Single Boson and Diboson Production Cross Sections in pp Collisions at $\sqrt{s} = 7$ TeV*, ATL-COM-PHYS-2010-695, 2010.
- [8] S. Glashow, *Partial Symmetries of Weak Interactions*, Nucl. Phys. **22** (1961) 579.
- [9] S. Weinberg, *A Model of Leptons*, Phys. Rev. Lett. **19** (1967) 1264.
- [10] A. Salam, *Elementary Particle Theory*. Almqvist and Wiksell, Stockholm, 1968.
- [11] G. t’Hooft, *Renormalizable Lagrangians for massive Yang-Mills fields*, Nucl. Phys. **B 35** (1971) 167.
- [12] G. t’Hooft and M. Veltman, *Regularization and renormalization of gauge fields*, Nucl. Phys. **B 44** (1972) 189.
- [13] L. Davis, A. Goldhaber, and M. Nieto, *Limit on the Photon Mass Deduced from Pioneer-10 Observations of Jupiter’s Magnetic Field*, Phys. Rev. L. 35.1402 (1975) .
- [14] C. Amsler, *Kern- und Teilchenphysik*. 2007.
- [15] I. J. Aitchison and A. J. Hey, *Gauge Theories in Particle Physics*. 1989.
- [16] P. W. Higgs, *Broken Symmetries And The Masses Of Gauge Bosons*, Phys. Rev. Lett. **13** (1964) 508–509.

- [17] P. W. Higgs, *Spontaneous Symmetry Breakdown Without Massless Bosons*, Phys. Rev. **145** (1966) 1156–1163.
- [18] F. Englert and R. Brout, *Broken Symmetry and the Mass of Gauge Vector Mesons*, Phys. Rev. Lett. **13** (1964) 321.
- [19] C. H. G.S. Guralnik and T. Kibble, *Global Conservation Laws and Massless Particles*, Phys. Rev. Lett. **13** (1964) 585.
- [20] J. Beringer et al. (Particle Data Group). Phys. Rev. D86, 010001, 2012.
- [21] H. L. H. Fritzsch, M. Gell-Mann, *Advantages of the Color Octet Gluon Picture*, Phys. Lett. **B 47** (1973) 365.
- [22] H. D. Politzer, *Reliable Perturbative Results for Strong Interactions*, Phys. Rev. Lett. **30** (1973) 1346.
- [23] F. W. D. Gross, *Ultraviolet Behavior of Nonabelian Gauge Theories*, Phys. Rev. Lett. **30** (1973) 1343.
- [24] S. Weinberg, *Nonabelian Gauge Theories of the Strong Interactions*, Phys. Rev. Lett. **31** (1973) 494.
- [25] The ALEPH Collaboration et al., *Precision Electroweak Measurements on the Z Resonance*, Phys.Rept. **427** (2006) no. CERN-PH-EP/2005-041, SLAC-R-774, 257–454.
- [26] C. Adloff et al. (H1 Collaboration), *Determination of the Longitudinal Proton Structure Function $F_L(x, Q^2)$ at Low x* , Phys. Lett. B **393** (1997) 452.
- [27] C. Adloff et al. (H1 Collaboration), *Measurement of Neutral and Charged Current Cross-Sections in Positron-Proton Collisions at Large Momentum Transfer*, Eur. Phys. J. **C 13** (2000) 609.
- [28] C. Adloff et al. (H1 Collaboration), *Measurement of Neutral and Charged Current Cross Sections in Electron-Proton Collisions at High Q^2* , Eur. Phys. J. **C 19** (2001) 269.
- [29] C. Adloff et al. (H1 Collaboration), *Deep-Inelastic Inclusive ep Scattering at Low x and a Determination of α_s* , Eur. Phys. J. **C 21** (2001) 33.
- [30] S. Chekanov et al. (ZEUS Collaboration), *Measurement of the neutral current cross section and F_2 structure function for deep inelastic $e+p$ scattering at HERA*, Eur. Phys. J. **C 21** (2001) 443.
- [31] S. Chekanov et al. (ZEUS Collaboration), *Measurement of high- Q^2 charged current cross sections in e^+p deep inelastic scattering at HERA*, Eur. Phys. J. **C 32** (2003) 1.
- [32] B. Abbott et al. (D0 Collaboration), *Inclusive Jet Production in $p\bar{p}$ Collisions*, Phys. Rev. Lett. **86** (2001) 1707.

-
- [33] B. Abbott et al. (D0 Collaboration), *High- p_T jets in $\bar{p}p$ collisions at $\sqrt{s} = 630$ and 1800 GeV*, Phys. Rev. **64** (2001) 032003.
- [34] P. M. Nadolsky et al., *Implications of CTEQ global analysis for collider observables*, Phys. Rev. **D78** (2008) 013004.
- [35] M. L. Mangano, F. Piccinini, A. D. Polosa, M. Moretti, and R. Pittau, *ALPGEN, a generator for hard multiparton processes in hadronic collisions*, Journal of High Energy Physics (2003) no. 07, 001.
- [36] G. Corcella et al., *HERWIG 6.5*, JHEP **0101** (2001) 010.
- [37] J. Campbell, J. Huston, and W. Stirling, *Hard Interactions of Quarks and Gluons: a Primer for LHC Physics*, Rept.Prog.Phys. **70:89** (2007) .
- [38] S. Frixione and B. Webber, *Matching NLO QCD computations and parton shower simulations*, JHEP **0206** (2002) 029, arXiv:hep-ph/0204244.
- [39] T. Sjostrand, S. Mrenna, and P. Skands, *PYTHIA 6.4 physics and manual*, JHEP **05** (2006) 026.
- [40] The ATLAS Collaboration, *First tuning of HERWIG/JIMMY to ATLAS data*, ATL-PHYS-PUB-2010-014 (2010) .
- [41] J.M.Butterworth, J.R.Forshaw, and M.H.Seymour, *Multiparton Interactions in Photoproduction at HERA*, Z.Phys. **C** (1996) no. 72, 637–646.
- [42] The GEANT4 Collaboration, S. Agostinelli et al., *GEANT4: A simulation toolkit*, Nucl. Instrum. Meth. **A506** (2003) 250.
- [43] The ATLAS Collaboration, *The ATLAS Simulation Infrastructure*, Eur. Phys. J. **C70** (2010) 823–874.
- [44] J. M. Campbell and R. K. Ellis, *An update on vector boson pair production at hadron colliders*, Phys. Rev. **D60** (1999) 113006, arXiv:hep-ph/9905386.
- [45] C. Anastasiou, L. Dixon, K. Melnikov, and F. Petriello, *High-precision QCD at hadron colliders: electroweak gauge boson rapidity distributions at NNLO*, Phys. Rev. **D69** (2004) 094008.
- [46] R. Hamberg, W. L. van Neerven, and T. Matsuura, *High-precision QCD at hadron colliders: electroweak gauge boson rapidity distributions at NNLO*, Nucl. Phys. **B 359** (1991) .
- [47] J. Stirling, private communication, <http://mstwpdf.hepforge.org/>.
- [48] The LHC Study Group, *The Large Hadron Collider, conceptual design*, Technical Report CERN/AC/95-05(LHC) (1995) .
- [49] Lyndon Evans and Philip Bryant, *LHC Machine*, JINST **3** (2008) S08001 (2008) .
- [50] Online at: <http://lhc2008.web.cern.ch/LHC2008/inauguration/lhcexpo.html>, accessed 2012.

- [51] Christiane Lefevre, *The CERN accelerator complex*, CERN-DI-0812015 (2010) .
- [52] The LHCb Collaboration, *The LHCb Detector at the LHC*, JINST 3 (2008) S08005 (2008) .
- [53] The ALICE Collaboration, *The ALICE experiment at the CERN LHC*, JINST 3 (2008) S08002 (2008) .
- [54] A. Afonin, et al., *Relative luminosity measurement of the LHC with the ATLAS forward calorimeter*, JINST **5 P05005** (2010) .
- [55] The ATLAS Collaboration, *Luminosity Determination in pp Collisions at $\sqrt{s}=7$ TeV using the ATLAS Detector in 2011*, ATLAS-CONF-2011-116, Aug, 2011.
- [56] S. van der Meer, *Calibration of the effective beam height in the ISR*. *oai:cds.cern.ch:296752*, Tech. Rep. CERN-ISR-PO-68-31. ISR-PO-68-31, CERN, Geneva, 1968.
- [57] O. Igonkina and B. Petersen, *Proposal and Motivations for 2011 Trigger Menu*, Tech. Rep. ATL-COM-DAQ-2011-007, CERN, Geneva, 2011.
- [58] The ATLAS Collaboration, *Letter of Intent for the Phase-I Upgrade of the ATLAS Experiment.*, CERN-LHCC-2011-12, 2011.
- [59] S. Ivanov et al., *Accelerator complex U70 of IHEP-Protvino: status and upgrade plans*, Proceedings of rupac 2008, zvenigorod, russia, 2008.
- [60] A.G.Afonin et al., *High-Efficiency Beam Extraction and Collimation Using Channeling in Very Short Bent Crystals.*, Phys. Rev. **Lett.** **87** (2001) 094802.
- [61] Hilum ATLAS Liquid-Argon Endcap Collaboration, *Liquid argon calorimeter performance at high rates.*, Nuclear Instruments and Methods in Physics **A** **669** (2012) 47–65.
- [62] J. Rutherford, *Signal degradation due to charge buildup in noble liquid ionization calorimeters.*, Nuclear Instruments and Methods in Physics **A** **482** (2002) 156–178.
- [63] The ISEG company Dresden, Germany, online at: <http://www.iseg-hv.de>.
- [64] J. Rutherford, private communication.
- [65] The ATLAS Collaboration, *Z \rightarrow $\tau\tau$ cross section measurement in proton-proton collisions at 7 TeV with the ATLAS experiment*, ATLAS-CONF-2012-006, 2012.
- [66] S. Jadach, Z. Was, R. Decker, and J. H. Kühn, *The τ decay library TAUOLA, version 2.4*, vol. 76. Comput. Phys. Commun., 1993.
- [67] P. Golonka and Z. Was, *PHOTOS Monte Carlo: A Precision tool for QED corrections in Z and W decays.*, vol. C45. 2006.
- [68] K. Melnikov and F. Petriello, *Electroweak gauge boson production at hadron colliders through $O(\alpha(s)^2)$* , Phys. Rev. **D74** (2006) 114017.

-
- [69] R. Gavin, Y. Li, F. Petriello et al., *FEWZ 2.0: A code for hadronic Z production at next-to-next-to-leading order*, arXiv:1011.3540 [hep-ph].
- [70] S. Catani, L. Cieri, G. Ferrera, D. de Florian, and M. Grazzini, *Vector boson production at hadron colliders: a fully exclusive QCD calculation at NNLO*, Phys. Rev. Lett. **103** (2009) 082001, arXiv:0903.2120 [hep-ph].
- [71] ATLAS Good Run List Generator, Online at: <https://atlasdqm.cern.ch/grl/>.
- [72] K. Zenker, *Development of a data based algorithm for measuring the mistag rate of b-quarks at the ATLAS experiment*, CERN-THESIS-2010-167, 2010.
- [73] The ATLAS Collaboration, *Muon reconstruction efficiency in reprocessed 2010 LHC proton-proton collision data recorded with the ATLAS detector*, ATLAS-CONF-2011-063, 2011.
- [74] The ATLAS Collaboration, *Electron performance measurements with the ATLAS detector using the 2010 LHC proton-proton collision data*, CERN-PH-EP-2011-117, 2011. arXiv:1110.3174 [hep-ex].
- [75] M. Cacciari and G. P. Salam, *Dispelling the N3 myth for the kt jet-finder*, Physics Letters B **641** (2006) no. 1, 57 – 61. M. Cacciari, G. P. Salam and G. Soyez, <http://fastjet.fr/>.
- [76] The ATLAS Collaboration, *Expected performance of the ATLAS experiment: detector, trigger and physics.*, CERN-OPEN-2008-020, 2009.
- [77] The ATLAS Collaboration, *Performance of the Reconstruction and Identification of Hadronic Tau Decays with ATLAS*, ATLAS-CONF-2011-152, 2011.
- [78] The ATLAS Collaboration, *Reconstruction and Calibration of Missing Transverse Energy and Performance in Z and W events in ATLAS Proton-Proton Collisions at $\sqrt{7\text{ TeV}}$* , ATLAS-CONF-2011-080, 2011.
- [79] P. Bechtle et al., *Benchmark Analysis for Z to tau tau to lepton hadron with the First 100 pb⁻¹*, ATL-PHYS-INT-2010-075, 2010.
- [80] The ATLAS Collaboration, *Z → ττ candidate event display (07 October 2010)*, Online at: <https://twiki.cern.ch/twiki/bin/view/AtlasPublic/TauPublicCollisionResults>, Accessed Nov. 2012.
- [81] A. Sherstnev and R. S. Thorne, *Parton Distributions for LO Generators*, Eur. Phys. J. **C55** (2008) 553.
- [82] The ATLAS Collaboration, *Charged particle multiplicities in p p interactions at $\sqrt{s} = 0.9$ and 7 TeV in a diractive limited phase-space measured with the ATLAS detector at the LHC and new PYTHIA6 tune*, ATLAS-CONF-2010-031, 2010.
- [83] The ATLAS Collaboration, *Z → ττ cross section measurement with 1.34-1.55 fb⁻¹ at the ATLAS experiment*, ATLAS-COM-2011-1660, 2011.

-
- [84] H1, ZEUS Collaborations, *Combined Measurement and QCD Analysis of the Inclusive $e p$ Scattering Cross Sections at HERA*, JHEP **1001** (2010) 109.
- [85] The ATLAS Collaboration, *Jet energy scale and its systematic uncertainty in proton-proton collisions at $\sqrt{s}=7$ TeV in ATLAS 2010 data*, Atlas-conf-2011-032, 2011.
- [86] M. Aharrouche et al., *$W \rightarrow e\nu$ and $Z \rightarrow ee$ cross-section measurement in proton-proton collisions at $\sqrt{s} = 7$ TeV with the ATLAS Detector*, ATLAS Note: ATL-COM-PHYS-2010-701, Oct, 2010.
- [87] *Measurement of the top-quark pair production cross-section in pp collisions at $\sqrt{s} = 7$ TeV in dilepton nal states with ATLAS*, ATLAS conference note: ATLAS-CONF-2011-100, Oct, 2011.
- [88] L. Lyons, D. Gibaut, and P. Clifford, *How to combine correlated estimates of a single physical quantity*, Nucl. Instrum. Meth. **A270** (1988) 110.
- [89] A. Valassi, *Combining correlated measurements of several different physical quantities*, Nucl. Instrum. Meth. **A500** (2003) 391–405.
- [90] The ATLAS Collaboration, *Measurement of the $W \rightarrow \ell\nu$ and $Z/\gamma^* \rightarrow \ell\ell$ production cross sections in proton-proton collisions at $\sqrt{s} = 7$ TeV with the ATLAS detector*, Journal of High Energy Physics (2010) .

Danksagung

Hier möchte ich mich bei allen bedanken, die mich beim Erstellen dieser Arbeit unterstützt haben. Dazu gehört im Besonderen mein Betreuer Arno Straessner, der mir die Arbeit innerhalb dieses spannenden Forschungsfeldes ermöglicht hat und stets mit Rat und Tat zur Seite stand. Auch Wolfgang Mader, Xavier Prudent und Michael Kobel haben mir in zahlreichen Meetings viele wichtige Hinweise und Anregungen gegeben. Die tolle Zusammenarbeit mit Xavier während des Aufenthaltes am CERN in Büro oder Freizeit war immer ein Erlebnis.

Für sehr hilfreiches Korrekturlesen danke ich Arno Straessner, Wolfgang Mader, Sebastian Wahrmund, Christian Rudolph, Philipp Anger und Lydia Köhler. Ohne sie wären noch viel mehr Fehler in der Arbeit zu finden. Danke auch an Arnulf Quadt, dass er sich so kurzfristig als Gutachter dieser Dissertation bereit erklärt hat.

Der Dresdner ATLAS Gruppe möchte ich für die angenehme Arbeitsatmosphäre und die tolle Unterstützung mit der Computing-Infrastruktur danken. Auch die Zusammenarbeit mit den Tau- $Z \rightarrow \tau\tau$ - und LAr-Hilum Arbeitsgruppen von ATLAS war oft sehr intensiv und hat mir immer viel Freude bereitet.

Zum Schluss gilt mein ganz besonderer Dank meinen Freunden, die mir viel spaßigen Ausgleich ermöglicht haben und natürlich meiner lieben Familie, die stets bei all meinen Unternehmungen hinter mir gestanden hat.

Versicherung

Hiermit versichere ich, dass ich die vorliegende Arbeit ohne unzulässige Hilfe Dritter und ohne Benutzung anderer als der angegebenen Hilfsmittel angefertigt habe; die aus fremden Quellen direkt oder indirekt bernommenen Gedanken sind als solche kenntlich gemacht. Die Arbeit wurde bisher weder im Inland noch im Ausland in gleicher oder ähnlicher Form einer anderen Prüfungsbehörde vorgelegt.

Diese Arbeit wurde am Institut für Kern- und Teilchenphysik der Technischen Universität Dresden unter wissenschaftlicher Betreuung von Jun.-Prof. Dr. Arno Straessner angefertigt.

Dresden, den 12.11.2012

Frank Seifert